Opacity dependence of transverse flow, preequilibrium, and applicability of hydrodynamics in heavy-ion collisions

Victor E. Ambruş,[1,2] S. Schlichting,[3] and C. Werthmann[3,4,*]

[1]*Institut für Theoretische Physik, Johann Wolfgang Goethe-Universität, Max-von-Laue-Strasse 1, D-60438 Frankfurt am Main, Germany*
[2]*Department of Physics, West University of Timişoara, Bd. Vasile Pârvan 4, Timişoara 300223, Romania*
[3]*Fakultät für Physik, Universität Bielefeld, D-33615 Bielefeld, Germany*
[4]*Incubator of Scientific Excellence-Centre for Simulations of Superdense Fluids, University of Wrocław, pl. Maxa Borna 9, 50-204 Wrocław, Poland*

(Received 16 December 2022; accepted 20 February 2023; published 11 May 2023)

We evaluate the full opacity dependence of collective flow in high-energy heavy-ion collisions within a microscopic kinetic description based on the Boltzmann equation in the conformal relaxation time approximation. By comparing kinetic theory calculations to hydrodynamic and hybrid simulations for an average initial state, we point out shortcomings and inaccuracies of hydrodynamic models and present modified simulation setups to improve them.

DOI: 10.1103/PhysRevD.107.094013

I. INTRODUCTION

Relativistic heavy ion collisions have proven to be an important tool for probing the dynamical properties of QCD matter in and out of equilibrium. Many current efforts are concerned with using experimental data to assess the conditions under which a quark gluon plasma (QGP) forms in the collision, as well as its properties [1–3]. Since the QGP itself cannot be directly observed, its properties have to be inferred by studying suitable aspects of the data and comparing with model descriptions. Hydrodynamics has proven to be a powerful tool for simulating the QGP dynamics [4–9] and can accurately describe data for transverse flow, which is an important indicator of collective behavior. Modern Bayesian inference frameworks based on simulations using hydrodynamics are able to provide significant constraints on the transport properties of the medium created in the collision [1,3,10].

However, the conditions for applicability of hydrodynamics to describe hadronic collisions is still an open question. It is doubtful whether it can be applied to small systems with a dilute medium and large local gradients. Certainly it cannot describe the far-from-equilibrium stage right after the collision. The system will quickly approach equilibrium and start behaving hydrodynamically, but the timescales of its applicability in realistic systems are yet unclear. The topics of applicability to small systems and the properties of the preequilibrium stage have been the focus of many recent endeavors, as described below.

In an effort to find clear distinctive features that indicate the presence or absence of a QGP, small systems have been extensively studied in experiment and have proven to feature nonvanishing transverse flow [11–16] and therefore display an onset of collective behavior. There have been many efforts in simulating these systems in hydrodynamics [17–31], which have produced reasonable results. However, in contrast to nucleus-nucleus collisions, such calculations are subject to much larger uncertainties, where in addition to the poorly constrained initial state geometry [26,32,33], one may question the theoretical justification for employing a hydrodynamic description for a system which features a very short lifetime and consists of very few degrees of freedom. Hence, alternative descriptions with a more sound motivation of their applicability have been put forward. For example, it has been studied whether initial state effects as described by the color glass condensate model could be the source of collective flow in small systems [34–45]. However, it turns out that these dynamics fail to describe the important systematics [46].

On the other front, significant progress has been made in pushing the theoretical understanding of the dynamics in the preequilibrium stage and the approach to hydrodynamic behavior and eventually equilibrium in large and small systems [47–49] (see also [50,51] for recent reviews). Descriptions of Bjorken flow have been found to exhibit universal behavior across different dynamical models and initial conditions [52–67]. The far-from-equilibrium behavior depends on the setup, but the approach to equilibrium proceeds in the same way by means of an attractor solution

*cwerthmann@physik.uni-bielefeld.de

that has been studied extensively. This concept has since also been applied to systems with trivial and nontrivial transverse expansion [68–71]. Phenomenologically, it has been shown that the preequilibrium stage has a non-negligible influence on final state observables [71–75] and it is therefore crucial to employ realistic descriptions thereof.

An appropriate alternative dynamical model for small systems as well as preequilibrium is kinetic theory, which is a mesoscopic description of the phase space distribution of interacting particles and is therefore less constrained in its applicability to very dilute systems and far-from-equilibrium dynamics. Applications of kinetic theory to heavy ion collisions have been proposed already 30 years ago [76–79] and have been used in different model scenarios to various levels in complexity. Among others, this has lead to the simulation code Boltzmann Approach to Multi-Parton Scattering (BAMPS) [80,81]. Several efforts have succeeded in describing transverse dynamics and the buildup of transverse flow within this description [82–92], in some cases even with event-by-event simulations [39,49,93,94].

The success of relativistic hydrodynamics in describing experimental observables, demonstrated repeatedly during the past two decades [95], is heavily dependent on the various theoretical models that lead to such an effective description of strongly-interacting matter. Key ingredients include initial-state generators such as IP-Glasma [96] or MC-Glauber [97], QCD equation of state and realistic transport coefficients [98], hadronization models [99], as well as particle-based hadronic transport such as UrQMD [100]. All of these stages introduce sometimes unquantifiable uncertainties, while statistical approaches such as the Bayesian analysis can be used to pinpoint the most probable parameter-set values of each of these models [101].

In our previous work [71], we found that for final state observables related to transverse flow, results from purely hydrodynamic simulations are in disagreement with results from kinetic theory even at very large opacities due to differences between the dynamics in these two theories during the preequilibrium phase. Even though equilibration proceeds on arbitrarily short timescales for sufficiently large opacities, conversely the rate of change of observables in this period increases, such that it still has a tangible effect on their final values. We also examined how, at early times, even an inhomogeneous system obeying boost invariance can be described locally by $0+1$D Bjorken flow and used the corresponding universal attractor solution to predict the time evolution before the onset of transverse expansion. This also allowed us to describe the discrepancies between hydrodynamics and kinetic theory due to preequilibrium in quantitative detail and verify that the size of this effect matches with the described discrepancy of final state observables.

Motivated by these results, the aim of this paper and its companion paper [102] is to examine how in practice simulations of heavy ion collisions based on hydrodynamics can be brought into agreement with kinetic theory simulations. In the present paper, we perform an in-depth theoretical analysis of the nonequilibrium dynamics in different time evolution models based exclusively on midcentral collision events, while a broad phenomenological analysis inferring conclusions for the applicability of hydrodynamics in small systems is presented in Ref. [102].

The time evolution is modeled in a simplified description based on the relaxation time approximation (RTA) of conformal kinetic theory. In such a simplistic model, the ultrarelativistic equation of state $\epsilon = 3P = aT^4$ can realistically describe the quark-gluon plasma only in the ultrahigh temperature phase, when interactions become negligible [103]. Furthermore, the bulk viscous pressure vanishes identically for a conformal fluid, while Bayesian studies indicate that bulk viscosity can play a significant role on final-state observables [104]. Also, our conformal model gives a constant shear viscosity to entropy density ratio, $\eta/s = \text{const}$, which is a crude approximation for the expected temperature variation of this ratio [101,105]. Nevertheless, due to its simplistic evaluation of the collision kernel, the RTA has the clear advantage of being computationally cheaper over more realistic collision kernels (e.g. AMY [106]). Such kernels are typically too expensive to be implemented in deterministic solvers, such as the lattice Boltzmann approach that we employ in this paper [71,107,108]. Previous implementations of higher-dimensional dynamics (e.g. BAMPS [80,81]) therefore rely on a test particle algorithm and thus suffer from statistical noise. Furthermore, the first- and second-order transport coefficients computed for the RTA can be readily implemented in the relativistic hydrodynamics solver, allowing for a well-defined comparison between the two theories. Within this model, we perform an analysis of the circumstances under which hydrodynamics becomes applicable as a function of opacity and time, as determined by comparing results for a set of observables related to cooling and transverse flow to kinetic theory. Due to the above simplifications our simulation results cannot be expected to realistically describe experimental data, nevertheless we expect that our conclusions regarding the applicability of hydrodynamics also hold for more realistic models. One argument for this is that the low-momentum behavior close to equilibrium—which is the relevant part for a comparison to hydrodynamics—should be qualitatively similar between all collision kernels. The model setup, initial conditions and the set of observables are introduced in Sec. II.

Apart from kinetic theory and hydrodynamics, in our work we also used other evolution models, which are discussed in Sec. III. We employed an expansion scheme of kinetic theory that linearizes in opacity and should agree with full kinetic theory in the limit of small interaction rates. We also employed KøMPøST [109,110] as an alternative to using a full kinetic theory simulation of the pre-equilibrium phase. Switching from this description to hydrodynamics for the equilibrated system in a hybrid simulation framework is one way to properly include

preequilibrium dynamics. KøMPøST is an approximation of the dynamics of kinetic theory, which we were able to verify in quantitative detail by comparing to full kinetic theory, the results of which are presented in Sec. III E.

Before presenting our results, we first discuss in detail how preequilibrium is described in hydrodynamics and kinetic theory, pointing out the differences between the two theories. To this end, in Sec. IV we introduce the 1D Bjorken flow attractor solution. This description is valid locally also for early times in 3D simulations assuming boost invariance. We use it to make predictions of the preequilibrium behavior in both evolution models, including a prediction of preflow. Based on our results for the differences of kinetic theory and hydrodynamics in this phase, we then introduce a scaling scheme for the initial condition of hydro that can counteract these differences. This scheme relies on a timescale separation of equilibration and the onset of transverse expansion.

In Sec. V, we discuss the time evolution of the system at three example opacities. On the basis of transverse profiles, we indicate how the picture changes from a close-to-free streaming to an almost fully equilibrated system in kinetic theory. We compare the time evolution in kinetic theory and viscous hydrodynamics as well as in hybrid schemes. Within these hybrid schemes, the first part of the system's evolution is modeled using kinetic theory. Afterwards, we switch to hydrodynamics to model the remainder of the evolution. For sufficiently large opacities, our proposed scaling scheme indeed brings hydrodynamics into agreement with kinetic theory after preequilibrium. Based on the system's equilibration, we present a useful criterion for the applicability of hydrodynamics, which can be used to define the switching times for hybrid schemes. This criterion is reached at later evolution times for smaller opacities and in some cases is never fulfilled. We find that when switching sufficiently late, hybrid schemes are also in good agreement with kinetic theory. KøMPøST + viscous hydro simulations yield similar results as simulations with full kinetic theory + viscous hydrodynamics.

The range of applicability of the different schemes can best be assessed by studying the opacity dependence of final state observables. In Sec. VI, we compare first naive and scaled hydrodynamics to kinetic theory and establish $4\pi\eta/s \lesssim 3$ as the opacity range where the scaling scheme brings agreement. We then show results from the two hybrid simulation schemes, which can improve on scaled hydro results in the intermediate opacity range around $4\pi\eta/s \sim 3$.

In Sec. VII, we present our conclusions and give a brief outlook. Appendix A summarizes the details regarding the relativistic lattice Boltzmann solver that we employ for solving the kinetic equation. Appendices B 1 and B 2 provide further details on how the linearized results in opacity expansion were obtained, while in Appendices C and D we discuss some additional results for the time evolution of the system.

II. INITIAL STATE AND OBSERVABLES

We will describe the time evolution of the plasma created in a collision under the assumption of boost invariance in the longitudinal direction, when the phase-space distribution $f \equiv f(x,p)$ of single particles depends only on the difference of the pseudorapidity $y = \operatorname{artanh}(p^z/p^t)$ and the spacetime rapidity $\eta = \operatorname{artanh}(z/t)$. We also assume that at initial time τ_0, the particles comprising the fluid have an isotropic distribution in transverse momentum $\mathbf{p}_\perp$ and vanishing momentum along the longitudinal direction, or, in other words, the longitudinal pressure P_L measured in the local rest frame vanishes [111]. For the latter assumption to be valid in kinetic theory simulations, we choose the initialization time τ_0 to be small enough for the system to start from the early time free-streaming attractor of kinetic theory [60]. Further assuming that the interparticle interactions can be modeled in the RTA, and describing only a reduced distribution function with no dependence on total momentum [71,88], the initial state is fully determined by the initial transverse energy density per unit rapidity, $\mathrm{d}E_\perp^0/\mathrm{d}\eta\mathrm{d}^2\mathbf{x}_\perp$. The detailed reduced distribution functions are given in Appendix A.

A. Initial state

We will use a realistic average initial condition for the 30–40% most central Pb-Pb collisions (see also our companion paper [102] for a comparison of hydrodynamization in different centrality classes). This initial condition was generated numerically on a transverse grid of size 512×512 in the following way. A saturation model based initial state generator was used to generate 8×10^6 events with aligned directions of the impact parameter, which were then divided into centrality classes. Then the pointwise average of all events in each centrality class was taken. We made sure that in the resulting event averages statistical fluctuations are sufficiently suppressed by checking that they feature no local peaks above an energy density level of 10^{-6} times its maximum. More details on this event generation procedure can be found in [112].

Given this initial condition for $\mathrm{d}E_\perp^0/\mathrm{d}\eta\mathrm{d}^2\mathbf{x}_\perp$, the full initial state can be constructed according to the model assumptions. Enforcing at initial time τ_0 a vanishing longitudinal pressure P_L and ignoring possible initial-state transverse-plane dynamics, the initial energy-momentum tensor is diagonal and has the following components:

$$T^{\mu\nu}(\tau_0, \mathbf{x}_\perp) = \mathrm{diag}(\epsilon_0, \epsilon_0/2, \epsilon_0/2, 0), \tag{1}$$

where the initial energy density $\epsilon_0 \equiv \epsilon(\tau_0, \mathbf{x}_\perp)$ is given by

$$\epsilon(\tau_0, \mathbf{x}_\perp) = \frac{1}{\tau_0}\frac{\mathrm{d}E_\perp^0}{\mathrm{d}\eta\mathrm{d}^2\mathbf{x}_\perp}. \tag{2}$$

In order to characterize the initial energy distribution, we define the total transverse energy per rapidity $\mathrm{d}E_\perp^0/\mathrm{d}\eta$

$$\frac{\mathrm{d}E_\perp^0}{\mathrm{d}\eta} = \int_{\mathbf{x}_\perp} \tau_0 \epsilon_0 \tag{3}$$

and effective radius R

$$R^2 \frac{\mathrm{d}E_\perp^0}{\mathrm{d}\eta} = \int_{\mathbf{x}_\perp} \tau_0 \epsilon_0 \mathbf{x}_\perp^2, \tag{4}$$

where $\int_{\mathbf{x}_\perp} \equiv \int \mathrm{d}^2\mathbf{x}_\perp$, as well as the eccentricities ϵ_n

$$\epsilon_n(\tau) = -\frac{\langle x_\perp^n \cos\left[n(\phi_x - \Psi_n)\right]\rangle_\epsilon}{\langle x_\perp^n \rangle_\epsilon}, \tag{5}$$

where Ψ_n are event plane angles and the energy density weighted average over transverse space is defined as

$$\langle \mathcal{O} \rangle_\epsilon(\tau) = \frac{\int_{\mathbf{x}_\perp} \mathcal{O}(\tau, \mathbf{x}_\perp)\epsilon(\tau, \mathbf{x}_\perp)}{\int_{\mathbf{x}_\perp} \epsilon(\tau, \mathbf{x}_\perp)}. \tag{6}$$

Based on the definitions in Eqs. (3) and (4), we introduce the opacity of a system with shear viscosity to entropy density ratio η/s via

$$\hat{\gamma} = \frac{1}{5\eta/s}\left(\frac{R}{\pi a}\frac{\mathrm{d}E_\perp^0}{\mathrm{d}\eta}\right)^{1/4}, \tag{7}$$

where a is related to the equation of state via

$$a = \frac{\epsilon}{T^4} = \frac{\pi^2 \nu_{\mathrm{eff}}}{30}, \tag{8}$$

where T is the local temperature and $\nu_{\mathrm{eff}} = 42.25$ represents the effective number of degrees of freedom of high temperature QCD [113,114]. The characteristic properties for the initial condition we use are summarized in Table I. As we use a fixed profile, the parameters R and $\mathrm{d}E_\perp^0/\mathrm{d}\eta$ are also fixed and we vary $\hat{\gamma}$ by changing η/s. Hence, throughout this paper, whenever discussing opacity dependencies, we will characterize the opacity via the value of the shear viscosity to entropy density ratio η/s. Note, however, that these two quantities are inversely proportional.

B. Observables

We consider a set of observables which are measured as a function of time τ. Their final state values are taken at finite time, $\tau/R = 4$. These observables are chosen such that they can be easily computed within the two frameworks considered in this paper, namely kinetic theory and hydrodynamics.

TABLE I. Characteristic properties of the initial condition for the energy density used in this work, corresponding to an average over profiles in the 30–40% centrality class of Pb-Pb collision at $\sqrt{s_{NN}} = 5.02$ TeV [112], as discussed in Sec. II A.

$\mathrm{d}E_\perp^0/\mathrm{d}\eta$ [GeV]	R [fm]	$\hat{\gamma} \times 4\pi\eta/s$	ϵ_2	ϵ_4	ϵ_6
1280	2.78	11.3	0.416	0.210	0.0895

Specifically, we focus on observables that are derived from the energy-momentum tensor, which is the fundamental object of hydrodynamics and can be calculated in kinetic theory as

$$T^{\mu\nu} = \langle p^\mu p^\nu \rangle, \tag{9}$$

where angular brackets denote the microscopic average of an observable O with respect to the single-particle distribution function f:

$$\langle O \rangle \equiv \int \mathrm{d}P\, f O, \tag{10}$$

while $\mathrm{d}P = \nu_{\mathrm{eff}}\sqrt{-g}\mathrm{d}^3p/[(2\pi)^3 p_0]$ is the generally covariant integration measure in momentum space.

We work in the Landau frame, where the local rest frame energy density ϵ and flow velocity u^μ are given as the timelike eigenvalue and eigenvector of the energy-momentum tensor:

$$T^{\mu\nu}u_\nu = T^{\mu\nu}_{\mathrm{eq}}u_\nu = \epsilon u^\mu, \tag{11}$$

where the energy-momentum tensor in thermal equilibrium reads

$$T^{\mu\nu}_{\mathrm{eq}} = (\epsilon + P)u^\mu u^\nu - P g^{\mu\nu}. \tag{12}$$

In order to facilitate the comparison between kinetic theory and relativistic hydrodynamics, we use as a substitute for $\mathrm{d}E_\perp/\mathrm{d}\eta = \tau \int_{\mathbf{x}_\perp} \langle p^\tau p_\perp \rangle$ the integral of the transverse part of the trace of the energy-momentum tensor, $\epsilon_{\mathrm{tr}} \equiv T^{\tau\tau} - \tau^2 T^{\eta\eta} = T^{xx} + T^{yy}$, computed as

$$\frac{\mathrm{d}E_{\mathrm{tr}}}{d\eta} = \tau \int_{\mathbf{x}_\perp} (T^{xx} + T^{yy}), \tag{13}$$

which is equal to the actual transverse energy per rapidity $\mathrm{d}E_\perp/\mathrm{d}\eta$ whenever the rapidity component of the particle momentum is negligible, $p^\eta \simeq 0$. Similarly, instead of the flow harmonics v_n, we will focus on the ellipticity of the energy flow ε_p, defined in terms of the transverse components of the energy-momentum tensor as

$$\varepsilon_p e^{2i\Psi_p} = \frac{\int_{\mathbf{x}_\perp} (T^{xx} - T^{yy} + 2iT^{xy})}{\int_{\mathbf{x}_\perp} (T^{xx} + T^{yy})}, \tag{14}$$

where Ψ_p is the symmetry plane angle of the elliptic flow ε_p.

In order to characterize the expansion rate in the transverse plane, we consider the energy-weighted average of the transverse four-velocity, defined as

$$\langle u_\perp \rangle_\epsilon = \langle (u_x^2 + u_y^2)^{1/2} \rangle_\epsilon. \tag{15}$$

The local departure from equilibrium can be characterized in terms of the inverse Reynolds number,

$$\mathrm{Re}^{-1}(\tau, \mathbf{x}_\perp) = \left[\frac{6\pi^{\mu\nu}(\tau, \mathbf{x}_\perp)\pi_{\mu\nu}(\tau, \mathbf{x}_\perp)}{\epsilon^2(\tau, \mathbf{x}_\perp)} \right]^{1/2}, \tag{16}$$

where $\pi^{\mu\nu}$ is defined as the nonequilibrium part of the energy-momentum tensor:

$$\pi^{\mu\nu} = T^{\mu\nu} - T^{\mu\nu}_{\mathrm{eq}}. \tag{17}$$

With the above normalization, $\mathrm{Re}^{-1} = 1$ when $T^{\mu\nu} = \mathrm{diag}(\epsilon, \epsilon/2, \epsilon/2, 0)$, corresponding to the initial preequilibrium free-streaming limit. As a global measure of nonequilibrium effects in the system, we use the energy-weighted average inverse Reynolds number $\langle \mathrm{Re}^{-1} \rangle_\epsilon$.

III. EVOLUTION MODELS

We want to compare the dynamics of several different time evolution frameworks, which first have to be introduced. In Sec. III A, we discuss the relativistic kinetic model based on the RTA, which is solved using the relativistic lattice Boltzmann approach [107]. Section III B discusses an analytical approach aimed at approximating the solution of the kinetic theory model for small opacities. Section III C summarizes the equations of relativistic hydrodynamics, which are solved using the vHLLE code [115]. Finally, Sec. III D introduces the linear response framework KøMPøST [109,110], which was modified to include RTA Green's functions [116].

A. Kinetic theory (RTA)

As the primary tool to investigate the time evolution of the initial configurations discussed in Sec. II A, we employ the relativistic Boltzmann equation in the Anderson-Witting RTA [117–120]:

$$p^\mu \partial_\mu f = -\frac{p \cdot u}{\tau_R}(f - f_{\mathrm{eq}}), \tag{18}$$

where $p^\mu = (p^\tau, \mathbf{p}_\perp, p^\eta)$ is the particle four-momentum of massless on-shell particles ($p^2 = 0$), and $\tau_R = 5(\eta/s)/T$ is the relaxation time [121]. The prefactor is determined by the fact that in conformal RTA, the shear viscosity is given as $\eta = 4\tau_R P/5$ and the entropy density as $s = 4P/T$. For the remainder of this paper, we will consider that the specific shear viscosity η/s is constant. The rest frame velocity u^μ and energy density $\epsilon = aT^4$ are determined according to Eqs. (9), (11). As $\tau_R \propto 1/T$, the system obeys conformal symmetry, which simplifies its dynamics. Introducing the reference length scale $\ell_{\mathrm{ref}} = R$ and reference energy density $\epsilon_{\mathrm{ref}} = \frac{1}{\pi R^3}(\mathrm{d}E^0_\perp/\mathrm{d}\eta)$, Eq. (18) can be nondimensionalized as

$$v^\mu \tilde{\partial}_\mu f = -v^\mu u_\mu \hat{\gamma}\, \tilde{T}(f - f_{\mathrm{eq}}), \tag{19}$$

where $v^\mu = p^\mu/p^\tau$, $\tilde{\partial}_\mu = \ell_{\mathrm{ref}}\partial_\mu$, $\tilde{T} = T/T_{\mathrm{ref}}$, and $T_{\mathrm{ref}} = (\epsilon_{\mathrm{ref}}/a)^{1/4}$. In this formulation of the equation, it becomes apparent that the time evolution of f parametrically depends only on the opacity $\hat{\gamma}$ introduced in Eq. (7). The equilibrium distribution appearing on the right-hand side of Eq. (18) can be identified as the Bose-Einstein distribution

$$f_{\mathrm{eq}} = \frac{1}{\exp\left(p \cdot u(x)/T(x)\right) - 1}; \tag{20}$$

however, as pointed out in [88], the dynamics depend only on the fact that this distribution is isotropic in the local rest frame. The initial state corresponding to vanishing longitudinal pressure is modeled via

$$f(\tau_0, \mathbf{x}_\perp, \mathbf{p}_\perp, y - \eta) = \frac{(2\pi)^3}{\nu_{\mathrm{eff}}} \frac{\delta(y - \eta)}{\tau_0 p_\perp} \frac{\mathrm{d}N_0}{\mathrm{d}^2\mathbf{x}_\perp \mathrm{d}^2\mathbf{p}_\perp \mathrm{d}y}, \tag{21}$$

where $y - \eta = \mathrm{artanh}(\tau p^\eta/p^\tau)$. The initial particle distribution is assumed to be isotropic with respect to the azimuthal angle $\varphi_p = \arctan(p^y/p^x)$, being connected with the initial transverse-plane energy distribution $\mathrm{d}E^0_\perp/\mathrm{d}\eta\mathrm{d}^2\mathbf{x}_\perp$ via

$$\frac{\mathrm{d}E^0_\perp}{\mathrm{d}\eta \mathrm{d}^2\mathbf{x}_\perp} = 2\pi \int_0^\infty \mathrm{d}p_\perp p_\perp^2 \frac{\mathrm{d}N_0}{\mathrm{d}^2\mathbf{x}_\perp \mathrm{d}^2\mathbf{p}_\perp \mathrm{d}y}. \tag{22}$$

In this paper, we employ the relativistic lattice Boltzmann (RLB) method [122–124] to solve Eq. (19). The full details of the algorithm are given in Sec. IV.B of Ref. [71]. The key ideas and simulation parameters are summarized in Appendix A. In the following, we will refer to the numerical solution obtained using the lattice Boltzmann algorithm as described above as "kinetic theory."

B. Opacity expansion

For small systems, the dynamical behavior is expected to be close to free streaming, with only slight corrections coming from the small but finite number of interactions. In the limit of small opacity, we expand the solution of the Boltzmann equation in opacity up to linear order: $f \approx f^{(0)} + f^{(1)}$. We follow the expansion scheme that was introduced in [82,83], which has recently also been used in other works examining small systems [84,86,87,89,92]. To zeroth order, there are no interactions, and the time evolution of the phase space distribution is computed in the free-streaming limit

$$p^\mu \partial_\mu f^{(0)} = 0. \tag{23}$$

Parametrizing the momentum space in terms of $(\mathbf{p}_\perp, y)$, $f^{(0)}$ can be related to the distribution at initial time via

$$f^{(0)}(\tau, \mathbf{x}_\perp, \eta, \mathbf{p}_\perp, y) = f\Bigg(\tau_0, \mathbf{x}_\perp - \mathbf{v}_\perp t(\tau, \tau_0, y-\eta), y - \operatorname{arcsinh}\left(\frac{\tau}{\tau_0}\sinh(y-\eta)\right), \mathbf{p}_\perp, y\Bigg), \tag{24}$$

where

$$t(\tau, \tau_0, y-\eta) = \tau\cosh(y-\eta) - \sqrt{\tau_0^2 + \tau^2\sinh^2(y-\eta)}. \tag{25}$$

The linear order correction $f^{(1)}$ vanishes at initial time. Its time evolution is given by the scattering rates of the zeroth order solution,

$$p^\mu \partial_\mu f^{(1)} = C[f^{(0)}]. \tag{26}$$

Its explicit expression and properties are presented in Appendix B. As parametrically, the collision kernel is proportional to the opacity $\hat{\gamma}$, cf. Eq. (A3), we can indeed identify it as the expansion parameter in this scheme.

To enable our scheme to deal with arbitrary input data, the linear order results have to be computed numerically. The computation requires performing a 6D integral, which in part can be done analytically. The details of the code for linear order results are explained in Appendix B.

C. Ideal and viscous hydrodynamics

Relativistic hydrodynamics [125] is an effective macroscopic description based on the conservation equations $\nabla_\mu T^{\mu\nu} = 0$ for energy and momentum. After decomposing the energy-momentum tensor $T^{\mu\nu}$ according to Eqs. (17), (12), the equations can be cast in the form

$$\begin{aligned} \dot{\epsilon} + (\epsilon + P)\theta - \pi^{\mu\nu}\sigma_{\mu\nu} &= 0, \\ (\epsilon + P)\dot{u}^\mu - \nabla^\mu P + \Delta^\mu{}_\lambda \partial_\nu \pi^{\lambda\nu} &= 0, \end{aligned} \tag{27}$$

where $\theta = \partial_\mu u^\mu$ is the expansion scalar and $\sigma_{\mu\nu} = \nabla_{\langle\mu} u_{\nu\rangle}$ is the shear tensor, while $A^{\langle\mu\nu\rangle} = \Delta^{\mu\nu}_{\alpha\beta} A^{\alpha\beta}$, $\Delta^{\mu\nu}_{\alpha\beta} = \frac{1}{2}(\Delta^\mu_\alpha \Delta^\nu_\beta + \Delta^\nu_\alpha \Delta^\mu_\beta) - \frac{1}{3}\Delta^{\mu\nu}\Delta_{\alpha\beta}$ and $\Delta^{\mu\nu} = g^{\mu\nu} - u^\mu u^\nu$.

Equation (27) provides only four evolution equations, governing the dynamics of ϵ and u^μ, leaving the dissipative shear-stress $\pi^{\mu\nu}$ as defined in Eqs. (17), (12) unspecified. In ideal hydrodynamics, $\pi^{\mu\nu} = 0$ at all times, such that the system of equations in (27) becomes closed.

Modeling dissipative effects by means of the Navier-Stokes constitutive equation $\pi^{\mu\nu} \simeq \pi^{\mu\nu}_{\mathrm{NS}} = 2\eta\sigma^{\mu\nu}$, where η is the shear viscosity, leads to parabolic equations which violate causality and are thus incompatible with special relativity [126,127]. In this paper, we will consider the Müller-Israel-Stewart-type theory of second-order hydrodynamics [128,129], by which $\pi^{\mu\nu}$ evolves according to the following equation [120,130]:

$$\tau_\pi \dot{\pi}^{\langle\mu\nu\rangle} + \pi^{\mu\nu} = 2\eta\sigma^{\mu\nu} + 2\tau_\pi \pi^{\langle\mu}_\lambda \omega^{\nu\rangle\lambda} - \delta_{\pi\pi}\pi^{\mu\nu}\theta - \tau_{\pi\pi}\pi^{\lambda\langle\mu}\sigma^{\nu\rangle}_\lambda + \phi_7 \pi^{\langle\mu}_\alpha \pi^{\nu\rangle\alpha}, \tag{28}$$

where $\omega_{\mu\nu} = \frac{1}{2}[\nabla_\mu u_\nu - \nabla_\nu u_\mu]$ is the vorticity tensor. The relaxation time τ_π, as well as the other coupling coefficients, represent second-order transport coefficients, the values of which are chosen for compatibility with RTA [131–133]:

$$\eta = \frac{4}{5}\tau_\pi P, \quad \delta_{\pi\pi} = \frac{4\tau_\pi}{3}, \quad \tau_{\pi\pi} = \frac{10\tau_\pi}{7}, \quad \phi_7 = 0, \tag{29}$$

while $\tau_\pi = \tau_R$.

Numerical solutions of Eqs. (27) and (28) reported in this paper are obtained using the open-source viscous HLLE (vHLLE) code [115],[1] which we modified to allow the implementation of the initial state considered in this paper (we employed vHLLE also in Ref. [71] for a similar application). Specifically, we employed the square simulation domain $[-8R, 8R] \times [-8R, 8R]$, which we discretized using 401×401 equidistant points. The simulations were performed until the final time $\tau_f = 5R$. The initial state was prepared using insight on the hydrodynamic attractor, as will be discussed in Sec. IV D. In the initial state, a background value of $10^{-7} \times \frac{R}{\tau_0}\epsilon_{\mathrm{ref}}$ was added to the energy density to prevent free-streaming artifacts in the system outskirts. The time step $\delta\tau$ was chosen dynamically,

$$\delta\tau(\tau) = \min\left[\tau\left(\frac{\delta\tau}{\tau}\right)_{\mathrm{M}}, R\left(\frac{\delta\tau}{R}\right)_{\mathrm{M}}\right], \tag{30}$$

where $(\delta\tau/\tau)_{\mathrm{M}} = 0.01$ and $(\delta\tau/R)_{\mathrm{M}} = 10^{-3}$.

D. KøMPøST

The open-source simulation code KøMPøST [109] implements a linearized nonequilibrium time evolution of the energy-momentum tensor $T^{\mu\nu}$ based on the dynamics of a kinetic theory description. It has been developed as a practical tool for describing the early time far-from-equilibrium dynamics of heavy ion collisions, where the system has not yet hydrodynamized and a nonequilibrium description is required. The original version of KøMPøST was based specifically on the effective kinetic theory for pure glue QCD [106]. To perform accurate comparisons with the other evolution models used in this paper, a modified version based on the dynamics of RTA was used. For this, we imported the RTA Green's functions calculated in [116]. This version of KøMPøST is available on Git.

[1]Commit number `efa9e28d24d5115a8d8134852-32fb342b38380f0`.

KøMPøST evolves a given input initial state from an initial time τ_0 to a final time τ in a single propagation step. Conceptionally, the output is expected to describe a hydrodynamized system and can be used as input for a subsequent hydrodynamic evolution model. Since the computation of this step involves linearizations in perturbations around a local average value, KøMPøST has a limited range of applicability in the evolution time.

More specifically, in its default mode with energy perturbations, KøMPøST propagates the energy momentum tensor in the following way: the values at each point $\mathbf{x}$ in the final state are computed from the initial values of $T^{\mu\nu}$ at all causally connected points $\mathbf{x}'$ in the initial state, meaning points that fulfill $|\mathbf{x}-\mathbf{x}'| < c(\tau-\tau_0)$. The energy-momentum tensor is divided into a spatial average of the causal past and perturbations around this average:

$$T^{\mu\nu}_{\mathbf{x}}(\tau_0,\mathbf{x}') = \bar{T}^{\mu\nu}_{\mathbf{x}}(\tau_0) + \delta T^{\mu\nu}_{\mathbf{x}}(\tau_0,\mathbf{x}'),$$

where the subscript $\mathbf{x}$ denotes the fact that the average depends on the position for which the causal past is considered. The average value is evolved according to the laws of Bjorken flow dynamics, assuming local homogeneity in the transverse plane and boost invariance, while the perturbations are propagated in a linear response scheme:

$$\delta T^{\mu\nu}(\tau,\mathbf{x}) = \int \mathrm{d}^2\mathbf{x}' G^{\mu\nu}_{\alpha\beta}(\mathbf{x},\mathbf{x}',\tau,\tau_0)\delta T^{\alpha\beta}_{\mathbf{x}}(\tau_0,\mathbf{x}')\frac{\bar{T}^{\tau\tau}_{\mathbf{x}}(\tau)}{\bar{T}^{\tau\tau}_{\mathbf{x}}(\tau_0)}. \tag{31}$$

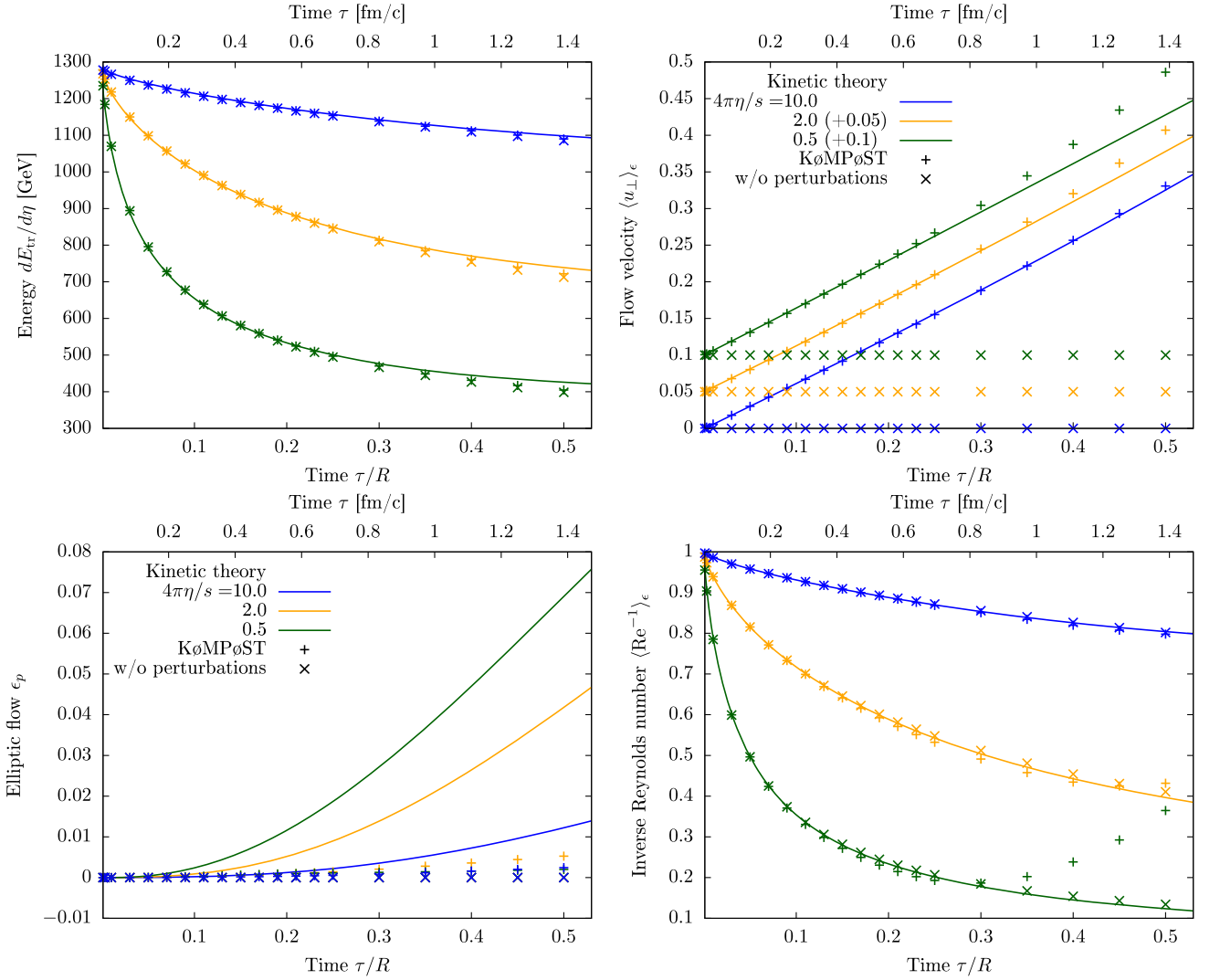

FIG. 1. Time evolution of transverse energy $\mathrm{d}E_{\mathrm{tr}}/\mathrm{d}\eta$ [top left, cf. Eq. (13)], transverse flow velocity $\langle u_\perp \rangle_\epsilon$ [top right, cf. Eq. (15)], elliptic flow ε_p [bottom left, cf. Eq. (14)] and inverse Reynolds number $\langle \mathrm{Re}^{-1} \rangle_\epsilon$ [bottom right, cf. Eq. (16)]. Plotted are results from KøMPøST (RTA) with (+ symbols) and without (× symbols) energy perturbations compared to full kinetic theory results (solid lines) at three different opacities $4\pi\eta/s = 0.5$ (green), 2 (yellow) and 10 (blue). In the plot of transverse flow velocity, results at different opacities are shifted in value in order to be distinguishable.

The Green's functions $G^{\mu\nu}_{\alpha\beta}(\mathbf{x}, \mathbf{x}', \tau, \tau')$ have been computed in the respective underlying kinetic theory description and are included in KøMPøST.

Energy perturbations ($\delta T^{\mu\nu}$) can also be switched off, in which case KøMPøST propagates only the average energy-momentum tensor taken over the causal past, as discussed above. Some of the phenomenological implications of this mode are discussed below. For all other results in this paper, we employed the modified RTA-KøMPøST with energy perturbations.

E. Validation of KøMPøST

Before employing KøMPøST to describe preequilibrium, we first checked to what extent results from modified RTA-KøMPøST are in agreement with results from full kinetic theory in RTA for our specific initial condition. This comparison was done on the basis of the time evolution of the observables we examined in this paper but also for cross sections through profiles of the energy-momentum tensor after some evolution time. All KøMPøST results presented here were obtained using an initial time of $\tau_0 = 10^{-6}R$.

Figure 1 shows a comparison of the time evolution of four different transverse space integrated observables at three different values of the shear viscosity, namely $4\pi\eta/s = 0.5, 2, 10$. The results from KøMPøST are plotted with symbols "+" for the mode with and "×" for the mode without energy perturbations and are benchmarked for times up to $\tau = 0.5R$ against the results obtained using a full kinetic theory description, which are plotted with lines.

The decrease of transverse energy $\mathrm{d}E_{\mathrm{tr}}/\mathrm{d}\eta$ is described very well in both modes. As without energy perturbations, the energy-momentum tensor is propagated as if there were no local gradients, it predicts zero transverse flow velocity $\langle u_\perp \rangle_\epsilon$ and elliptic flow ε_p. The mode with energy

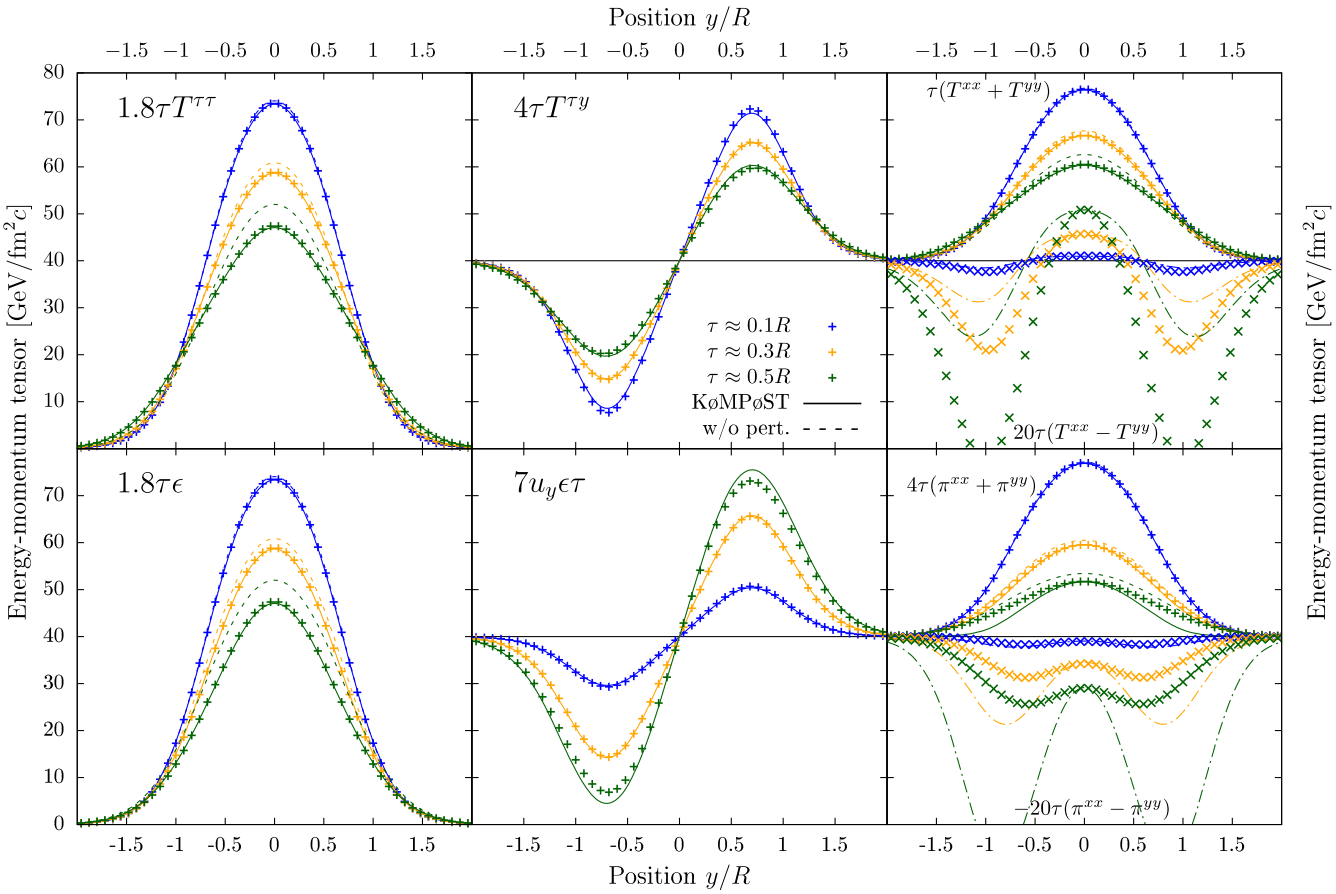

FIG. 2. Comparison of KøMPøST (RTA) and full kinetic theory via results for the energy-momentum tensor on the line $x = 0$, represented at fixed times $\tau/R \simeq 0.1$ in blue, 0.3 in yellow and 0.5 in green. The full kinetic theory results are plotted with points (+,×), while the KøMPøST ones obtained with and without energy perturbations are plotted with solid and dashed lines, respectively. Anisotropic observables are nonzero only with energy perturbations and are plotted with point-dashed lines. The upper row shows, from left to right, the following components of the energy-momentum tensor: $T^{\tau\tau}$ (left), $T^{\tau y}$ (middle), as well as $T^{xx} + T^{yy}$ and $T^{xx} - T^{yy}$ (right). The lower row shows analogous local rest-frame quantities, namely ϵ (left), ϵu^y (middle), as well as $\pi^{xx} + \pi^{yy}$ and $\pi^{yy} - \pi^{xx}$ (right). Notice the change in sign for the latter when compared to the upper panel. All observables were multiplied with τ and rescaled with a constant factor to adjust their magnitudes such that they can be plotted on the same total range of 80 GeV/fm^2 c.

perturbations can describe the buildup of $\langle u_\perp \rangle_\epsilon$ correctly. On the other hand, while giving nonzero results, it still vastly underestimates the buildup of anisotropic flow ε_p. The inverse Reynolds number $\langle \mathrm{Re}^{-1} \rangle_\epsilon$ is well described by both modes at early times, but results from the mode with energy perturbations deviate at very late times.

Generally, the comparison suggests that, for certain observables, KøMPøST results can be accurate way beyond the timeframe it was intended for, which is on the order of 0.1 fm. Other observables, in particular those related to anisotropies, are not described correctly.

In a further comparison of KøMPøST to full kinetic theory data, we also investigated profiles of certain components of $T^{\mu\nu}$ at fixed shear viscosity $4\pi\eta/s = 2$ and three different fixed times $\tau = 0.1R$, $0.3R$ and $0.5R$. The same comparisons were also performed in the local rest frame with analogous quantities that are defined via the variables ϵ, u^μ and $\pi^{\mu\nu}$. Figure 2 illustrates our findings. This time, KøMPøST results are plotted with lines and full kinetic theory results with symbols.

The results confirm that for energy or energy flow observables like $T^{\tau\tau}$, $T^{\tau y}$ and $T^{xx} + T^{yy}$, KøMPøST works well even on a local level and in the outskirts of the system for all evolution times that we examined. The only part of the energy-momentum tensor for which KøMPøST results shows significant deviations are anisotropies in the shear stress, as measured by $T^{xx} - T^{yy}$. While this observable is still correctly reproduced in the central part of the system, it exhibits sizeable deviations of up to a factor of five at a radial distance of $r \gtrsim R$. These deviations also explain the errors in elliptic flow ε_p.

IV. EARLY TIME DYNAMICS OF DIFFERENT MODELS

Before the onset of transverse expansion, at times $\tau \ll R$, the system's dynamics is dominated by longitudinal expansion and the effects of transverse expansion can be neglected. Under these conditions, at each point in the transverse plane, the system evolves independently of the transverse neighborhood and can locally be described by $(0+1)$D longitudinally boost-invariant Bjorken flow. In Bjorken flow, the trajectories of energy, pressure and stress for different initial conditions are known to rapidly converge to a common time evolution curve called the Bjorken flow attractor curve [59,60]. This means that at late times the system always evolves in the same way. If it is initialized on the attractor, then its entire time evolution is given by the attractor curve. We will describe the features of the attractor scaling solution for both the Müller-Israel-Stewart-type second-order hydrodynamics theory and for the conformal kinetic theory in RTA. In Sec. IV A, the quantities describing the attractor solutions are introduced. Sections IV B and IV C discuss how the preequilibrium evolution impacts the observables of interest, highlighting the possible discrepancies between RTA, viscous hydrodynamics and ideal hydrodynamics. Finally, in Sec. IV D, we discuss how viscous and ideal hydrodynamics can be brought in agreement with RTA at late times by scaling the initial conditions.

A. Bjorken attractor

The $(0+1)$D Bjorken flow can be described in terms of the Bjorken coordinates (τ, x, y, η), with respect to which the velocity becomes $u^\mu \partial_\mu = \partial_\tau$. The energy-momentum tensor takes the diagonal form

$$T^{\mu\nu} = \mathrm{diag}(\epsilon, P_T, P_T, \tau^{-2} P_L), \tag{32}$$

where P_T and P_L are the transverse and longitudinal pressures, respectively. The shear-stress tensor also becomes diagonal,

$$\pi^{\mu\nu} = \mathrm{diag}\left(0, -\frac{1}{2}\pi_d, -\frac{1}{2}\pi_d, \frac{1}{\tau^2}\pi_d\right), \tag{33}$$

where π_d can be related to P_T and P_L via

$$P_T = P - \frac{\pi_d}{2}, \qquad P_L = P + \pi_d, \tag{34}$$

such that $\pi_d = \frac{2}{3}(P_L - P_T)$. The observables of interest for the following section are the inverse Reynolds number defined in Eq. (16), and the sum $\epsilon_{\mathrm{tr}} = T^{xx} + T^{yy}$, which become

$$\mathrm{Re}^{-1} = -\frac{3\pi_d}{\epsilon}, \qquad \epsilon_{\mathrm{tr}} = \frac{2\epsilon}{3} - \pi_d = \frac{\epsilon}{3}(2 + \mathrm{Re}^{-1}). \tag{35}$$

The evolution of the energy density ϵ is governed by the conservation equation $\nabla_\mu T^{\mu\nu}$, where ∇_μ is the covariant derivative, which reduces to

$$\tau \frac{\partial \epsilon}{\partial \tau} + \frac{4}{3}\epsilon + \pi_d = 0. \tag{36}$$

In ideal hydrodynamics, $\pi_d = 0$ and $\tau^{4/3}\epsilon(\tau) = \tau_0^{4/3}\epsilon_0$, where ϵ_0 is the energy density at initial time τ_0.

In RTA, the dynamics of π_d is governed directly by the Boltzmann equation. In viscous hydrodynamics, the evolution of π_d can be found from Eq. (28) and reads:

$$\tau \frac{\partial \pi_d}{\partial \tau} + \left(\lambda + \frac{4\pi\tilde{w}}{5} + \frac{2\pi\tilde{w}}{5}\phi_7 \pi_d\right)\pi_d + \frac{16\epsilon}{45} = 0, \tag{37}$$

where $\tilde{w}$ is the conformal parameter,

$$\tilde{w} = \frac{5\tau}{4\pi\tau_\pi} = \frac{\tau T}{4\pi\eta/s}. \tag{38}$$

In the above, $s = (\epsilon + P)/T$ is the entropy density for an ultrarelativistic gas at vanishing chemical potential, while

$\eta = \frac{4}{5}\tau_\pi P$, as shown in Eq. (29). In Eq. (37), we introduced the notation

$$\lambda = \frac{\delta_{\pi\pi}}{\tau_\pi} + \frac{\tau_{\pi\pi}}{3\tau_\pi}, \tag{39}$$

which evaluates to $38/21$ when using the values for the second-order transport coefficients given in Eq. (29). We note that in the original MIS theory, λ evaluates to $4/3$, while the value $31/15$ was advocated in Ref. [65] in order to mimic the early time attractor of RTA.

Equations (36) and (37) admit scaling solutions with respect to the conformal parameter $\tilde{w}$. To see this, we note that the time derivative of $\tilde{w}$ satisfies

$$\tau\frac{\mathrm{d}\tilde{w}}{\mathrm{d}\tau} = \tilde{w}\left(\frac{2}{3} - \frac{f_\pi}{4}\right), \tag{40}$$

where we defined

$$f_\pi = \frac{\pi_d}{\epsilon}. \tag{41}$$

Using Eqs. (36), (37) and (40), f_π can be shown to satisfy

$$\tilde{w}\left(\frac{2}{3} - \frac{f_\pi}{4}\right)\frac{\mathrm{d}f_\pi}{\mathrm{d}\tilde{w}} + \frac{16}{45} + \left(\lambda - \frac{4}{3} + \frac{4\pi\tilde{w}}{5} + \frac{2\pi\tilde{w}}{5}\phi_7\epsilon f_\pi - f_\pi\right)f_\pi = 0, \tag{42}$$

where $\phi_7 = 0$ for consistency with RTA [see Eq. (29)]. Demanding that f_π remains finite when $\tilde{w} \to 0$, its early time behavior in viscous hydro can be obtained as

$$f_\pi(\tilde{w} \ll 1) = f_{\pi;0} + f_{\pi;1}\tilde{w} + f_{\pi;2}\tilde{w}^2 + O(\tilde{w}^3), \tag{43}$$

where

$$f_{\pi;0} = \frac{1}{2}\left[\lambda - \frac{4}{3} - \sqrt{\left(\lambda - \frac{4}{3}\right)^2 + \frac{64}{45}}\right],$$
$$f_{\pi;1} = \frac{\frac{16\pi}{25}f_{\pi;0}^2}{(f_{\pi;0} - \frac{4}{15})^2 + \frac{16}{75}}\left(1 + \frac{1}{2}\phi_7\epsilon f_{\pi;0}\right),$$
$$f_{\pi;2} = \frac{\frac{8\pi}{15}f_{\pi;0}f_{\pi;1}}{(f_{\pi;0} - \frac{4}{9})^2 + \frac{16}{405}}\left(1 - \frac{25f_{\pi;1}}{16\pi} + f_{\pi;0}\phi_7\epsilon\right). \tag{44}$$

When $\lambda = 38/21$, we find $f_{\pi;0} = \frac{1}{105}(25 - 3\sqrt{505}) \simeq -0.404$, which is different from the limit $-1/3$ in kinetic theory.[2] At large values of $\tilde{w}$, $f_\pi(\tilde{w})$ behaves like

$$f_\pi(\tilde{w} \gg 1) = -\frac{4}{9\pi\tilde{w}} + O(\tilde{w}^{-2}), \tag{45}$$

which is the leading order gradient expansion [54] and therefore valid in both viscous hydrodynamics and in RTA. Due to the relations in Eq. (35), our observable $\mathrm{Re}^{-1} = -3f_\pi$ also exhibits attractor behavior. Its attractor curve is represented as a function of $\tilde{w}$ in the top panel of Fig. 3. Its asymptotic forms at small and large $\tilde{w}$ can be found from Eqs. (43) and (45), respectively.

We now turn to the energy equation, Eq. (36). On the attractor, when f_π depends only on $\tilde{w}$, it is possible to write (cf. [59,67])

$$\tau^{4/3}\epsilon(\tau) = \frac{\tau_0^{4/3}\epsilon_0}{\mathcal{E}(\tilde{w}_0)}\mathcal{E}(\tilde{w}), \tag{46}$$

where the scaling function $\mathcal{E}(\tilde{w})$ satisfies

$$\tilde{w}\left(\frac{2}{3} - \frac{f_\pi}{4}\right)\frac{\mathrm{d}\mathcal{E}}{\mathrm{d}\tilde{w}} + f_\pi\mathcal{E} = 0. \tag{47}$$

Due to Eq. (35), ϵ_{tr} also admits a scaling solution,

$$\tau^{4/3}\epsilon_{\mathrm{tr}}(\tau) = \frac{\tau_0^{4/3}\epsilon_0}{\mathcal{E}(\tilde{w}_0)}\mathcal{E}_{\mathrm{tr}}(\tilde{w}),$$
$$\mathcal{E}_{\mathrm{tr}}(\tilde{w}) = \left(\frac{2}{3} - f_\pi(\tilde{w})\right)\mathcal{E}(\tilde{w}). \tag{48}$$

For $\tilde{w} \ll 1$, $\mathcal{E}(\tilde{w})$ can be obtained as

$$\mathcal{E}(\tilde{w} \ll 1) = C_\infty^{-1}\tilde{w}^\gamma(1 + \mathcal{E}_1\tilde{w} + \ldots), \tag{49}$$

where the exponent γ and the correction $\mathcal{E}_1$ are given by

$$\gamma = \frac{12f_{\pi;0}}{3f_{\pi;0} - 8}, \qquad \mathcal{E}_1 = -\frac{\frac{32}{3}f_{\pi;1}}{(f_{\pi;0} - \frac{8}{3})^2}. \tag{50}$$

The constant C_∞ appearing in Eq. (49) is taken such that $\lim_{\tilde{w}\to\infty}\mathcal{E}(\tilde{w}) = 1$, in which case $\mathcal{E}$ has the following late-time asymptotic behavior:

$$\mathcal{E}(\tilde{w} \gg 1) = 1 - \frac{2}{3\pi\tilde{w}}. \tag{51}$$

In the case of ideal hydrodynamics, obviously $f_\pi = 0$ (such that $f_{\pi;0} = \gamma = 0$) and $\mathcal{E}(\tilde{w}) = C_\infty = 1$. The functions $\mathcal{E}(\tilde{w})$ and $\mathcal{E}_{\mathrm{tr}}(\tilde{w})$ are shown in the bottom panel of Fig. 3 for both viscous hydrodynamics and for kinetic theory. The normalization factor C_∞ can be obtained in each theory by computing the attractor curve [59]. For completeness, we list below the values of γ and C_∞ in the relevant theories:

$$\text{RTA:} \quad \gamma = \frac{4}{9}, \quad C_\infty \simeq 0.88, \tag{52a}$$

$$\text{Visc Hydro:} \quad \gamma = \frac{\sqrt{505} - 13}{18}, \quad C_\infty \simeq 0.80, \tag{52b}$$

$$\text{Ideal Hydro:} \quad \gamma = 0, \quad C_\infty = 1. \tag{52c}$$

[2]Expressing $\lambda = f_{\pi;0} + \frac{4}{3} - \frac{16}{45f_{\pi;0}}$, it can be seen that $f_{\pi;0} = -1/3$ leads to $\lambda = 31/15$, as pointed out in Ref. [65].

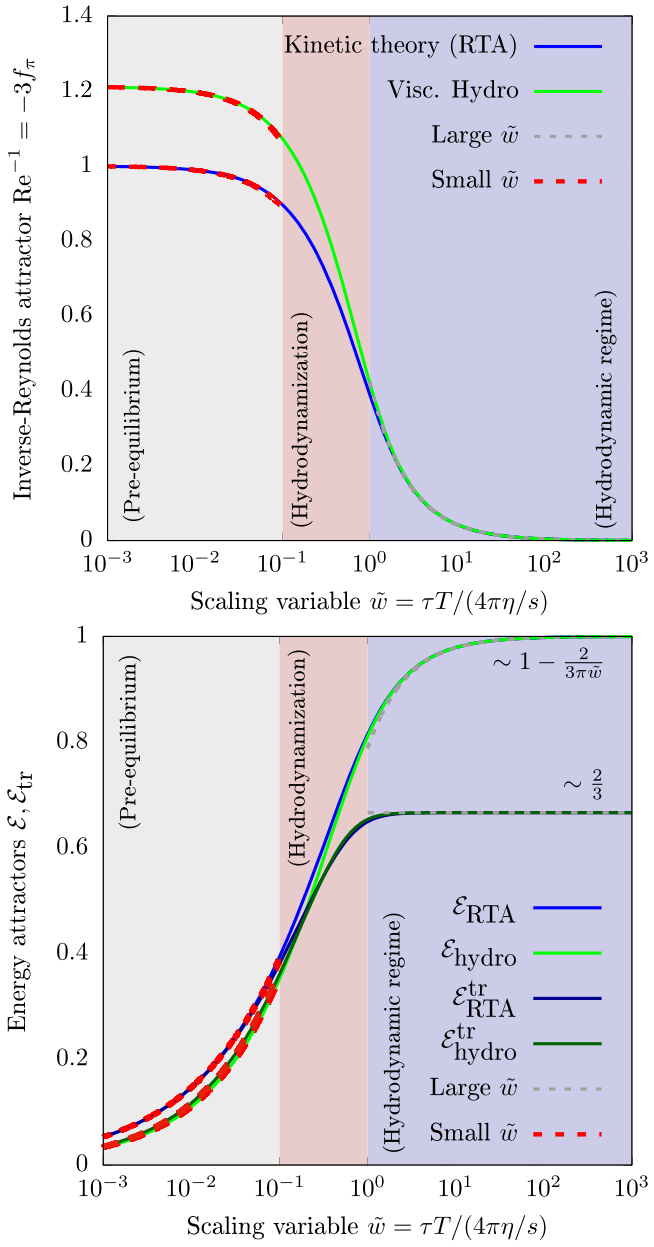

FIG. 3. Attractor curves for the scaling functions (top) Re^{-1} [cf. Eq. (35)], (bottom) $\mathcal{E}(\tilde{w})$ [upper two curves, light colors, cf. Eq. (46)] and $\mathcal{E}_{\mathrm{tr}}(\tilde{w})$ [lower two curves, dark colors, cf. Eq. (48)] obtained for RTA (blue) and for second-order hydrodynamics (green). The large-$\tilde{w}$ asymptotics are shown with dashed gray curves. The small-$\tilde{w}$ asymptotics are shown with black and red dashed curves for RTA and hydro, respectively.

Due to the normalization $\lim_{\tilde{w}\to\infty}\mathcal{E}(\tilde{w}) = 1$, the quantities $\tau^{-2/3}\tilde{w}$ and $\tau^{4/3}\epsilon$ can be rewritten as

$$\tau^{-2/3}\tilde{w} = (\tau^{-2/3}\tilde{w})_\infty \mathcal{E}^{1/4}(\tilde{w}), \tag{53a}$$

$$\tau^{4/3}\epsilon = (\tau^{4/3}\epsilon)_\infty \mathcal{E}(\tilde{w}), \tag{53b}$$

where $(\tau^{-2/3}\tilde{w})_\infty$ and $(\tau^{4/3}\epsilon)_\infty$ represent the corresponding asymptotic, late-time hydrodynamic limits, satisfying

$$(\tau^{-2/3}\tilde{w})_\infty = \frac{(\tau^{4/3}\epsilon)_\infty^{1/4}}{a^{1/4}4\pi\eta/s}, \qquad (\tau^{4/3}\epsilon)_\infty = \frac{\tau_0^{4/3}\epsilon_0}{\mathcal{E}(\tilde{w}_0)}. \tag{54}$$

Taking now the initial time such that $\tilde{w}_0 \ll 1$, Eq. (49) can be used to obtain

$$(\tau^{4/3}\epsilon)_\infty \simeq C_\infty \left(\frac{4\pi\eta}{s}a^{1/4}\right)^{\gamma}\left(\tau_0^{(\frac{4}{3}-\gamma)/(1-\gamma/4)}\epsilon_0\right)^{1-\gamma/4}. \tag{55}$$

Equation (55) tells us that the equilibration dynamics introduce a nontrivial relation between energy densities in equilibrium and in the initial state, as the dependence is nonlinear and the exponents depend on the model description, which was one of the main points of Ref. [59].

In the preequilibrium regime, $\tilde{w} \ll 1$. Under the early time approximation (49), $\tilde{w}$ can be written in terms of $(\tau^{-2/3}\tilde{w})_\infty$ as

$$\tilde{w} \simeq \tau^{\frac{2}{3}/(1-\gamma/4)}[C_\infty^{-1/4}(\tau^{-2/3}\tilde{w})_\infty]^{1/(1-\gamma/4)}, \tag{56}$$

which allows $\epsilon(\tilde{w} \ll 1)$ to be obtained as

$$\epsilon(\tilde{w} \ll 1) \simeq \tau^{(\gamma-\frac{4}{3})/(1-\gamma/4)} \times \left[C_\infty^{-1}\left(\frac{4\pi\eta}{s}a^{1/4}\right)^{-\gamma}(\tau^{4/3}\epsilon)_\infty\right]^{1/(1-\gamma/4)}. \tag{57}$$

Substituting the expression (55) for $(\tau^{4/3}\epsilon)_\infty$ manifestly shows that $\tau^{(\frac{4}{3}-\gamma)/(1-\gamma/4)}\epsilon$ becomes independent of τ as $\tau \to 0$:

$$\epsilon(\tilde{w} \ll 1) \simeq \left(\frac{\tau_0}{\tau}\right)^{(\frac{4}{3}-\gamma)/(1-\frac{\gamma}{4})}\epsilon_0. \tag{58}$$

B. Preequilibrium evolution

We now consider a system which is no longer homogeneous in the transverse plane, such that the energy density becomes a function of both τ and $\mathbf{x}_\perp$, $\epsilon \equiv \epsilon(\tau, \mathbf{x}_\perp)$. At early times $\tau \ll R$ we can neglect transverse dynamics and describe the dynamics locally by Bjorken flow (we will discuss early time transverse expansion effects on the buildup of flow in the Sec. IV C). Under this approximation, at each point $\mathbf{x}_\perp$ of the transverse plane, we can assume that $\epsilon(\tau, \mathbf{x}_\perp)$ follows an evolution along the attractor curve according to the local value of the conformal variable, $\tilde{w} \equiv \tilde{w}(\tau, \mathbf{x}_\perp)$. Moreover, we consider that $\tilde{w}_0(\mathbf{x}_\perp) \ll 1$ throughout the system, such that the full preequilibrium evolution is captured during the system's evolution.

Neglecting the dynamics in the transverse plane, such that $T^{xx} = T^{yy} = \frac{1}{2}\epsilon_{\rm tr}$, $dE_{\rm tr}/d\eta$ defined in Eq. (13) can be written as

$$\frac{dE_{\rm tr}}{d\eta} = \tau \int_{\mathbf{x}_\perp} \left(\frac{2}{3} - f_\pi\right)\epsilon, \tag{59}$$

where Eq. (35) was employed to replace $\epsilon_{\rm tr}$ and $f_\pi = -{\rm Re}^{-1}/3$. Using now Eqs. (53b) and (55) to replace ϵ, we arrive at

$$\frac{dE_{\rm tr}}{d\eta} = \tau^{-1/3} a \left(\frac{4\pi\eta}{s}\right)^{\gamma} \int_{\mathbf{x}_\perp} \left(\tau_0^{(\frac{4}{3}-\gamma)/(1-\gamma/4)} \frac{\epsilon_0}{a}\right)^{1-\frac{\gamma}{4}} \times \left(\frac{2}{3} - f_\pi\right) C_\infty \mathcal{E}. \tag{60}$$

The above equation can be employed to estimate the evolution of $dE_{\rm tr}/d\eta$ due solely to longitudinal expansion over the whole range of τ.

At a fixed value of τ, the conformal parameter $\tilde{w}$ spans the interval 0 (reached at infinitely large distances from the system's center of mass) up to the value $\tilde{w}_{\rm max}$ corresponding to the maximum value of the temperature. For sufficiently small values of τ, $\tilde{w}_{\rm max} \ll 1$ and Eqs. (43), (58) can be used to approximate f_π and ϵ, leading to

$$\frac{dE_{\rm tr}}{d\eta} \simeq \left(\frac{\tau_0}{\tau}\right)^{\frac{1}{3}(1-9\gamma/4)/(1-\gamma/4)} \frac{dE_{\rm tr}^0}{d\eta}. \tag{61}$$

The above relation shows that in RTA ($\gamma = 4/9$), $dE_{\rm tr}/d\eta$ remains constant during preequilibrium. Conversely, in viscous hydrodynamics, $\gamma > 4/9$ and consequently $dE_{\rm tr}/d\eta$ increases with time. As expected, in ideal hydrodynamics, $dE_{\rm tr}/d\eta$ decreases as $\tau^{-1/3}$.

In the limit $\tilde{w} \gg 1$, $f_\pi \sim \tilde{w}^{-1}$ and $\mathcal{E} \simeq 1$, as shown in Eqs. (45) and (51), such that $\tau^{4/3}\epsilon$ can be approximated by $(\tau^{4/3}\epsilon)_\infty$ by virtue of Eq. (53b). Using Eq. (55), $dE_{\rm tr}/d\eta$ reduces to

$$\frac{dE_{\rm tr}}{d\eta} \simeq \frac{2\tau^{-1/3}}{3} C_\infty \left(\frac{4\pi\eta}{s} a^{1/4}\right)^{\gamma} \tau_0^{\frac{4}{3}-\gamma} \int_{\mathbf{x}_\perp} \epsilon_0^{1-\gamma/4}. \tag{62}$$

The above equation shows that, at late times, $dE_{\rm tr}/d\eta$ decrease as $\tau^{-1/3}$. The amount of energy available at a given time τ depends explicitly on the dynamical theory (ideal and viscous hydrodynamics, RTA).

We now consider another important effect arising due to the preequilibrium evolution, namely inhomogeneous cooling. During preequilibrium, neighboring points in the transverse plane undergo cooling at differing rates according to their local attractors. As pointed out in Refs. [59,71], the characteristics of the inhomogeneities in the transverse plane change during preequilibrium, as can be seen by looking at the eccentricity ϵ_n, defined as

$$\epsilon_n = -\frac{\int_{\mathbf{x}_\perp} x_\perp^n \epsilon \cos[n(\phi_x - \Psi_n)]}{\int_{\mathbf{x}_\perp} x_\perp^n \epsilon}. \tag{63}$$

When $\tilde{w} \ll 1$, Eq. (58) can be employed to show that $\epsilon_n(\tau) \simeq \epsilon_n(\tau_0)$ and the eccentricities ϵ_n remain constant during pre-equilibrium. When $\tilde{w} \gg 1$, ϵ_n is modified to

$$\epsilon_n \simeq -\frac{\int_{\mathbf{x}_\perp} x_\perp^n \epsilon_0^{1-\gamma/4} \cos[n(\phi_x - \Psi_n)]}{\int_{\mathbf{x}_\perp} x_\perp^n \epsilon_0^{1-\gamma/4}}. \tag{64}$$

The above relation shows that inhomogeneous cooling leads to modifications of all eccentricities of the initial profile, except in the case of ideal hydrodynamics ($\gamma = 0$).

The effects of the different behavior for global and inhomogeneous cooling in different model descriptions are illustrated in Fig. 4. It shows the preequilibrium evolution of the energy density profile multiplied by the Bjorken time, $\tau\epsilon$, for an example event in the 30–40% centrality class of Pb-Pb collisions in kinetic theory and viscous hydrodynamics with either the same or a scaled initial condition. At very early times, this quantity is constant in kinetic theory, but later it decreases slightly due to equilibration. Meanwhile, in hydrodynamics it increases first before transitioning to a decreasing trend. The speed of these transitions in both cases depends on the local temperature, meaning that e.g. the peak values will start decreasing earlier than the values in the outskirts of the system; i.e. the system cools inhomogeneously. After equilibration, the time evolution will uniformly follow the same power law in both models, but the differences

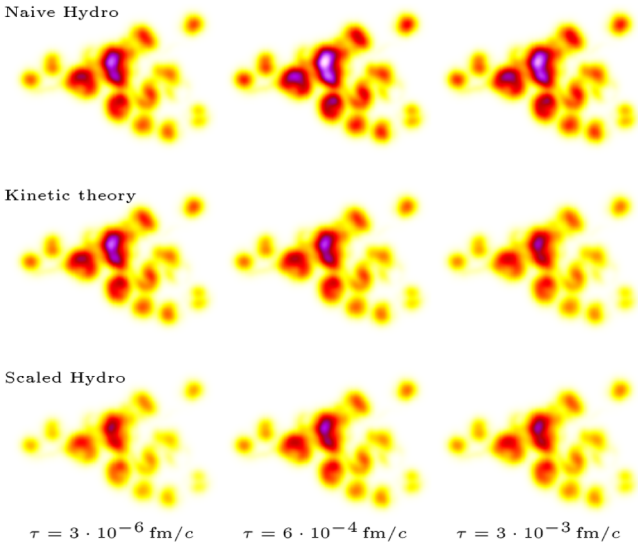

FIG. 4. Early time evolution of the transverse profile of the rest frame energy density $\tau\epsilon$ for an example event in the 30–40% centrality class of Pb-Pb collisions in naive viscous hydrodynamics (top), kinetic theory (middle) and scaled viscous hydrodynamics (bottom) at an opacity $4\pi\eta/s = 0.05$.

due to the different preequilibrium evolution will persist. But the knowledge of the local attractor scaling behavior allows us to anticipate the differences between kinetic theory and hydrodynamics and apply a corresponding local scaling prescription to the initial condition of hydro. It then initially takes smaller values than in kinetic theory but dynamically approaches it during preequilibrium and reaches agreement after equilibration. This initialization scheme is explained in more detail in Sec. IV D.

C. Preflow estimation

We now estimate the buildup of flow during the preequilibrium evolution, which we quantify via the observable $\langle u_\perp \rangle_\epsilon$ defined in Eq. (15). The basis of our analysis is to consider that the transverse dynamics represent a small perturbation on top of the purely-longitudinal dynamics discussed in Secs. IV A and IV B, which we consider to be dominant. The idea of this calculation is similar to the one presented in Ref. [134].

At early times $\tau \ll R$, when the transverse flow is negligible, we can write $T^{\mu\nu} = T^{\mu\nu}_B + \delta T^{\mu\nu}$, where $T^{\mu\nu}_B = \mathrm{diag}(\epsilon_B, P_{B;T}, P_{B;T}, \tau^{-2} P_{B;L})$ is the background (Bjorken) solution of the local, equivalent $(0+1)$D system (we also consider that at initial time $\tilde{w}_0 \ll 1$ throughout the transverse plane). Further assuming that $\delta T^{\mu\nu}$ is small and imposing the Landau frame condition, $T^\mu_\nu u^\nu = \epsilon u^\mu$, we write $u^\mu = u^\mu_B + \delta u^\mu$ and $\epsilon = \epsilon_B + \delta\epsilon$ and find

$$\delta\epsilon = \delta T^{\tau\tau}, \qquad \delta u^i = \frac{\delta T^{\tau i}}{\epsilon_B + P_{B;T}}, \tag{65}$$

while $\delta u^\tau = 0$ as required by $u^\mu_B \delta u_\mu = 0$. Thus, the flow buildup can be estimated from the buildup of $\delta T^{\tau i}$.

We can now derive a dynamical equation for $T^{\tau i}$ via the conservation equation $\nabla_\mu T^{\mu\nu} = 0$, which in a general coordinate system reads

$$\nabla_\mu T^{\mu\nu} = \partial_\mu T^{\mu\nu} + \Gamma^\mu{}_{\lambda\mu} T^{\lambda\nu} + \Gamma^\nu{}_{\lambda\mu} T^{\mu\lambda}, \tag{66}$$

where $\Gamma^\lambda{}_{\mu\nu} = \frac{1}{2} g^{\lambda\rho}(\partial_\nu g_{\rho\mu} + \partial_\mu g_{\rho\nu} - \partial_\rho g_{\mu\nu})$ are the Christoffel symbols. In the Bjorken coordinate system (τ, x, y, η), the only nonvanishing Christoffel symbols are $\Gamma^\tau{}_{\eta\eta} = \tau$ and $\Gamma^\eta{}_{\tau\eta} = \Gamma^\eta{}_{\eta\tau} = \tau^{-1}$, such that the equation for $\nu = i$ becomes

$$\frac{1}{\tau}\frac{\partial(\tau T^{\tau i})}{\partial\tau} + \partial_j T^{ij} = 0. \tag{67}$$

Splitting the energy-momentum tensor into a local Bjorken flow part and a small perturbation as discussed above, we find

$$\frac{1}{\tau}\frac{\partial(\tau \delta T^{\tau i})}{\partial\tau} + \partial_i P_{B;T} + \partial_j \delta T^{ij} = 0. \tag{68}$$

Noting that δT^{ij} represents a higher-order correction, the leading-order contribution to $\delta T^{\tau i}$ can be obtained by solving

$$\frac{\partial(\tau \delta T^{\tau i})}{\partial\tau} \simeq -\tau \partial_i P_{B;T}. \tag{69}$$

In the above, $P_{B;T}$ evolves according to the local Bjorken attractor, such that $P_{B;T} \simeq \epsilon_B(\frac{1}{3} - \frac{1}{2} f_{\pi;B})$. Using Eq. (53b) to replace ϵ_B, the spatial gradient of $P_{B;T}$ can be obtained as

$$\frac{\partial_i P_T}{P_T} = \frac{\partial_i(\tau^{4/3}\epsilon)_\infty}{(\tau^{4/3}\epsilon)_\infty} + \left(\frac{\mathcal{E}'}{\mathcal{E}} - \frac{\frac{1}{2} f'_\pi}{\frac{1}{3} - \frac{1}{2} f_\pi}\right)\partial_i \tilde{w}, \tag{70}$$

where the prime denotes differentiation with respect to $\tilde{w}$. Here and henceforth, we will drop the B subscript for brevity, keeping in mind that all instances of P_T, ϵ, f_π and the corresponding conformal variable $\tilde{w}$ are evaluated according to the background $(0+1)$D Bjorken attractor.

Since $(\tau^{4/3}\epsilon)_\infty$ depends on the transverse coordinates only through the initial profile [see Eq. (55)], the first term on the right-hand side of the above relation evaluates in the limit $\tilde{w}_0 \ll 1$ to

$$\frac{\partial_i(\tau^{4/3}\epsilon)_\infty}{(\tau^{4/3}\epsilon)_\infty} = \left(1 - \frac{\gamma}{4}\right)\frac{\partial_i \epsilon_0}{\epsilon_0}. \tag{71}$$

The gradient of $\tilde{w}$ appearing in Eq. (70) can be written in terms of that of $(\tau^{-2/3}\tilde{w})_\infty$ starting from Eq. (53a),

$$\begin{aligned}\frac{\partial_i \tilde{w}}{\tilde{w}} &= \left(1 - \frac{\tilde{w}\mathcal{E}'}{4\mathcal{E}}\right)^{-1} \frac{\partial_i(\tau^{-2/3}\tilde{w})_\infty}{(\tau^{-2/3}\tilde{w})_\infty}, \\ &= \frac{1}{4}\left(1 - \frac{\gamma}{4}\right)\left(1 - \frac{\tilde{w}\mathcal{E}'}{4\mathcal{E}}\right)^{-1} \frac{\partial_i \epsilon_0}{\epsilon_0},\end{aligned} \tag{72}$$

where the equality on the second line is established using the relations (54) and (71). Substituting Eqs. (71) and (72) into Eq. (70) gives

$$\frac{\partial_i P_T}{P_T} = \frac{1 - \gamma/4}{1 - \frac{\tilde{w}\mathcal{E}'}{4\mathcal{E}}}\left(1 - \frac{\tilde{w} f'_\pi}{\frac{8}{3} - 4 f_\pi}\right)\frac{\partial_i \epsilon_0}{\epsilon_0}. \tag{73}$$

Substituting Eq. (73) in Eq. (69) and integrating with respect to τ, we arrive at

$$\delta T^{\tau i} = -\frac{1}{\tau}\left(1 - \frac{\gamma}{4}\right)\frac{\partial_i \epsilon_0}{\epsilon_0}\int_{\tau_0}^{\tau} d\tau \frac{\frac{1}{3} - \frac{1}{2} f_\pi - \frac{\tilde{w}}{8} f'_\pi}{1 - \frac{\tilde{w}}{4\mathcal{E}}\mathcal{E}'}\tau\epsilon. \tag{74}$$

Considering now that $\tilde{w} \ll 1$ throughout the system, we can use Eqs. (49), (43) and (58) to approximate $f_\pi \simeq f_{\pi;0} = -(2\gamma/3)/(1 - \gamma/4)$, $\mathcal{E} \simeq C_\infty^{-1}\tilde{w}^\gamma$ and $\epsilon = (\tau_0/\tau)^{2-\alpha}\epsilon_0$, where $\alpha = (\gamma + 4/3)/[2(1 - \gamma/4)]$, which reduces to $\alpha = 2/3$, 1 and 1.071 in ideal hydro, RTA and viscous hydro, respectively. To leading order, we find

$$\tau^{2-\alpha}\delta T^{\tau i} = -\frac{\tau}{2}\left[1-\left(\frac{\tau_0}{\tau}\right)^{\alpha}\right]\partial_i(\tau_0^{2-\alpha}\epsilon_0), \tag{75}$$

which allows the macroscopic velocity to be estimated as

$$\delta u^i(\tilde{w}\ll 1) \simeq -\frac{3\tau}{8}\left(1-\frac{\gamma}{4}\right)\left[1-\left(\frac{\tau_0}{\tau}\right)^{\alpha}\right]\frac{\partial_i\epsilon_0}{\epsilon_0}. \tag{76}$$

As expected, the flow velocity is driven by the gradients of the initial energy density profile. In addition, when $\tau \gg \tau_0$, δu^i exhibits a linear increase with τ, independently of the value of γ. The prefactor governing the overall amplitude of δu^i is however γ dependent. We can now estimate the early time evolution of $\langle u_\perp\rangle_\epsilon$, defined in Eq. (15), as follows:

$$\langle u_\perp\rangle_{\epsilon,\text{early}} \simeq \frac{3\tau}{8}\left(1-\frac{\gamma}{4}\right)\left[1-\left(\frac{\tau_0}{\tau}\right)^{\alpha}\right] \times\left(\int_{\mathbf{x}_\perp}\epsilon_0\right)^{-1}\int_{\mathbf{x}_\perp}|\nabla_\perp\epsilon_0|, \tag{77}$$

where $|\nabla_\perp\epsilon_0| = [(\partial_x\epsilon_0)^2+(\partial_y\epsilon_0)^2]^{1/2}$.

In general, the time dependence of the integrand in Eq. (74) is too complicated to integrate analytically. But it again takes a simple form in the Bjorken flow equilibrium stage, where $\tau^{4/3}P_T \simeq \frac{1}{3}(\tau^{4/3}\epsilon)_\infty$. At late times, when the duration of preequilibrium is small compared to the elapsed time, its contribution in the time integration is negligible and $\delta T^{\tau i}$ and δu^i asymptote to

$$\delta T^{\tau i}(\tilde{w}\gg 1) \simeq -\frac{1}{2\tau^{1/3}}\left[1-\left(\frac{\tau_0}{\tau}\right)^{2/3}\right]\partial_i(\tau^{4/3}\epsilon)_\infty, \tag{78a}$$

$$\delta u^i(\tilde{w}\gg 1) \simeq -\frac{3\tau}{8}\left[1-\left(\frac{\tau_0}{\tau}\right)^{2/3}\right]\frac{\partial_i(\tau^{4/3}\epsilon)_\infty}{(\tau^{4/3}\epsilon)_\infty}, \tag{78b}$$

such that $\langle u_\perp\rangle_\epsilon$ becomes

$$\langle u_\perp\rangle_{\epsilon,\text{ late}} \simeq \frac{3\tau}{8}\left[1-\left(\frac{\tau_0}{\tau}\right)^{2/3}\right]\frac{\int_{\mathbf{x}_\perp}|\nabla_\perp\epsilon_0^{1-\gamma/4}|}{\int_{\mathbf{x}_\perp}\epsilon_0^{1-\gamma/4}}. \tag{79}$$

Note that the above equation was derived under the assumption that δu^i is small and thus holds only when the system hydrodynamizes before transverse expansion sets in.

The right-hand side of Eqs. (77) and (79) can be evaluated numerically for the 30–40% centrality profile that we are considering in this paper. The results for the different theories (kinetic theory, ideal hydrodynamics and viscous hydrodynamics) are shown in Table II. Here, we contrast the "naive" and "scaled" initial conditions for hydrodynamics, which will be discussed in detail in the following subsection. In the early time regime, it can be seen that kinetic theory leads to more flow than viscous hydrodynamics (2% and 1% more for the naive and scaled initialization, respectively), while ideal hydrodynamics leads to more flow than kinetic theory (13% and 7% more for the naive and scaled initializations, respectively). In the late-time limit, both ideal and viscous hydrodynamics are brought in agreement with kinetic theory when the scaled initialization is employed. In the case of the naive initialization, ideal hydrodynamics gives about 5% more flow, while viscous hydrodynamics underestimates the flow by less than 1%.

TABLE II. Estimates for the preflow generated in kinetic theory, ideal hydrodynamics and viscous hydrodynamics (see Sec. IV D for details regarding the naive and scaled hydrodynamics setups).

	Kinetic theory	Naive hydro		Scaled hydro	
		Ideal	Viscous	Ideal	Viscous
γ	4/9	0	0.526	0	0.526
α	1	2/3	1.071	2/3	1.071
$\frac{R}{\tau}\frac{\langle u_\perp\rangle_{\epsilon,\text{early}}}{1-(\tau_0/\tau)^{\alpha}}$	0.614	0.691	0.600	0.658	0.606
$\frac{R}{\tau}\frac{\langle u_\perp\rangle_{\epsilon,\text{late}}}{1-(\tau_0/\tau)^{2/3}}$	0.658	0.691	0.652	0.658	0.658

D. Setting initial conditions

From the discussion in the previous subsection, it becomes clear that the preequilibrium evolution of the fluid depends on the theory employed to describe it. We take as the "correct" evolution that described by kinetic theory, when $dE_{\text{tr}}/d\eta$ remains constant during the free-streaming stage of preequilibrium. This can be seen by setting $\gamma = 4/9$ in Eq. (61). Since in viscous hydrodynamics, $\gamma \simeq 0.526 > 4/9$, $dE_{\text{tr}}/d\eta$ will actually increase during preequilibrium, thus leading for the same initial energy profile to an unphysically higher transverse plane energy at late times, as illustrated in Fig. 4. Similarly, the change in eccentricity due to the preequilibrium evolution will be different compared to kinetic theory. We will now discuss how these phenomena specifically affect the preequilibrium evolution of our initial state as given in Sec. II A and how they are counteracted by locally scaling the initial condition. We will then give the quantitative details of the scaling prescription.

Figure 5 illustrates the size of the effect on transverse energy $dE_{\text{tr}}/d\eta$ in the top panel and ellipticity ϵ_2 in the bottom panel. In naive hydrodynamics using the same initial condition for the energy density as kinetic theory and initial pressure determined by the hydrodynamic attractor, $dE_{\text{tr}}/d\eta$ rises to a value which is about 1.5 times larger than in kinetic theory at the onset of equilibration and will remain in disagreement throughout the rest of the evolution. The dashed lines show predictions of the behavior in the local Bjorken flow scaling approximation according to Eq. (60). In our proposed scheme the initial value of

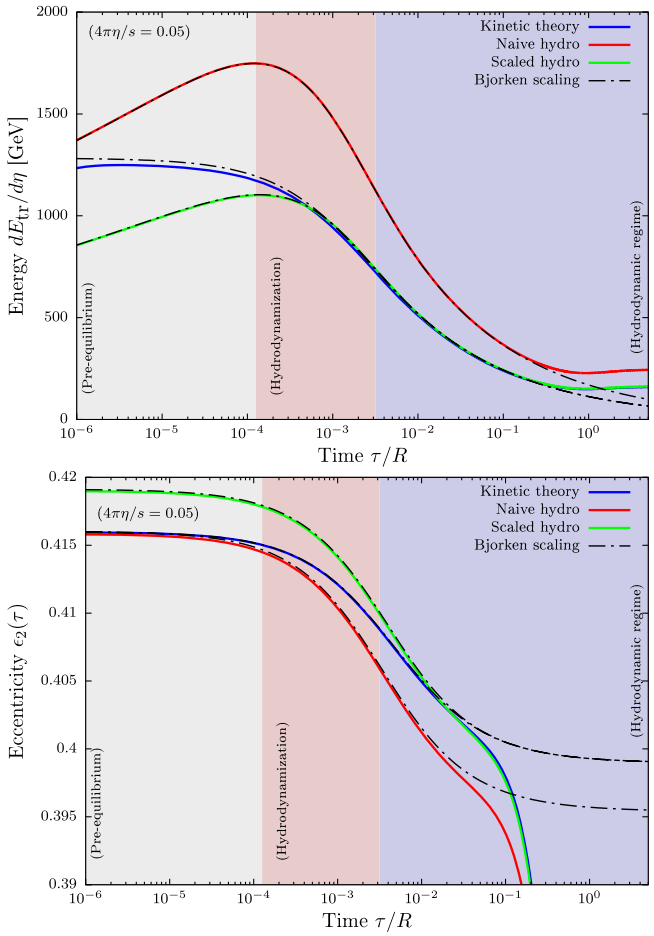

FIG. 5. Early time evolution of transverse energy $\mathrm{d}E_{\mathrm{tr}}/\mathrm{d}\eta$ [top, cf. Eq. (13)] and ellipticity ϵ_2 [bottom, cf. Eq. (5)] in kinetic theory (blue), naive hydrodynamics (red) and scaled hydrodynamics (green). Hydrodynamics behaves differently in preequilibrium, such that differences to a kinetic theory description build up. This can be counteracted by scaling the initial condition.

$\mathrm{d}E_{\mathrm{tr}}/\mathrm{d}\eta$ is scaled down in such a way that it dynamically reaches agreement with kinetic theory. Similarly, we find that the ellipticity decreases in both kinetic theory and in hydro, but more so in the latter case. This means that in naive hydro the eccentricity will have a smaller value at the onset of the buildup of transverse flow than in kinetic theory, which will result in smaller final values of elliptic flow. With the scaling scheme, the initial ellipticity is scaled up in hydrodynamics and will come into agreement with kinetic theory after equilibration.

As the local scaling factor for the hydrodynamic initial condition is computed in the local Bjorken flow approximation, it assumes that the system will fully equilibrate before the onset of transverse expansion. How well this works in practice will be discussed in Sec. V B.

We now move to the quantitative analysis of the preequilibrium behavior in the two hydro schemes. In the first one, dubbed "naive hydrodynamics," we will impose the same energy density ϵ_0 at initial time τ_0 as in kinetic theory. We first note that the RTA initial conditions given in Eq. (1) are not compatible with the hydrodynamic attractor.

Indeed, noting the relations $P_T = \epsilon(\frac{1}{3} - \frac{f_\pi}{2})$ and $P_L = \epsilon(\frac{1}{3} + f_\pi)$, the early time expression for $T^{\mu\nu}$ reads

$$T_0^{\mu\nu} = \epsilon_0 \times \mathrm{diag}\left(1, \frac{1}{3} - \frac{f_\pi}{2}, \frac{1}{3} - \frac{f_\pi}{2}, \frac{1}{3\tau^2} + \frac{f_\pi}{\tau^2}\right), \tag{80}$$

where $f_\pi \equiv f_\pi(\tilde{w}_0)$ depends on the local value of the conformal variable, $\tilde{w}_0 \equiv \tilde{w}_0(\mathbf{x}_\perp) = \tau_0 T_0(\mathbf{x}_\perp)/(4\pi\eta/s)$, with $T_0(\mathbf{x}_\perp) = [\epsilon_0(\mathbf{x}_\perp)/a]^{1/4}$. In order to evaluate $f_\pi(\tilde{w}_0)$, we follow Ref. [135] and employ a simple Padé approximation interpolating between the $\tilde{w} \ll 1$ and $\tilde{w} \gg 1$ limits given in Eqs. (43) and (45):

$$f_\pi(\tilde{w}) \simeq \frac{c_0 + c_1\tilde{w}}{d_0 + d_1\tilde{w} + d_2\tilde{w}^2}, \tag{81}$$

where the coefficients c_0, c_1, d_0, d_1 and d_2 are computed to ensure second order accuracy at small $\tilde{w}$ and first order accuracy at large $\tilde{w}$:

$$d_0 = \frac{4f_{\pi;1}}{9\pi} - f_{\pi;0}^2, \quad d_1 = f_{\pi;0}f_{\pi;1} - \frac{4f_{\pi;2}}{9\pi},$$
$$d_2 = f_{\pi;0}f_{\pi;2} - f_{\pi;1}^2, \quad c_0 = d_0 f_{\pi;0}, \quad c_1 = -\frac{4d_2}{9\pi}. \tag{82}$$

The coefficients $f_{\pi;0}, f_{\pi;1}$ and $f_{\pi;2}$ are given in Eq. (44). In the limit $\tilde{w} \to 0$, when $f_\pi \to f_{\pi;0} = -\frac{2\gamma}{3}/(1-\gamma/4)$, Eq. (80) reduces to

$$T_0^{\mu\nu} = \frac{\epsilon_0}{1-\gamma/4}\mathrm{diag}\left(1 - \frac{\gamma}{4}, \frac{1}{3} + \frac{\gamma}{4}, \frac{1}{3} + \frac{\gamma}{4}, \frac{1}{3\tau^2} - \frac{3\gamma}{4\tau^2}\right), \tag{83}$$

which coincides with the initialization employed for RTA [shown in Eq. (1)] in the case when $\gamma = 4/9$. Since in hydrodynamics, $\gamma > 4/9$, the initial transverse-plane energy when $\tilde{w}_0 \ll 1$ will be larger than in RTA:

$$\frac{\mathrm{d}E^0_{\mathrm{tr};\gamma}}{\mathrm{d}\eta} = \frac{2}{3}\frac{1+3\gamma/4}{1-\gamma/4}\frac{\mathrm{d}E^0_{\mathrm{tr;RTA}}}{\mathrm{d}\eta}. \tag{84}$$

This explains why at initial time the naive hydro curve in Fig. 5 starts above the kinetic theory one.

Acknowledging that viscous hydrodynamics does not capture correctly the preequilibrium evolution of the fluid, we propose to change the initialization of hydrodynamics in such a way that the energy density ϵ locally agrees with the kinetic theory prediction at late times. In principle, this works only when the preequilibrium evolution ends before the onset of transverse expansion. Taking a and η/s to be identical in the two theories and demanding that they both

reach the same $(\tau^{4/3}\epsilon)_\infty$ value when $\tau \to \infty$, Eq. (55) shows that the local modification of the initial energy density in hydrodynamics (denoted $\epsilon_{0,\gamma}$) is

$$\epsilon_{0,\gamma} = \left[\left(\frac{4\pi\eta/s}{\tau_0} a^{1/4}\right)^{\frac{1}{2}-\frac{9\gamma}{8}} \left(\frac{C_\infty^{\mathrm{RTA}}}{C_\infty^{\gamma}}\right)^{9/8} \epsilon_{0,\mathrm{RTA}}\right]^{\frac{8/9}{1-\gamma/4}}, \quad (85)$$

where the specific shear viscosity η/s is considered to have the same value in viscous hydrodynamics and in kinetic theory. Using the above energy profile in Eqs. (62), (64) and (79) shows that after preequilibrium (i.e. at large $\tilde{w}$), $\mathrm{d}E_{\mathrm{tr}}/\mathrm{d}\eta$, the eccentricities ϵ_n and the average flow velocity $\langle u_\perp \rangle_\epsilon$ will reach the corresponding RTA limits, irrespective of the value of γ. We note, however, that the preequilibrium behavior of all of the above observables will still be different from that in RTA.

Before ending this section, we emphasize that the rescaling of the initial conditions shown in Eq. (85) is not only possible, but also mandatory for ideal hydrodynamics simulations, when $\gamma = 0$ and $C_\infty = 1$. While when applying the scaling procedure to viscous hydrodynamics, η/s was considered as an invariant physical parameter, in ideal hydrodynamics (when $\eta = 0$), this is no longer the case. Instead, the factor η/s helps rescale the initial energy density such that, at late times, $\tau^{4/3}\epsilon$ obtained in ideal hydrodynamics would match the one in a hypothetical RTA system with that given value of η/s. The agreement between ideal hydro and RTA can be expected of course only in the limit $\eta/s \to 0$. Specifically, Eq. (85) reduces in the case of ideal hydro to

$$\epsilon_{0,\mathrm{id}} = \left(\frac{4\pi\eta}{s}\right)_{\mathrm{RTA}}^{4/9} C_\infty^{\mathrm{RTA}} \frac{a^{1/9}}{\tau_0^{4/9}} \epsilon_{0,\mathrm{RTA}}^{8/9}. \quad (86)$$

When comparing the ideal hydro result to kinetic theory calculations, we employ the above formula with $4\pi\eta/s = 1$, and for $\mathrm{d}E_{\mathrm{tr}}/\mathrm{d}\eta$ we rescale the final results with $(4\pi\eta/s)^{4/9}$ according to Eq. (86) when comparing to kinetic theory at other values of $4\pi\eta/s$.

V. SPACE-TIME EVOLUTION AT DIFFERENT OPACITIES AND IN DIFFERENT SETUPS

The different behavior of hydrodynamics compared to kinetic theory in preequilibrium can best be assessed via the time dependence of the studied observables. This also allows to study the behavior during different stages of the collision. In Sec. V A, we discuss the time evolution of transverse profiles of the system in kinetic theory. Section V B compares the time evolution of the tracked observables in kinetic theory and scaled viscous hydrodynamics. These are then used as the basis for a discussion of the time evolution in hybrid simulation schemes in Sec. V C.

A. Evolution of transverse profiles in kinetic theory

We now want to discuss the system's time evolution at different opacities resolved in transverse space. This is illustrated in Fig. 6 via heat map plots of the timescaled local rest frame energy density $\tau\epsilon$ together with a vector plot of the transverse components of the flow velocity u^μ at three different values of the shear viscosity, $4\pi\eta/s = 0.5$, 3, 10, which are representative of the regimes of hydrodynamic behavior, close-to-free-streaming behavior and the intermediate transitioning regime. The time evolution of these profiles is sampled at three different times, $\tau = 0.1R$, $1R$ and $2R$, which mark the beginning, peak and end of the buildup of elliptic flow ε_p, as will be discussed in Sec. V B.

At the earliest time, $\tau = 0.1R$, transverse dynamics have not had a large effect yet: flow velocities are negligible and the main geometric properties of the profile remain unchanged. The only obvious difference is the overall scale. At smaller η/s, the system starts cooling sooner, performing more work against the longitudinal expansion, resulting in significantly smaller energy densities when compared to larger η/s.

$\tau = 1R$ marks the characteristic time where transverse expansion effects become significant. Here, we see the profile taking on a more circular shape. We also see significant flow velocities, which rise in magnitude with the distance from the center. For smaller shear viscosity η/s, meaning larger interaction rates, the system tends to lump together more, resulting in a smaller spatial extent and smaller flow velocities compared to larger η/s.

At the largest selected time, $\tau = 2R$, the interaction rate in the system has significantly decreased due to the dilution caused by the transverse expansion. Over time, the dynamics will approach a free-streaming expansion in all directions. It is apparent in all three cases that the system has expanded mainly in the directions of larger gradients in the initial state. For small shear viscosity η/s, the system's energy density is still peaked in the center due to stronger collective behavior. On the other hand, at large η/s, the system evolution is closer to a free-streaming propagation of the initial state, resulting in two high-density areas at distances $r \approx \tau$ from the center. Though the difference is barely visible, the built-up flow velocities are larger for larger η/s.

We can discern additional spatially resolved information on the opacity dependence of the system's evolution by also comparing profile plots of the anisotropic stress, $T^{xx} - T^{yy}$, which are presented in Fig. 7. Per definition in Eq. (14), the transverse integral of this quantity is proportional to elliptic flow ε_p, which builds up more at smaller values of η/s. Note that the symmetry-plane phase factor takes the value $e^{2i\Psi_p} = -1$ in this case, such that a negative integral results in positive ε_p. The plots show that the transverse plane separates into regions with different sign of the anisotropic stress. The behavior in the outskirts is dictated by transverse expansion, resulting in positive values in $\pm x$ direction

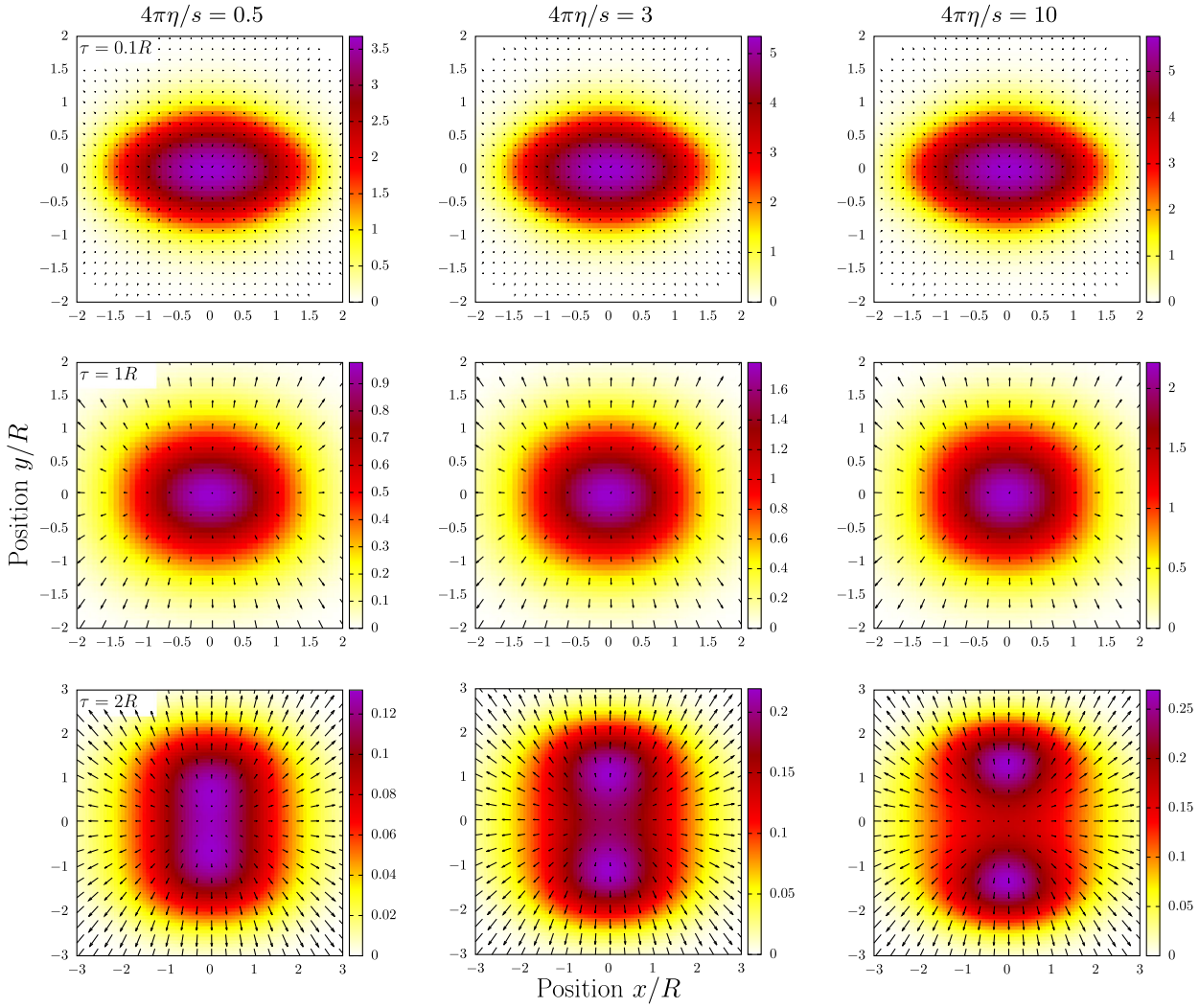

FIG. 6. Time evolution of transverse profiles of the rest frame energy density $\tau\epsilon$ in a heat map plot together with transverse components of the flow velocity (u^x, u^y) as a vector field plot for the averaged initial condition used in this work at different opacities $4\pi\eta/s = 0.5$ (left), 3 (middle) and 10 (right). The snapshot times $\tau = 0.1R$ (top), $\tau = 1R$ (middle) and $\tau = 2R$ (bottom) were chosen as the beginning, peak and end of the buildup of elliptic flow ε_p.

and negative values in $\pm y$ direction. The buildup of elliptic flow seems to proceed mainly via the positive parts decaying more than negative ones. At small opacities in the right panel, particles propagate with few interactions. Due to the initial almond shape, most of the particles in the center propagate in $\pm x$ direction, resulting in a larger T^{xx} than T^{yy}. At large opacities in the left panel, the system is hydrodynamized and the anisotropic stress comes mostly from the direction of flow. Since the flow components u_x and u_y are zero in the center of the system, the anisotropic stress vanishes there.

B. Time evolution of observables in kinetic theory and hydrodynamics

We will now examine the time evolution of certain characteristic transverse space integrated observables in both kinetic theory and the scaled hydrodynamics scheme that was proposed in Sec. IV D as a countermeasure to the unphysical preequilibrium behavior of hydrodynamics discussed in Sec. IV B. This will provide additional insights into the system's behavior but also reveal how well the scaled hydro scheme works at different opacities. Figure 8 shows comparisons of the time evolution of transverse energy $\mathrm{d}E_{\mathrm{tr}}/\mathrm{d}\eta$, elliptic flow ε_p, average transverse flow velocity $\langle u_\perp \rangle_\epsilon$ and average inverse Reynolds number $\langle \mathrm{Re}^{-1} \rangle_\epsilon$ in both models at three different opacities. Since we are using a fixed initial profile, we plot ε_p without normalization to the initial state eccentricity ϵ_2. As an illustration of the motivation for the scaling scheme in hydrodynamics, for $\mathrm{d}E_{\mathrm{tr}}/\mathrm{d}\eta$ and $\langle \mathrm{Re}^{-1} \rangle_\epsilon$ we also compare with the time evolution in the absence of transverse expansion, where we describe the system as a collection of local Bjorken flows.

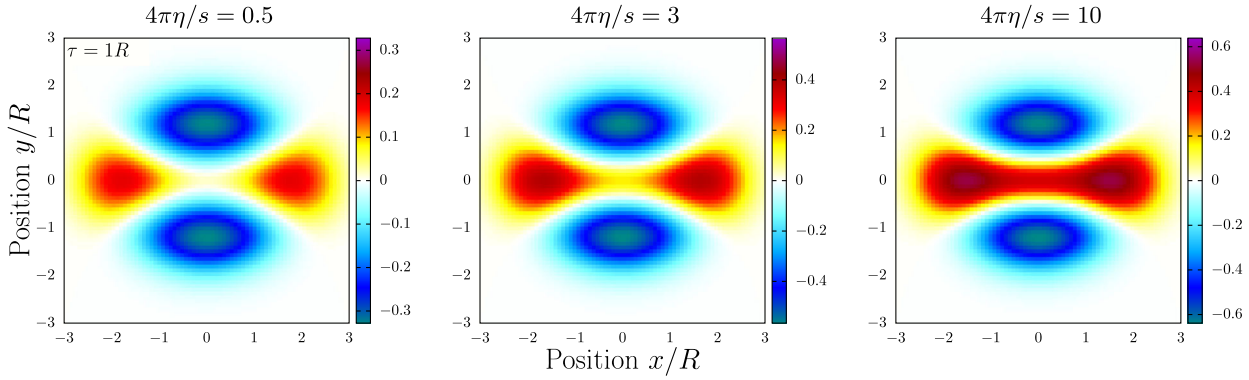

FIG. 7. Transverse profiles of the transverse anisotropy $\tau(T^{xx} - T^{yy})$ in kinetic theory at time $\tau = 1R$ for different opacities $4\pi\eta/s = 0.5$ (left), 3 (middle), 10 (right).

The time evolution of transverse energy $dE_{\mathrm{tr}}/d\eta$ closely follows results from Bjorken flow scaling at early times, as predicted in Sec. IV B. In Bjorken flow scaling, this observable starts out being constant in the free-streaming period of kinetic theory, while, in hydrodynamics, it follows a positive power law, cf. Eq. (61). From there, in both cases the time evolution smoothly transitions to a late time equilibrium power law $dE_{\mathrm{tr}}/d\eta \sim \tau^{-1/3}$. The timescale of this transition depends on the opacity and is smaller at smaller η/s. In RTA,[3] it scales as $\tau_{\mathrm{eq}} \sim (\eta/s)^{4/3}$ [71]. By construction, results from scaled hydrodynamics agree with kinetic theory results in the late time limit of Bjorken flow scaling. The time evolution in full simulations follows this behavior up to times $\tau \sim R$, when effects of transverse expansion become significant. The rapid dilution due to transverse expansion decreases interaction rates and causes $dE_{\mathrm{tr}}/d\eta$ to approach a constant value. For large opacities like $4\pi\eta/s = 0.5$, the Bjorken flow equilibrium where both models agree sets in long before transverse expansion and even afterwards the results will stay in agreement. Intermediate opacities around $4\pi\eta/s = 3$ mark the transition region where results for $dE_{\mathrm{tr}}/d\eta$ from both models just barely come into agreement before approaching a constant value. At small opacities like in the case of $4\pi\eta/s = 10$, the onset of transverse expansion interrupts the Bjorken flow scaling period before the two model descriptions have come into agreement. The residual discrepancy then persists throughout the evolution of the system and leads to a mismatch of final state observables, which becomes worse as η/s is increased.

The second line of Fig. 8 shows the time evolution of the elliptic flow coefficient ε_p. Again, like in the case of $dE_{\mathrm{tr}}/d\eta$, because of the decrease of interaction rates due to the dilution caused by transverse expansion, ε_p reaches a late-time plateau. Thus, at all opacities, ε_p builds up in a time frame of $\tau \lesssim 2R$. Contributions from early times are negligible, such that effectively the buildup starts at $\tau \gtrsim 0.1R$. As indicated in the log-log insets, the kinetic theory curves exhibit at early times an approximate power-law increase, $\varepsilon_p \propto \tau^{8/3}$. In contrast, the scaled hydro curve for ε_p first dips to negative values. For $4\pi\eta/s = 0.5$, when equilibration is achieved before the onset of transverse expansion, the scaled hydro curve merges into the RTA one as implied by the discussion in Sec. IV D. At small opacity ($4\pi\eta/s = 10$), the merging process is interrupted by transverse expansion. The scaled hydro result for ε_p is in perfect agreement with kinetic theory at large opacities and stays in good agreement at intermediate opacities. Due to a smaller overall interaction rate, the ε_p response decreases with decreasing opacity. For small opacities, a negative trend in the early time behavior of hydrodynamics causes discrepancies with kinetic theory. This trend will become dominant at even smaller opacities, resulting in negative values of the late time plateaus.

As discussed in Sec. IV C, at early times, $\langle u_\perp \rangle_\epsilon$ builds up linearly with the elapsed time $\Delta\tau = \tau - \tau_0$ in kinetic theory. For finite initialization time τ_0, the detailed behavior in hydrodynamics is slightly different, but almost indistinguishable from linearity in $\Delta\tau$. Hence, we plot the ratio $\frac{\langle u_\perp \rangle_\epsilon}{\Delta\tau/R}$ and indicate the early time limit using horizontal dashed blue lines. The plots confirm that there are slight differences in the early time behavior of the flow velocities in hydrodynamics and kinetic theory; however they come into agreement on similar timescales as $dE_{\mathrm{tr}}/d\eta$. This is partly owing to the fact that early time contributions to the total $\langle u_\perp \rangle_\epsilon$ are negligible. $\langle u_\perp \rangle_\epsilon$ enters a period of superlinear rise during transverse expansion. While this period ends earlier at larger opacities due to dilution of the system and transition to free streaming, the total rise of $\frac{\langle u_\perp \rangle_\epsilon}{\Delta\tau/R}$ is nevertheless larger. Comparing hydrodynamic results to kinetic theory results, the late time free-streaming does not seem to be accurately reproduced, as hydrodynamics

[3]In general, the equilibration timescale scales with $(\eta/s)^{3(1-\gamma/4)/2}$, with γ as defined in Eq. (50). Numerically, the exponent 1.30 for viscous hydrodynamics is close to the one for RTA.

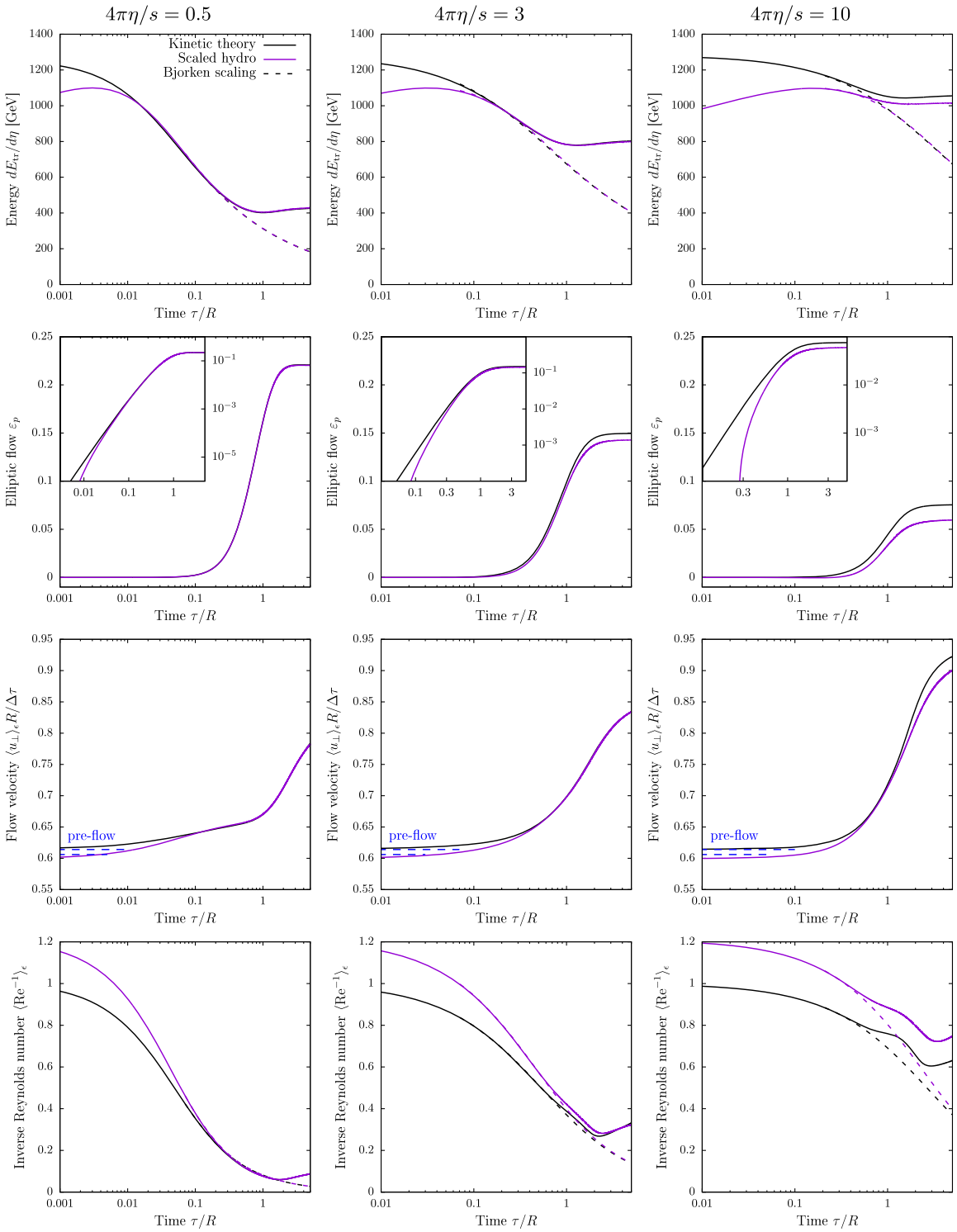

FIG. 8. Time evolution of (from top to bottom) transverse energy $dE_{\rm tr}/d\eta$ [cf. Eq. (13)], elliptic flow ε_p [cf. Eq. (14)], transverse flow velocity $\langle u_\perp \rangle_\epsilon$ [cf. Eq. (15)] and inverse Reynolds number $\langle {\rm Re}^{-1} \rangle_\epsilon$ [cf. Eq. (16)] in kinetic theory (black) and scaled viscous hydrodynamics (purple). The time axis is scaled logarithmically in all plots. The plots showing elliptic flow ε_p feature an inset plot of the same quantity plotted in log-log scale. The plots of flow velocity also show the preflow result from Table II for the early time limit for $\langle u_\perp \rangle_\epsilon/(\Delta\tau/R)$ (0.614 for kinetic theory and 0.606 for scaled hydrodynamics). Bjorken scaling results are shown with dashed lines for $dE_{\rm tr}/d\eta$ (top) and $\langle {\rm Re}^{-1} \rangle_\epsilon$ (bottom).

underestimates $\langle u_\perp \rangle_\epsilon$. Problems in the late time behavior are less relevant for the other observables we discuss, as they tend to plateau at late times. This late time discrepancy between hydrodynamics and kinetic theory is thus a phenomenon that mainly affects $\langle u_\perp \rangle_\epsilon$ among the observables that were tracked in this work, and is not related to preequilibrium.

Finally, we look at the time evolution of the average inverse Reynolds number, which is a measure of the size of nonequilibrium effects in the system. We normalized this in such a way that, in RTA, its initial value is equal to one (note that on the hydro attractor, $\mathrm{Re}^{-1} \sim 1.212$ when $\tau_0 \to 0$). Like for $\mathrm{d}E_{\mathrm{tr}}/\mathrm{d}\eta$, the two model descriptions will come into agreement in the late time limit of Bjorken flow scaling, on timescales that are larger for smaller opacities. Due to equilibration, in this period $\langle \mathrm{Re}^{-1} \rangle_\epsilon$ experiences a phase of rapid decay towards 0, as expected since Re^{-1} measures nonequilibrium effects. The effect of transverse expansion on this observable is not straightforwardly understood, except for the fact that due to the additional dilution, $\langle \mathrm{Re}^{-1} \rangle_\epsilon$ must be larger in full simulations than in Bjorken flow scaling. For large opacities, transverse expansion seems to only slow down the approach to equilibrium. However, at intermediate opacities we see a significant rise in $\langle \mathrm{Re}^{-1} \rangle_\epsilon$. We also computed results for the limit of vanishing opacity. Here, the inverse Reynolds number remains constant at early times, but later increases due to transverse expansion, e.g. at $\tau = 4R$ to a value of $\langle \mathrm{Re}^{-1} \rangle_\epsilon(\tau = 4R) = 1.322$. However, an increase due to transverse expansion cannot be the only late time effect, as we can see from the results at $4\pi\eta/s = 10$, where the trend of this quantity changes multiple times. It first departs from the local Bjorken flow prediction at $\tau/R \sim 0.3$, but later the curve returns to decreasing at a rate comparable to that during the Bjorken flow stage. At late times, the behavior transitions to a rise in the inverse Reynolds number. Despite this peculiar behavior, our numerical results indicate that $\langle \mathrm{Re}^{-1} \rangle_\epsilon$ reaches a minimum value that is larger for smaller opacities. For very small opacities, it will not drop significantly below its initial value of 1 before starting to rise.

For a more detailed examination of the opacity dependence of the time evolution in kinetic theory ranging from very small ($4\pi\eta/s = 1000$) to very large opacities ($4\pi\eta/s = 0.01$), please see Appendix C.

After examining the time evolution of these observables and establishing some understanding about the implications of their buildup, we now want to invert this logic. As the change in these observables carries information on the state of the system, e.g. the progress of its equilibration or the onset of transverse expansion, we want to track the first times when these observables reach a specific milestone of their time evolution as a function of opacity. Figure 9 shows plots of kinetic theory results for these curves for five different milestone criteria. Specifically, we tracked when the average

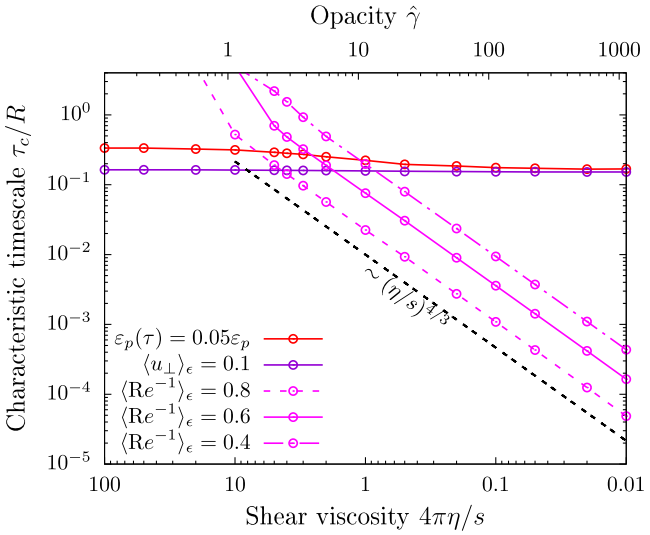

FIG. 9. Opacity ($\hat{\gamma} = \frac{11.3}{4\pi\eta/s}$) dependence of the characteristic times where the elliptic flow ε_p [cf. Eq. (14)] reaches 5% of its late time ($\tau = 4R$) value (red), the transverse flow velocity [cf. Eq. (15)] builds up to a value of $\langle u_\perp \rangle_\epsilon = 0.1$ (purple), or the inverse Reynolds number [cf. Eq. (16)] drops to a value of $\langle \mathrm{Re}^{-1} \rangle_\epsilon = 0.8$ (pink, dashed), 0.6 (pink, solid) or 0.4 (pink, long-short dashed). The buildup in transverse flow velocity marks the transition from the Bjorken flow scaling regime to the regime of transverse expansion, while the drop in inverse Reynolds number marks the region where hydrodynamics is applicable.

transverse flow velocity reaches a value of 0.1 as a criterion for the onset of transverse expansion, the time when the elliptic flow response builds up to 5% of its maximum value at the given opacity as a criterion for the beginning of the buildup of flow, and the time when the average inverse Reynolds number reaches values of 0.4, 0.6 and 0.8, which tells us to what degree hydrodynamization has progressed. As it turns out, the curve for the flow velocity criterion is almost perfectly flat at a value of $\tau_c \approx 0.15R$, meaning that the early time buildup of $\langle u_\perp \rangle_\epsilon$ is mostly independent of the opacity. The elliptic flow criterion is met at similar times as the flow velocity criterion at large opacities, but at slightly later times $\tau_c \approx 0.3R$ for small opacities. Despite the general time frame of ε_p-buildup being independent of opacity, it seems to start slightly earlier at larger opacities. The most interesting criterion curves are those for the average inverse Reynolds number. The system's adherence to early time Bjorken flow scaling leads to a power law behavior $\tau_c \propto (\eta/s)^{4/3}$ for all three of these curves at large opacities. The curves deviate from this power law when the criterion is not reached before transverse expansion sets in at times $\tau \sim R$. For small opacities, the criteria are never met, as the average inverse Reynolds number reaches a minimum value larger than the criterion value, as already stated in the discussion of Fig. 8. The behavior of $\mathrm{d}E_{\mathrm{tr}}/\mathrm{d}\eta$ resembles that of $\mathrm{d}E_\perp/\mathrm{d}\eta$, which we already

discussed in our previous paper [71]. Similarly to $\langle \mathrm{Re}^{-1} \rangle_\epsilon$, it follows Bjorken flow scaling at early times, resulting in a similar power law behavior.

C. Time evolution in hybrid schemes

Another way to alleviate discrepancies due to the behavior of hydrodynamics in the preequilibrium phase as discussed in Sec. IV B is to model the time evolution via a hybrid scheme, switching from a kinetic theory based description at early times to hydrodynamics at later times, i.e. initializing the hydrodynamic simulation with the energy-momentum tensor computed from the kinetic theory based time evolution. This requires to fix a criterion for when to switch descriptions.

As we argue that hydrodynamics becomes viable only after some timescale related to equilibration, we also expect the accuracy of hybrid scheme results to depend on the switching times. Due to the opacity dependence of equilibration, it might be beneficial to choose switching times as a function of opacity. Hence we tested both a hybrid scheme with fixed switching times at two different times $\tau = 0.4$ fm and $\tau = 1$ fm, which are in the range of switching times typically used in phenomenological descriptions, and with dynamically determined switching times.

In order to tie this definition to the phenomenon of equilibration, we determine the dynamical switching times on the basis of the decrease of the average inverse Reynolds number $\langle \mathrm{Re}^{-1} \rangle_\epsilon$; i.e. we switch as soon as this quantity first reaches a specific value. Specifically, we chose the values $\langle \mathrm{Re}^{-1} \rangle_\epsilon = 0.8$, 0.6 and 0.4 (sometimes we will consider switching also when $\langle \mathrm{Re}^{-1} \rangle_\epsilon$ drops below 0.2). In the case of a transversally homogeneous system, Fig. 3 shows that these values for the inverse Reynolds number correspond to various degrees of hydrodynamization of the system. Specifically, $\mathrm{Re}^{-1} = 0.8$ ($\tilde{w} \simeq 0.2$) corresponds to the onset of hydrodynamization. When $\mathrm{Re}^{-1} = 0.6$ ($\tilde{w} \simeq 0.6$), the system significantly progressed through the hydrodynamization process, while when $\mathrm{Re}^{-1} = 0.4$ ($\tilde{w} \simeq 1$), the system has hydrodynamized and the kinetic theory and hydrodynamics attractor curves are almost merged. Due to the relation (38) between $\tilde{w}$ and the Bjorken time τ, the characteristic times τ_c when Re^{-1} drops below a certain threshold increase with $4\pi\eta/s$ (see Sec. V B for a detailed discussion).

The results are illustrated by the time evolution of transverse energy $\mathrm{d}E_{\mathrm{tr}}/\mathrm{d}\eta$, elliptic flow ε_p and average transverse flow velocity $\langle u_\perp \rangle_\epsilon$ compared for different choices of the switching times, as plotted in Fig. 10 at three different opacities. The early time evolution was computed with the RLB method of simulating kinetic theory. The plots also compare to results from a pure kinetic theory simulation as well as from our scaled viscous hydro scheme. Here we plot all results including the ones for elliptic flow ε_p on a logarithmic scale of the time axis so that the different switching times are discernible. The ε_p plots also feature an inset plot on log-log scale. It can be seen that the curves corresponding to the hybrid setups tend to detach from the RTA curve towards lower values of ε_p. Since in viscous hydro, the equilibration process leads to a decrease of spatial eccentricity ϵ_2 (see lower panel of Fig. 5), the hybrid simulations with early switching times will lead to lower late-time values of ε_p (see the discussion in the next section).

At a small shear viscosity of $4\pi\eta/s = 0.5$, all switching schemes yield accurate results for all three observables. Since the equilibration timescale is small for this opacity, the system has equilibrated by the time we switch descriptions such that kinetic theory and hydrodynamics are in agreement. The $\langle \mathrm{Re}^{-1} \rangle_\epsilon$-based criteria are fulfilled early on in the system's evolution such that the dynamically chosen switching times are significantly smaller than the fixed ones. However, when comparing results from pure kinetic theory or viscous hydrodynamics, they are within the time frame where both descriptions are in acceptable agreement. The only curve where a deviation from kinetic theory is clearly visible is the one for $\mathrm{Re}^{-1} = 0.8$, where hydrodynamization has only partly progressed by the time this criterion is fulfilled.

The results at $4\pi\eta/s = 3$ now show that it is indeed necessary to give the choice of switching times some thought, as here we see a significant increase in accuracy of results for $\mathrm{d}E_{\mathrm{tr}}/\mathrm{d}\eta$ and $\langle u_\perp \rangle_\epsilon$ with later switching times. For this opacity, the dynamically chosen switching times are on a similar scale as the fixed ones. We also see that the nature of any discrepancies with pure kinetic theory results is the same as in the case of hydrodynamics. As soon as we switch, the curves of these observables follow a trajectory that is qualitatively similar to the pure hydrodynamics result, meaning that $\mathrm{d}E_{\mathrm{tr}}/\mathrm{d}\eta$ is increased, while $\langle u_\perp \rangle_\epsilon$ and ε_p are decreased relative to the kinetic theory result.

The strength of the dynamically chosen switching times is well displayed for results at $4\pi\eta/s = 10$. In this case, the system is still far from hydrodynamized at the two fixed switching times, leading to sizeable inaccuracies in the corresponding hybrid scheme results for all three observables, but especially for $\mathrm{d}E_{\mathrm{tr}}/\mathrm{d}\eta$. As $\langle \mathrm{Re}^{-1} \rangle_\epsilon$ does not drop low enough, two of the three criteria for the dynamical switching were not reached. However, the result for switching at the largest of the three values of $\langle \mathrm{Re}^{-1} \rangle_\epsilon$ retains a similar level of accuracy as at smaller shear viscosity and is a significant improvement to fixed time switching results.

Overall, we find that while switching at fixed time is conceptionally straightforward and always possible, the accuracy of this scheme strongly depends on the opacity and results at small opacity show large deviations from full kinetic theory. On the other hand, switching based on $\langle \mathrm{Re}^{-1} \rangle_\epsilon$ is not always possible because this quantity does not drop to the desired values at small opacities, but

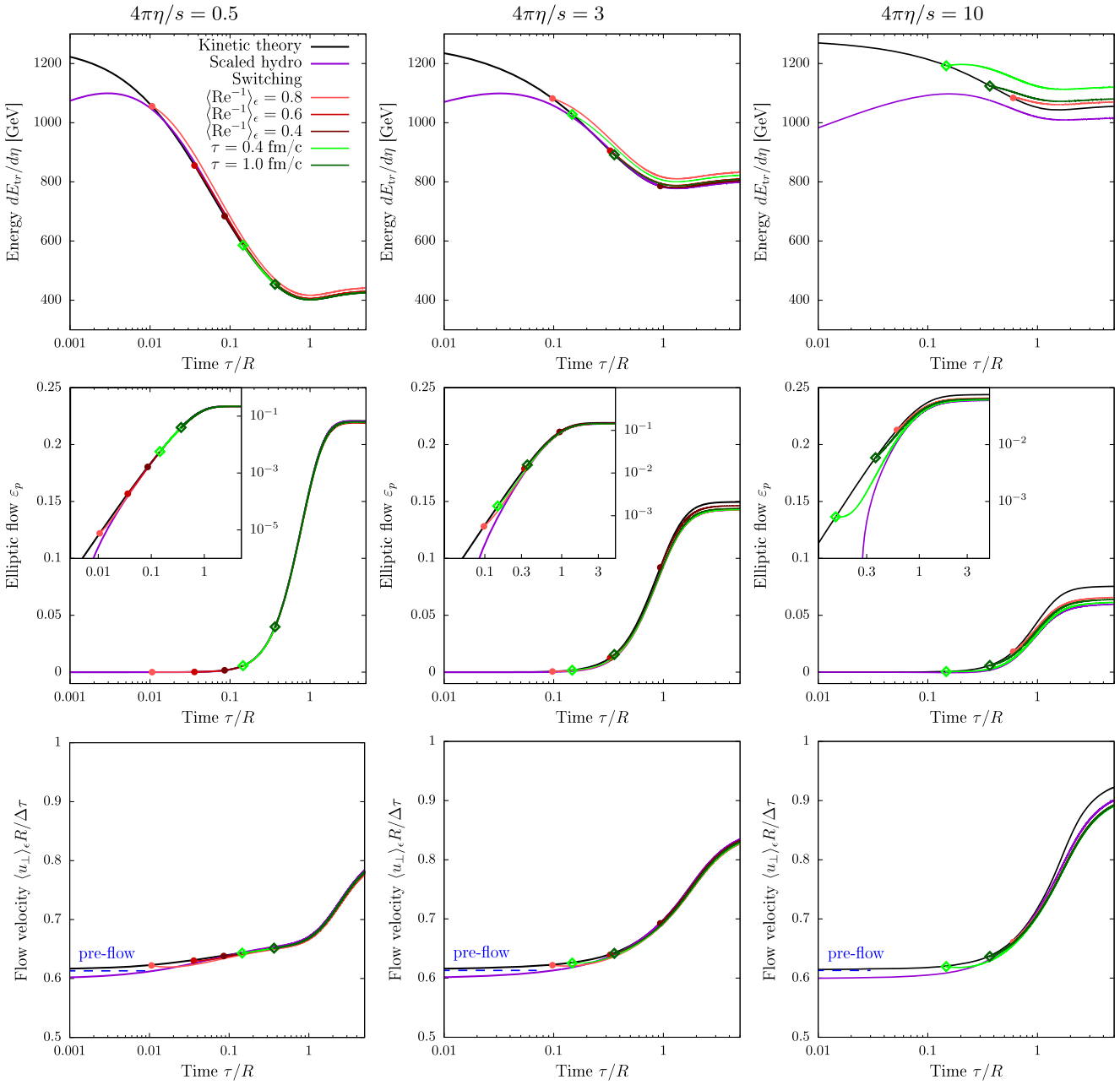

FIG. 10. Time evolution of transverse energy $\mathrm{d}E_{\mathrm{tr}}/\mathrm{d}\eta$ [top, cf. Eq. (13)], elliptic flow ε_p [middle, cf. Eq. (14)] and transverse flow velocity $\langle u_\perp\rangle_\epsilon$ [bottom, cf. Eq. (15)] in hybrid kinetic theory + viscous hydro simulations at opacities $4\pi\eta/s = 0.5$ (left), 3 (middle) and 10 (right) when switching at different values of the inverse Reynolds number [cf. Eq. (16)] $\langle \mathrm{Re}^{-1}\rangle_\epsilon = 0.8$ (light red), 0.6 (red) and 0.4 (dark red) or fixed time $\tau = 0.4$ fm (light green) and $\tau = 1$ fm (dark green). The switching points are marked with filled symbols. The time axis is scaled logarithmically. The plots showing elliptic flow ε_p feature an inset plot of the same quantity plotted in log-log scale. In the flow velocity plots, we also show the estimate $\langle u_\perp\rangle_{\epsilon,\mathrm{RTA}} = 0.614\Delta\tau/R$ for the early time buildup of preflow in kinetic theory (see Table II).

whenever it is possible, the accuracy of the result can be estimated beforehand and depends only little on opacity. In other words, the dynamical definition yields the earliest possible switching time for a desired accuracy, and whenever $\langle \mathrm{Re}^{-1}\rangle_\epsilon$ does not drop enough for it to be determined, hydrodynamics is not viable in the first place.

Finally, we also tested hybrid schemes with the same switching times but with an early time evolution computed in KøMPøST. We found that due to its limited range of applicability, some of the later switching times could not be viably reached with this description. But whenever we were able to obtain results, they were in good agreement with the results

from the previously discussed scheme, except for some systematic errors in ε_p and $\langle u_\perp \rangle_\epsilon$. These results are presented in more detail in Appendix D, together with analogous time dependence plots to those presented in Fig. 10.

VI. OPACITY DEPENDENCE OF FINAL STATE OBSERVABLES IN DIFFERENT TIME EVOLUTION MODELS

The previous section's comparison of the time evolution in different models has provided insights into the nature of different sources of discrepancies and at what opacities to expect them. For a detailed opacity-resolved analysis, it is convenient to study the dependence of final-state observables on a wide range of opacity, from the free-streaming regime to ideal fluid behavior. In Sec. VI A, we present opacity dependencies in kinetic theory, naive viscous hydrodynamics and scaled viscous hydrodynamics. Section VI B discusses results for hybrid simulation schemes.

A. Scaled and naive hydrodynamics compared to kinetic theory

First, we assess the performance of scaled hydrodynamics as described in Sec. IV D when compared to a common naive initialization scheme of hydrodynamics, where the simulation is started at a time τ_0 where hydrodynamization is likely to have set in, with the same initial condition for $\tau_0 \epsilon(\tau_0, \mathbf{x}_\perp)$ as we are using for kinetic theory simulations initialized in the early time free-streaming limit. Figure 11 shows the opacity dependences of transverse energy $\mathrm{d}E_{\mathrm{tr}}/\mathrm{d}\eta$, elliptic flow ε_p and average transverse flow velocity $\langle u_\perp \rangle_\epsilon$ in kinetic theory, scaled hydrodynamics and naive hydrodynamics initialized on the hydrodynamic attractor at two different times $\tau_0 = 0.4$ fm and $\tau_0 = 1$ fm, which are in the range of values typically used in phenomenological descriptions.

For all three observables, the kinetic theory results smoothly interpolate between limiting cases of small and large opacities. For $\mathrm{d}E_{\mathrm{tr}}/\mathrm{d}\eta$ and ε_p, we compare at small opacities to results from the linear order opacity expansion that is introduced in Sec. III B. Results from full kinetic theory are in excellent agreement with these approximations for $4\pi\eta/s \gtrsim 20$. In the case of $\langle u_\perp \rangle_\epsilon$, we present results for the free-streaming limit $\hat{\gamma} \to 0$, to which the full kinetic theory results converge at small opacities.

On the other end of the opacity spectrum, the results from both kinetic theory and scaled viscous hydrodynamics converge to those of scaled ideal hydrodynamics in the limit $\eta/s \to 0$. Even though $\eta/s = 0$ by definition in ideal hydrodynamics, we represent the scaled ideal hydro results as a function of $4\pi\eta/s$ in the equivalent RTA simulation [see discussion around Eq. (86)], leading to a power-law dependence $\mathrm{d}E_{\mathrm{tr}}/\mathrm{d}\eta \propto (4\pi\eta/s)^{4/9}$, which is confirmed by the scaled viscous hydrodynamics and

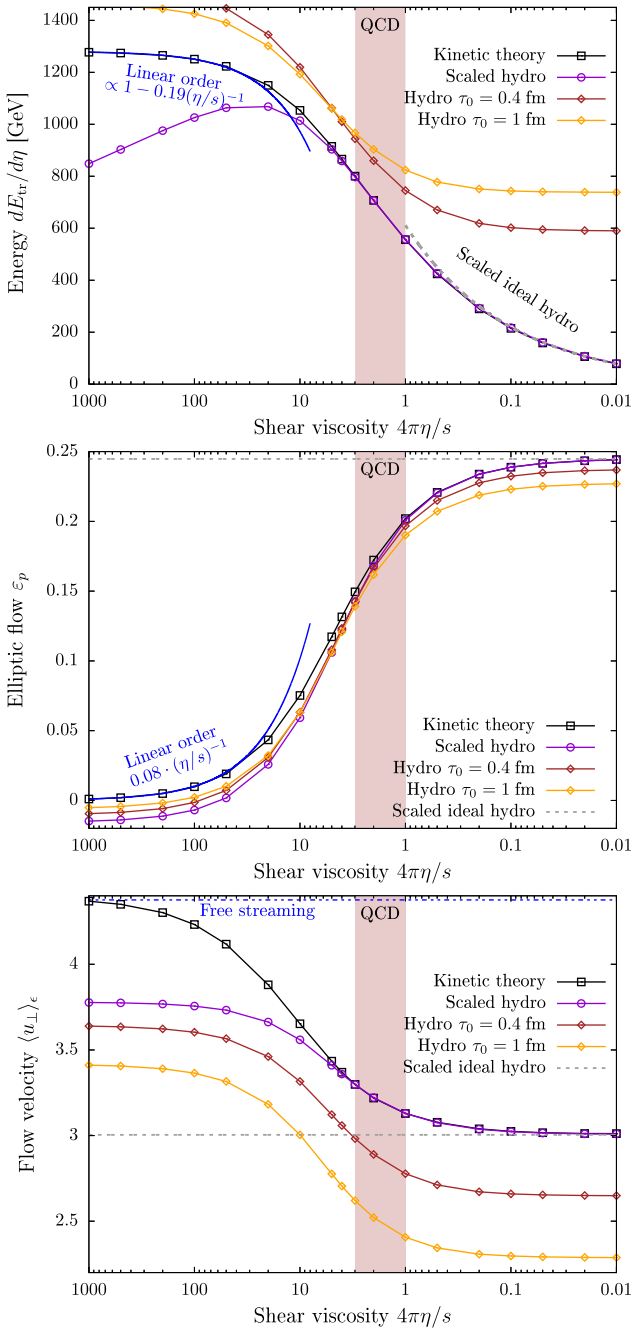

FIG. 11. Opacity (η/s) dependence of the final ($\tau = 4R$) values of transverse energy $\mathrm{d}E_{\mathrm{tr}}/\mathrm{d}\eta$ [top, cf. Eq. (13)], elliptic flow ε_p [middle, cf. Eq. (14)] and transverse flow velocity $\langle u_\perp \rangle_\epsilon$ [bottom, cf. Eq. (15)] for kinetic theory (black), scaled hydro (purple) and naive hydro at two different initialization times $\tau_0 = 0.4$ fm (brown) and 1 fm (yellow). Also plotted are the small opacity limits of an opacity-linearized result (blue) in the top two plots, the free-streaming result (blue, dashed) in the bottom plot as well as the opacity-scaled ideal hydrodynamics results (gray, dashed). The latter follows a $(\eta/s)^{4/9}$ scaling law for $\mathrm{d}E_{\mathrm{tr}}/d\eta$ as per the initialization scheme in Eq. (86). The ideal hydro results are $611\mathrm{GeV} \cdot (4\pi\eta/s)^{4/9}$ for $\mathrm{d}E_{\mathrm{tr}}/d\eta$, 0.244 for ε_p and 3.01 for $\langle u_\perp \rangle_\epsilon$. The red shaded region shows the realistic values for QCD according to Bayesian estimates.

kinetic theory results (this result was derived from early time Bjorken scaling in [71]). The curves for ε_p and $\langle u_\perp \rangle_\epsilon$ converge at large opacities to the ideal hydrodynamics limit that was obtained with a scaled initial condition. This is not *a priori* obvious but rather an achievement of our proposed scheme. Ideal hydrodynamics is the large opacity limit of kinetic theory only after hydrodynamization. At any finite opacity, kinetic theory simulations feature a preequilibrium period which is absent in ideal hydro. In this period, the ellipticity ϵ_2 decreases in kinetic theory, such that, with the same initial condition, it would result in a smaller elliptic flow ε_p than in ideal hydro. The agreement is only reached after scaling the hydro initial condition as discussed in Sec. IV D.

Comparing now to hydrodynamic results, for all three obserables, the large opacity limits of scaled hydrodynamics and kinetic theory are in excellent agreement. Going to small opacities, all observables are underestimated in hydro, as will be further discussed in the following. Agreement holds for $4\pi\eta/s \lesssim 3$.

On the other hand, for naive hydrodynamics initialized at $\tau_0 = 0.4$ and 1.0 fm, the opacity dependence curves show qualitatively similar behavior to kinetic theory but remain in quantitative disagreement for all opacities. This is obvious in the case of $\mathrm{d}E_{\mathrm{tr}}/\mathrm{d}\eta$, which is significantly overestimated. We find that the large opacity power law is not captured. There are different reasons for this in the two limiting cases of large and small opacity. For small opacities $4\pi\eta/s \gtrsim 10$, despite the initialization time being large, it is still smaller than the equilibration timescale and the simulation will partly undergo a preequilibrium phase. As we have seen, in the hydrodynamic description of this phase $\mathrm{d}E_{\mathrm{tr}}/\mathrm{d}\eta$ increases before the onset of transverse expansion, while staying constant in kinetic theory, so it is overestimated in hydro. For the smaller initialization time $\tau_0 = 0.4$ fm, the system is in preequilibrium for a longer time compared to $\tau_0 = 1$ fm. This is why results for $\tau_0 = 0.4$ fm yield a larger final value of $\mathrm{d}E_{\mathrm{tr}}/\mathrm{d}\eta$ at small opacities. On the other hand, for large opacities $4\pi\eta/s \lesssim 3$, the system would have been in equilibrium for a significant amount of time if it had been initialized at an earlier time. In the equilibrated phase before transverse expansion, $\mathrm{d}E_{\mathrm{tr}}/\mathrm{d}\eta$ drops proportionally to $\tau^{-1/3}$. The larger the initialization time, the more of this period is cut out of the simulation, resulting in a larger final value. This is why the curve for initialization at $\tau_0 = 1$ fm is above the one for $\tau_0 = 0.4$ fm at large opacities, resulting in a crossing of the two at intermediate opacities $4\pi\eta/s \sim 5$. The equilibration timescale becomes smaller and smaller at larger and larger opacities, meaning that for fixed initialization time more and more of the $\tau^{-1/3}$-scaling period is cut out. This is why the large opacity power law is not reproduced in naive hydrodynamics.

These problems are cured in scaled hydrodynamics. It is initialized at very early times, so no part of the time evolution is lost. The discrepancies due to hydrodynamic preequilibrium behavior are cured via scaling the initial energy density as discussed in Sec. IV D such that agreement with kinetic theory is reached only after equilibration. However, for small opacities $4\pi\eta/s \gtrsim 3$, the underlying assumption of a timescale separation of equilibration and transverse expansion no longer holds. In this case, scaled hydrodynamics underestimates $\mathrm{d}E_{\mathrm{tr}}/\mathrm{d}\eta$, as transverse expansion interrupts its approach to kinetic theory behavior before agreement is reached.

Of the three presented observables, ε_p in naive hydrodynamics shows the weakest deviations from kinetic theory. This is in alignment with our expectations, as we know that hydro has been very successful in phenomenological descriptions of anisotropic flow. The reasons might be that ε_p builds up on timescales that are fully captured by simulations at initialization times of $\sim$1 fm and depends very little on the overall energy scale. But certainly, this level of agreement was not to be expected *a priori* and should be regarded as a coincidence. The influence of the initialization time is as follows. At small opacities $4\pi\eta/s \gtrsim 10$, a part of the early time negative trend in hydrodynamics is cut out, resulting in larger results for later initialization times. For large opacities $4\pi\eta/s \lesssim 1$, ε_p already has positive contributions at early times which might be cut out, resulting in smaller final values for later initialization times. But very early initialization times cannot bring hydro into agreement with kinetic theory. As discussed in Sec. IV B, hydrodynamics initialized at very early times exhibits a larger decrease of the eccentricity during preequilibrium, resulting in lower final values of ε_p than in kinetic theory. However, the scaling procedure counteracts this phenomenon by increasing the eccentricity in the initial state of hydrodynamic simulations, such that scaled hydrodynamics is in perfect agreement with kinetic theory at large opacities $4\pi\eta/s \lesssim 3$. For small opacities $4\pi\eta/s \gtrsim 10$, on the other hand, due to the early initialization scaled hydrodynamics features a longer period of the aforementioned early time negative buildup of ε_p, resulting in final values which are lower than in the case of the naive hydro initializations discussed above.

The flow velocity results from naive hydrodynamics again show two effects. One of them is straightforward: as this observable rises monotonically with time, for larger initialization times, there is less time for $\langle u_\perp \rangle_\epsilon$ to build up, resulting in an underestimate. This effect is cured in scaled hydrodynamics due to the early initialization. At small opacities $4\pi\eta/s \gtrsim 10$, we see an additional decrease of hydrodynamic results compared to kinetic theory due to its inability to describe the late-time free-streaming behavior. This is an effect that both

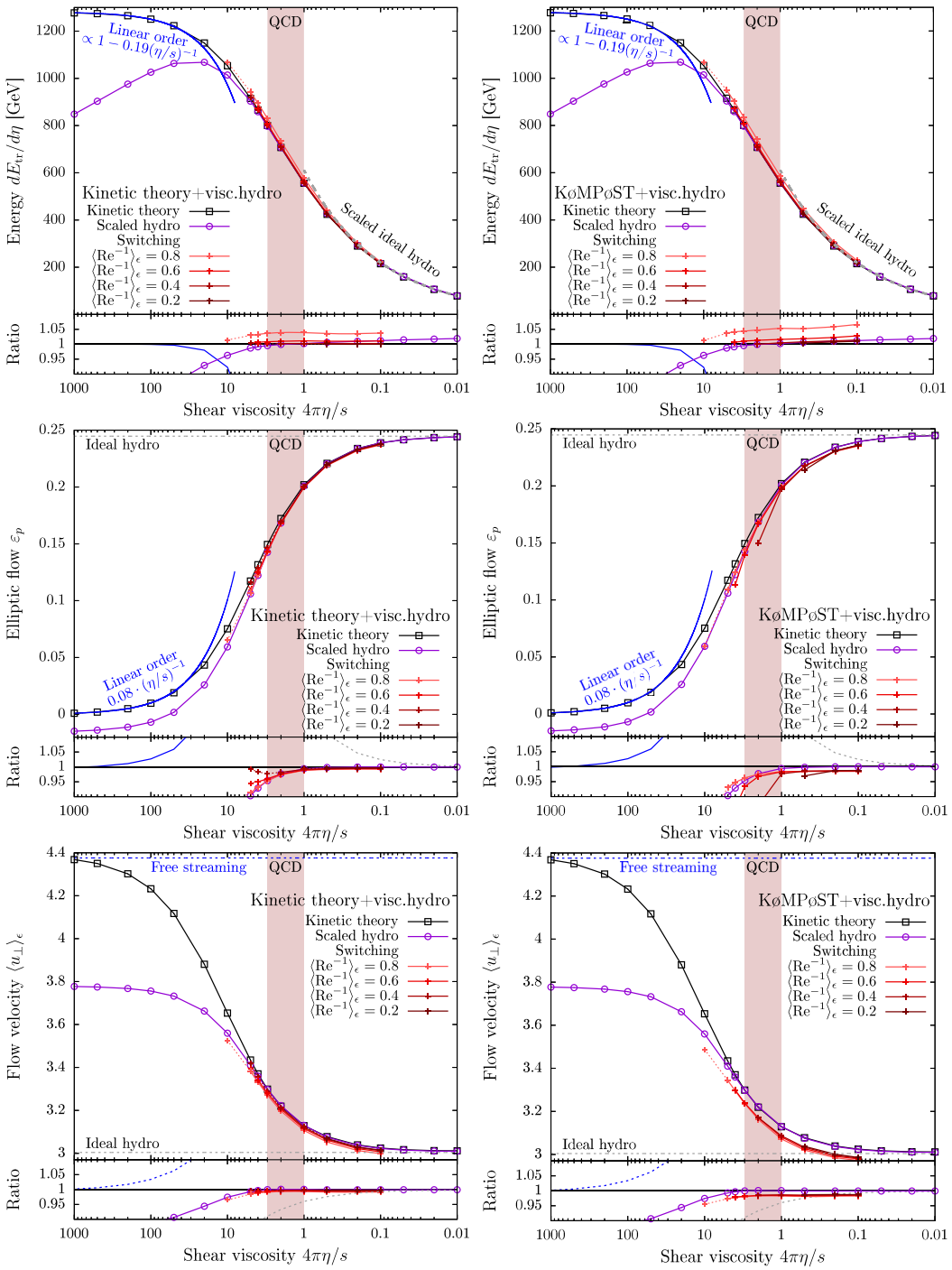

FIG. 12. Opacity (η/s) dependence of the final ($\tau = 4R$) values of transverse energy $\mathrm{d}E_{\rm tr}/\mathrm{d}\eta$ [top, cf. Eq. (13)], elliptic flow ε_p [middle, cf. Eq. (14)] and transverse flow velocity $\langle u_\perp \rangle_\epsilon$ [bottom, cf. Eq. (15)] in hybrid kinetic theory + viscous hydro (left) and KøMPøST + viscous hydro simulations (right) when switching at different values of the inverse Reynolds number [cf. Eq. (16)] $\langle \mathrm{Re}^{-1}\rangle_\epsilon = 0.8$, 0.6, 0.4 and 0.2 plotted in different shades of red from light to dark. Results from simulations with switching times after $\tau = 0.5R$ are plotted with smaller points (+) and dashed lines. The results are compared to kinetic theory (black), scaled hydro (purple) and the small opacity limits of an opacity-linearized result (blue) in the top two plots, the free-streaming result (blue, dashed) in the bottom plot as well as the large opacity limit of scaled ideal hydro (gray, dashed), which scales as $(\eta/s)^{4/9}$ in the top plot. The red shaded region shows the realistic values for QCD according to Bayesian estimates. The bottom part of each plot shows the ratios of all results to those from kinetic theory.

hydro schemes (based on naive and scaled initial conditions) have in common.

B. Hybrid simulations

As described in Sec. V C, another way to bring hydrodynamic results into agreement with kinetic theory is to use hybrid schemes switching from a kinetic theory based early time description to hydrodynamics at later times. We tried switching both at fixed times as well as at the first times equilibration has proceeded to a given extent, which we quantified by the inverse Reynolds number dropping to a specific value. We also tested two different model descriptions for early times: full kinetic theory and KøMPøST. As described in the previous section, the time evolution curves of all observables instantaneously change behavior when the models are switched, such that switching too early will be affected by the inaccurate description of preequilibrium in hydrodynamics. We now want to quantitatively assess the accuracy of various switching schemes as a function of opacity.

We first discuss results for the opacity dependence in hybrid simulations with $\langle \mathrm{Re}^{-1}\rangle_\epsilon$-based switching, which are plotted in Fig. 12. For early switching times on the timescale of equilibration, hybrid results may reflect the inaccurate preequilibrium behavior in hydrodynamics. Of course, in this case, there is no scaling of the initial condition to counteract this behavior. However, this also means that these schemes do not suffer from discrepancies due to an incomplete approach of a scaled initial condition to kinetic theory behavior before the onset of transverse expansion, and therefore tend to be more accurate than scaled hydrodynamics at intermediate opacities, i.e. for $4\pi\eta/s \sim 3$. However, results plotted with smaller crosses and dashed lines were obtained in simulations with switching times larger than $0.5R$, so in this case it is questionable whether these schemes could be considered hybrid results, as the crucial parts of the time evolution were actually described in kinetic theory.

Going into more detail, hybrid results typically overestimate $\mathrm{d}E_{\mathrm{tr}}/\mathrm{d}\eta$ because of the hydrodynamic preequilibrium increase after switching. ε_p is underestimated, however, the hydrodynamic negative early time trend is alleviated, such that results from kinetic theory + viscous hydro are typically larger than scaled hydro results. Hybrid results show a consistent underestimation of $\langle u_\perp\rangle_\epsilon$, but on a relative scale this error is negligible. This could be due to hydrodynamic flow velocities typically being smaller than those in kinetic theory at early times, causing a dip in $\langle u_\perp\rangle_\epsilon$ relative to kinetic theory after switching.

Comparing kinetic theory + viscous hydrodynamics in the left column of the figure to KøMPøST + viscous hydrodynamics in the right column, one obvious difference is that, in the latter, some of the results for smaller opacities are missing, because there the $\langle \mathrm{Re}^{-1}\rangle_\epsilon$-based switching times were too late to be reached with KøMPøST.[4] Where it does work, it produces almost the same results for $\mathrm{d}E_{\mathrm{tr}}/\mathrm{d}\eta$ as kinetic theory. The underestimation of $\langle u_\perp\rangle_\epsilon$ is slightly more severe in KøMPøST. It does seem to have a systematic component on top of the one related to switching early. But the total deviation is still negligible. The largest difference is seen in ε_p, which is not built up at all in KøMPøST simulations, thus there is a significantly larger underestimation at smaller opacities, where a larger part of the time evolution is described in KøMPøST.

Next, we shift our attention to results from hybrid schemes at fixed switching times $\tau_s = 0.4$ fm and $\tau_s = 1$ fm, which are presented in Fig. 13. As expected from the discussion of the time evolution in Sec. V C, again kinetic theory + viscous hydrodynamics yields perfectly accurate results at large opacities $4\pi\eta/s \lesssim 1$ and improves on scaled hydrodynamics at intermediate opacities $4\pi\eta/s \sim 3$, but less so than for dynamically chosen switching times. The upshot is that hybrid schemes with fixed switching times are applicable for arbitrarily small opacities. However, here the results for the three tracked observables show similar problems to those obtained in naive hydrodynamics simulations discussed earlier in this section. Due to incomplete equilibration at early switching times, $\mathrm{d}E_{\mathrm{tr}}/\mathrm{d}\eta$ increases after switching. ε_p suffers from the early time negative trend in hydrodynamics but slightly less than scaled hydrodynamics. $\langle u_\perp\rangle_\epsilon$ is again only slightly underestimated in hybrid schemes when compared to scaled hydrodynamics due to the different preequilibrium. This is an improvement over naive hydrodynamics, as instead of starting at late times with no flow velocity, the early time buildup is described in kinetic theory. Both schemes suffer equally from the inability of hydrodynamics to describe flow velocities in the late time free-streaming limit.

Also for fixed switching times, KøMPøST + viscous hydrodynamics results for $\mathrm{d}E_{\mathrm{tr}}/\mathrm{d}\eta$ and $\langle u_\perp\rangle_\epsilon$ are in good agreement with those obtained in kinetic theory + viscous hydrodynamics simulations. We again see the effect of the absence of ε_p buildup in KøMPøST. Since we do not increase the duration of time evolution in KøMPøST, the effect is not larger at small opacities $4\pi\eta/s \gtrsim 10$. In fact, here we see agreement with results from kinetic theory + viscous hydrodynamics, as there is no significant buildup of ε_p at early times. However, at large opacities $4\pi\eta/s \lesssim 5$, this buildup starts earlier, which is why KøMPøST + viscous hydrodynamics results underestimate the final values in these cases.

[4]For large evolution times, KøMPøST crashes in the setup stage when computing the Green's functions. This is because they are only implemented for a finite number of points in momentum space and have to be convolved with a Gaussian smearing kernel $\exp(-\sigma^2|\mathbf{k}|/2)$. But the Green's functions scale in $|\mathbf{k}|(\tau-\tau_0)$ such that for too large of an evolution time this smearing is no longer sufficient.

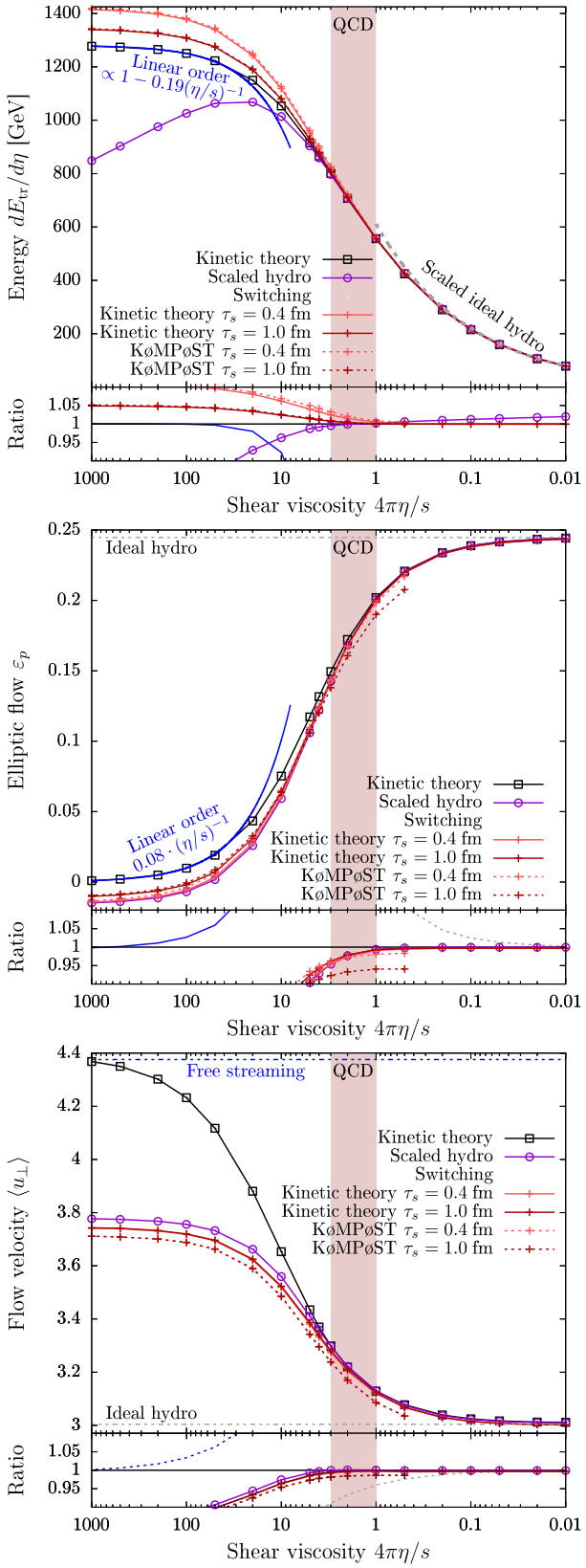

FIG. 13. (*Continued*).

VII. CONCLUSIONS

In this work, we examined hydrodynamic and kinetic theory simulations of hadronic collisions. Within a simplified model setup based on RTA and using a fixed initial profile that was obtained as an average of events in the 30–40% centrality class of Pb-Pb collisions, we scanned the dynamical behavior on the whole range in interaction rates as parametrized by the opacity $\hat{\gamma}$ defined in Eq. (7), which for our fixed profile is inversely proportional to shear viscosity, $\hat{\gamma} = 11.3/(4\pi\eta/s)$. This study was based on results for the transverse energy $dE_{\rm tr}/d\eta$, elliptic flow ε_p, radial flow $\langle u_\perp \rangle_\epsilon$ and shear stress as measured via the inverse Reynolds number $\langle {\rm Re}^{-1} \rangle_\epsilon$. At small opacities $4\pi\eta/s \gtrsim 20$, kinetic theory agrees with results from a linearization in opacity. Here, the system is too dilute for hydrodynamics to be applicable, which was confirmed quantitatively in Sec. VI A: the time evolution of transverse energy, radial flow and shear stress is in significant disagreement in hydrodynamic simulations compared to kinetic theory. For large opacities $4\pi\eta/s \lesssim 0.1$, in the limit of high interaction rates, kinetic theory is expected to converge to hydrodynamics. Our results confirm that the two descriptions are in agreement after preequilibrium. Going down to intermediate opacities, we found that for suitable setups of hydrodynamics, results for final state transverse energy, elliptic flow and radial flow are in good agreement with kinetic theory up to shear viscosities $4\pi\eta/s \lesssim 3$ for the examined profile, which translates to opacity values $\hat{\gamma} \gtrsim 4$.

However, hydrodynamics is not suitable for describing out-of-equilibrium behavior in the early preequilibrium stage and the late time period where the microscopic description of kinetic theory approaches a free-streaming behavior. In both of these regimes, hydrodynamic results are in quantitative disagreement with kinetic theory, which

FIG. 13. Opacity (η/s) dependence of the final ($\tau = 4R$) values of transverse energy $dE_{\rm tr}/d\eta$ [top, cf. Eq. (13)], elliptic flow ε_p [middle, cf. Eq. (14)] and transverse flow velocity $\langle u_\perp \rangle$ [bottom, cf. Eq. (15)] in hybrid kinetic theory + viscous hydro (solid lines) and KøMPøST + viscous hydro simulations (dashed lines) when switching at fixed times $\tau = 0.4$ fm (light red) and $\tau = 1$ fm (dark red). The results are compared to kinetic theory (black), scaled hydro (purple) and the small opacity limits of an opacity-linearized result (blue) in the top two plots, the free-streaming result (blue, dashed) in the bottom plot, as well as to the large opacity limit of scaled ideal hydro (gray, dashed), which scales as $(\eta/s)^{4/9}$ in the top plot. The red shaded region shows the realistic values for QCD according to Bayesian estimates. The bottom part of the plot shows the ratios of all results to those from kinetic theory.

can be seen at the level of final state observables, as discussed in Sec. IV B. Omitting the preequilibrium period or naively employing hydrodynamics to describe it will yield inaccurate results. On the other hand, at late times where interactions die out, these observables no longer build up and approach constant values, such that hydrodynamic descriptions yield similar results to kinetic theory. However, the late time free-streaming stage does have an effect on radial flow, which is underestimated in hydrodynamics.

We examined two different modified setups of hydrodynamic simulations that can alleviate problems with the preequilibrium evolution. The first setup follows the idea of an early initialization of hydrodynamics with a scaled initial condition relative to kinetic theory to counteract the differences in the preequilibrium evolution. These differences are predicted locally based on insights from Bjorken flow, which is accurate in systems with a timescale separation of equilibration and the onset of transverse flow. By construction, this setup yields accurate results at large opacities $4\pi\eta/s \lesssim 3$, but fails at smaller opacities, where equilibration takes longer and is interrupted by transverse expansion. The results obtained in this setup are presented in Secs. V B and VI A.

The second setup is a hybrid simulation switching from kinetic theory based descriptions at early times to hydrodynamics for later times. In these schemes, as described in Sec. V C, we saw an immediate change of the time evolution behavior at the moment that we switch the dynamical descriptions. Thus, the accuracy of hybrid simulations depends on the extent to which the kinetic theory and hydrodynamic descriptions of the system's time evolution have come into agreement by the time of the switch. This approach to agreement between the two descriptions is what we call hydrodynamization. We found that this criterion can in practice be quantified via the inverse Reynolds number. Figure 3 shows that the system is partly hydrodynamized when $\mathrm{Re}^{-1} = 0.8$, significantly hydrodynamized when $\mathrm{Re}^{-1} = 0.6$ and has reached almost perfect agreement of the two descriptions at $\mathrm{Re}^{-1} = 0.4$. The accuracy of hybrid simulations when switching at a fixed value of $\langle \mathrm{Re}^{-1} \rangle_\epsilon$ can be estimated beforehand and is almost independent of the opacity. As detailed in Sec. VI B, results from simulations with late switching times are accurate at high opacities $4\pi\eta/s \lesssim 1$ and can slightly improve on our first setup at intermediate opacities $4\pi\eta/s \sim 3$. At small opacities $4\pi\eta/s \gtrsim 20$, $\langle \mathrm{Re}^{-1} \rangle_\epsilon$ does not drop below 0.8, meaning the system does not equilibrate enough for hydrodynamics to become applicable at any point during the system's evolution.

For the early time kinetic theory description in hybrid models, we used both full kinetic theory and the compact KøMPøST code. The latter uses a linearization scheme in perturbations around local homogeneity to propagate the energy-momentum tensor according to the Boltzmann equation under the relaxation time approximation (the original version [109,110] is based on the QCD effective kinetic theory [106]). We first tested the performance of KøMPøST as detailed in Sec. III E and found that it can accurately reproduce full kinetic theory results for transverse energy, radial flow and isotropic shear stress, but due to the linearization it significantly underestimates elliptic flow. It is by construction limited to times on the order of $0.5R$. In hybrid simulations with switching times in this regime, transverse energy and radial flow results reach similar accuracy as when employing full kinetic theory. However, the underestimation of elliptic flow causes discrepancies when the switching time is non-negligible compared to the timescale of transverse expansion. These shortcomings have already been reported in the original KøMPøST paper [136] and will require further investigation in the future.

This work provides the baseline for analyses of hadronic collisions in frameworks based on the microscopic dynamics of kinetic theory. It is part of a series of recent efforts [49,71,88,89,94] to push the practical applicability of these dynamics in theoretical simulations. One important goal that has yet to be reached is to improve the codes that implement them in order to be able to also run event-by-event simulations. At the moment, the tool that is closest to fulfilling this goal is KøMPøST, which we confirmed to function properly for its intended use, but it is confined to the preequilibrium phase of heavy-ion collisions.

Broadly speaking, our results confirm that in principle hydrodynamics is the proper tool for describing midcentral collisions, if and only if preequilibrium is described correctly. Issues with this phase in hydrodynamic descriptions can be alleviated by changing the interpretation of the initial state in the way discussed in Sec. IV D. As alluded to in Sec. IV A as well as in previous works [65,137,138], appropriate changes to the evolution equations might achieve similar improvements. If such changes are not incorporated, we discussed in Sec. VI that hydrodynamic results can be in significant disagreement with kinetic theory. We also refer the interested reader to our companion paper [102], where we extract a more general criterion for the applicability of hydrodynamics and infer phenomenological conclusions for the description of the space-time dynamics of high-energy collisions.

ACKNOWLEDGMENTS

We thank P. Aasha, N. Borghini, H. Elfner, A. Mazeliauskas, H. Roch, A. Shark and U. A. Wiedemann for valuable discussions. This work is supported by the Deutsche Forschungsgemeinschaft (DFG, German Research Foundation) through the CRC-TR 211 "Strong-interaction matter under extreme conditions"—Project No. 315477589—TRR 211. V. E. A. gratefully acknowledges the support through a grant of the Ministry of Research, Innovation and Digitization, CNCS—UEFISCDI, Project No. PN-III-P1-1.1-TE-2021-1707, within PNCDI III. C. W. was supported by the program Excellence Initiative Research University of

the University of Wrocław of the Ministry of Education and Science. Numerical calculations presented in this work were performed at the Paderborn Center for Parallel Computing (PC2) and the Center for Scientific Computing (CSC) at the Goethe-University of Frankfurt and we gratefully acknowledge their support.

APPENDIX A: RELATIVISTIC LATTICE BOLTZMANN IMPLEMENTATION DETAILS

The first step in applying the RLB method is the parametrization of the momentum space, which we perform using two sets of coordinates, namely the spherical (subscript s) and free-streaming (subscript fs) coordinates:

$$(p_{\rm s}, v_{z;{\rm s}}) = \left(p^\tau, \frac{\tau p^\eta}{p^\tau}\right), \tag{A1a}$$

$$(p_{\rm fs}, v_{z;{\rm fs}}) = \left(p_{\rm s}\Delta_{\rm s}, \frac{\tau v_{z;{\rm s}}}{\tau_0 \Delta_{\rm s}}\right), \tag{A1b}$$

where $\Delta_{\rm s} = [1 + (\frac{\tau^2}{\tau_0^2} - 1)v_{z;{\rm s}}^2]^{1/2}$ [139]. The azimuthal coordinate $\varphi_p = \arctan(p^y/p^x)$ is employed in both parametrizations.

Due to the particularly simple nature of RTA, the dynamics of the observables introduced in Sec. II are fully described by the reduced distribution $\mathcal{F}_*$ ($* \in \{{\rm s}, {\rm fs}\}$), obtained from the phase-space distribution f via

$$\mathcal{F}_* = \frac{\nu_{\rm eff}\pi R^2 \tau_0}{(2\pi)^3}\left(\frac{{\rm d}E_\perp^0}{{\rm d}\eta}\right)^{-1}\int_0^\infty {\rm d}p_* p_*^3 f. \tag{A2}$$

Using the nondimensionalization conventions introduced around Eq. (19), the nondimensional function $\mathcal{F}_{\rm s} \equiv \mathcal{F}_{\rm s}(\tilde{\tau}, \tilde{\mathbf{x}}_T, \varphi_p, v_{z;{\rm s}})$ satisfies

$$\left(\tilde{\partial}_\tau + \sqrt{1 - v_{z;{\rm s}}^2}\mathbf{v}_\perp \cdot \tilde{\nabla}_\perp + \frac{1 + v_{z;{\rm s}}^2}{\tilde{\tau}}\right)\mathcal{F}_{\rm s} - \frac{1}{\tilde{\tau}}\frac{\partial[v_{z;{\rm s}}(1 - v_{z;{\rm s}}^2)\mathcal{F}_{\rm s}]}{\partial v_{z;{\rm s}}} = -\hat{\gamma} v^\mu u_\mu \tilde{T}(\mathcal{F}_{\rm s} - \mathcal{F}_{\rm s}^{\rm eq}), \tag{A3}$$

while $\mathcal{F}_{\rm fs} \equiv \mathcal{F}_{\rm fs}(\tilde{\tau}, \tilde{\mathbf{x}}_T, \varphi_p, v_{z;{\rm fs}})$ obeys

$$\left(\tilde{\partial}_\tau + \frac{1}{\Delta_{\rm fs}}\sqrt{1 - v_{z;{\rm fs}}^2}\mathbf{v}_\perp \cdot \tilde{\nabla}_\perp\right)\mathcal{F}_{\rm fs} = -\hat{\gamma} v^\mu u_\mu \tilde{T}(\mathcal{F}_{\rm fs} - \mathcal{F}_{\rm fs}^{\rm eq}), \tag{A4}$$

with $\Delta_{\rm fs} = [1 - (1 - \frac{\tilde{\tau}_0^2}{\tilde{\tau}^2})v_{z;{\rm fs}}^2]^{1/2}$. The equilibrium functions $\mathcal{F}_*^{\rm eq}$ are given by

$$\mathcal{F}_{\rm s}^{\rm eq} = \Delta_{\rm fs}^4 \mathcal{F}_{\rm fs}^{\rm eq} = \frac{\tilde{\tau}_0 \tilde{\epsilon}}{4\pi(v^\mu u_\mu)^4}, \tag{A5}$$

where

$$v^\mu u_\mu = \gamma(1 - \sqrt{1 - v_{z;{\rm s}}^2}\mathbf{v}_\perp \cdot \boldsymbol{\beta}) = \gamma\left(1 - \frac{1}{\Delta_{\rm fs}}\sqrt{1 - v_{z;{\rm fs}}^2}\mathbf{v}_\perp \cdot \boldsymbol{\beta}\right), \tag{A6}$$

with $\gamma = u^\tau \equiv 1/\sqrt{1 - \beta^2}$ being the local Lorentz factor. In the above, $\boldsymbol{\beta} = \beta(\cos\varphi_u, \sin\varphi_u)$ and $\mathbf{v}_\perp = (\cos\varphi_p, \sin\varphi_p)$ are transverse-plane vectors.

Vanishing longitudinal pressure and azimuthal momentum isotropy imply the following initial state for the reduced distributions $\mathcal{F}_*$:

$$\mathcal{F}_*(\tilde{\tau}_0, \tilde{\mathbf{x}}_\perp, \varphi_p, v_{z;*}) = \frac{\delta(v_{z;*})}{2\pi}\tilde{\tau}_0 \tilde{\epsilon}_0(\mathbf{x}_\perp) \tag{A7}$$

and depends only on the initial transverse energy distribution ${\rm d}E_\perp^0/{\rm d}\eta{\rm d}^2\mathbf{x}_\perp = \tau_0\epsilon_0$ [see Eq. (2)]. Note that at $\tau = \tau_0$, $\Delta_{\rm s} = \Delta_{\rm fs} = 1$ and $(p_{\rm fs}, v_{z;{\rm fs}}) = (p_{\rm s}, v_{z;{\rm s}})$.

Due to the singular nature of the Dirac delta function $\delta(v_z)$, Eq. (A7) cannot be achieved exactly with our numerical approach. We instead employ the Romatschke-Strickland distribution with anisotropy parameter ξ_0,

$$f_{\rm RS} = \left[\exp\left(\frac{p^\tau}{\Lambda_0}\sqrt{1 + \xi_0 v_z^2}\right) - 1\right]^{-1}, \tag{A8}$$

where $\xi_0 = 0$ corresponds to the isotropic Bose-Einstein distribution, while $\xi_0 \to \infty$ is required in order to achieve Eq. (A7). The parameter $\Lambda_0 \equiv \Lambda_0(\mathbf{x}_\perp)$ represents an energy scale satisfying

$$\Lambda_0 = 2^{1/4} T_0 \left(\frac{\arctan\sqrt{\xi_0}}{\sqrt{\xi_0}} + \frac{1}{1 + \xi_0}\right)^{-1/4}, \tag{A9}$$

reducing to the initial temperature T_0 when $\xi_0 = 0$. Thus, the system is initialized according to

$$\mathcal{F}_{0;{\rm s}} = \mathcal{F}_{0;{\rm fs}} = \frac{\tilde{\tau}_0 \tilde{\epsilon}_0}{2\pi}(1 + \xi_0 v_z^2)^2 \left(\frac{\arctan\sqrt{\xi_0}}{\sqrt{\xi_0}} + \frac{1}{1 + \xi_0}\right)^{-1}. \tag{A10}$$

We now summarize the characteristics and parameters of our RLB solver. The advection operator $\mathbf{v}_\perp \cdot \nabla_\perp$ is implemented using the upwind-biased finite-difference fifth-order weighted essentially nonoscillatory (WENO-5) scheme [125,140] (see Ref. [107] for details). The spatial domain consists of a square box of size $16R$ centered on the system's center of mass and is discretized equidistantly using S^2 cells. Periodic boundary conditions are employed at the domain edges. When initializing the system, a background value $\epsilon_{\rm th} = 10^{-10} \times \frac{R}{\tau_0}\epsilon_{\rm ref}$ is added to the energy density to avoid numerical underflow.

TABLE III. Simulation parameters for the RLB solver, as employed for the ranges of $4\pi\eta/s$ displayed in the left column. The notation is explained in this appendix.

$4\pi\eta/s$	S	$(\frac{\delta\tilde{\tau}}{\tilde{\tau}})_{\mathrm{M}}$	$\delta\tilde{\tau}_{\mathrm{M}}$	Q_φ	$Q_z(*)$	$\tilde{\tau}_0$	ξ_0	P_L/P_T
[0.01:0.5]	200	0.05	0.002	80	40(s)	10^{-6}	20	0.08
[1:5]	100	0.02	0.005	40	200(s)	10^{-6}	100	0.02
[10:1000]	100	0.1	0.005	40	1000(fs)	10^{-3}	1000	0.002

The time stepping is performed by solving the equation $\tilde{\partial}_\tau \mathcal{F}_* = L[\tilde{\tau}, \mathcal{F}_*(\tilde{\tau})]$ using the third-order Runge-Kutta scheme [125,141,142], as described in Ref. [107]. The time step $\delta\tilde{\tau}$ is chosen dynamically as

$$\delta\tilde{\tau}(\tilde{\tau}) = \min\left[\tilde{\tau}\left(\frac{\delta\tilde{\tau}}{\tilde{\tau}}\right)_{\mathrm{M}}, \frac{\max_\perp(\tilde{\tau}_R)}{2}, \delta\tilde{\tau}_{\mathrm{M}}\right], \tag{A11}$$

where $\max_\perp(\tilde{\tau}_R)$ represents the maximum value of $\tilde{\tau}_R(\tilde{\tau}, \tilde{\mathbf{x}_\perp})$ taken over the entire flow domain at time $\tilde{\tau} = \tau/R$, while the values of $(\delta\tilde{\tau}/\tilde{\tau})_{\mathrm{M}}$ and $\delta\tilde{\tau}_{\mathrm{M}}$ are shown in Table III.

The discretization of $\delta\varphi_p$ is done equidistantly using Q_φ points (the employed values of Q_φ are summarized in Table III).

The $v_{z;*}$ degree of freedom is discretized using Q_z values. When employing the spherical coordinate $v_{z;\mathrm{s}}$, these points are chosen according to the Gauss-Legendre quadrature rules as the roots of the Legendre polynomial of order Q_z, i.e. $P_{Q_z}(v_{z;j}) = 0$. When $v_{z;\mathrm{fs}}$ is employed, the discretization is performed equidistantly at the level of the parameter $\chi = \mathrm{artanh}(Av_{z;\mathrm{fs}})$, namely $\chi_j = (\frac{2j-1}{Q_z} - 1)\mathrm{artanh}A$. In this paper, we take $1 - A = 10^{-6}$ (see Sec. IV.B of Ref. [71] for more details).

As shown in Table III, the (s) and (fs) approaches are employed when $4\pi\eta/s \leq 5$ and $4\pi\eta/s \geq 10$, respectively. Employing the (s) approach at larger values of $4\pi\eta/s$ requires increasing Q_z, otherwise the time evolution leads to energy-momentum tensor configurations which are incompatible with the Landau frame. Using $Q_z = 200$ gives reliable results for $4\pi\eta/s \lesssim 10$. Because the computation of the force term involving $\partial_{v_z}\mathcal{F}$ is quadratic with respect to Q_z (see Sec. III.E of Ref. [107] for details), the (s) strategy becomes inefficient when $Q_z \gtrsim 200$.

Conversely, the (fs) approach requires larger Q_z as τ_f/τ_0 is increased (we ran all simulations up to $\tau_f = 5R$). Since in the (fs) approach, the computational time scales linearly with Q_z, we employed $Q_z = 1000$. With our choice of parameters, this limits the lower value of τ_0 to $10^{-3}R$, which is insufficient to correctly capture the early time dynamics of the system when $4\pi\eta/s \lesssim 1$.

Finally, the choice of ξ_0 in preparing the initial state depends on the $v_{z;*}$ resolution offered by the chosen discretization. As $\xi_0 \to \infty$, the initial state becomes peaked around $v_z = 0$, hence the $v_{z;*}$ discretization must include sufficient points around this value. We found that the influence of the initial value of ξ_0 on the observables is less significant at smaller values of $4\pi\eta/s$. Thus, we employed progressively larger values of ξ_0 as we increased η/s, which were compatible with the discretization of $v_{z;*}$, as shown in Table III.

APPENDIX B: NUMERICAL CODE COMPUTING LINEAR ORDER RESULTS

In this appendix, we discuss the numerical code needed for obtaining the linear order results discussed in Sec. III B. Section B 1 discusses the conceptual setup of the code and Sec. B 2 deals with the details of how the integration is performed.

1. Setup of the linear order code

The code is set up to compute the zeroth and first order contributions to the energy-momentum tensor, which is given in terms of the phase space density as

$$T^{\mu\nu} = \frac{\nu_{\mathrm{eff}}}{(2\pi)^3}\int \mathrm{d}^2p_\perp \int \mathrm{d}y\, p^\mu p^\nu f. \tag{B1}$$

For simplicity, observables that are nonlinear in $T^{\mu\nu}$ with contributions from both zeroth and first order in the opacity expansion were computed only to zeroth order.

The code is set up as follows. For an arbitrary initial energy density distribution $\epsilon_0(\tau_0, \mathbf{x}_\perp)$, the free-streaming energy momentum tensor is given as

$$T^{(0)\mu\nu} = \frac{\tau_0}{\tau}\int \frac{\mathrm{d}\phi_v}{2\pi} v_\perp^\mu v_\perp^\nu \epsilon(\tau_0, \mathbf{x}_\perp - \Delta\tau\mathbf{v}_\perp), \tag{B2}$$

where $\Delta\tau = \tau - \tau_0$. The integral over ϕ_v is performed numerically, using the same stencils for all entries to prevent errors later on. Now, to go to first order in the opacity expansion, we first have to compute the zeroth order results for the rest frame energy density $\epsilon(\tau, \mathbf{x}_\perp)$ and the flow velocity $u^\mu(\tau, \mathbf{x}_\perp)$, as they are required for evaluating the RTA collision kernel. This is achieved by numerical diagonalization of $T^{(0)\mu\nu}$.

As computed before [71], the first order correction to the phase space distribution is given as an integral of the zeroth order collision kernel:

$$f^{(1)}(\tau, \mathbf{x}_\perp, \mathbf{p}_\perp, y - \eta) = \int_{\tau_0}^{\tau} \mathrm{d}\tau' \frac{C[f^{(0)}]}{p^\tau}(\tau', \mathbf{x}'_\perp, \mathbf{p}_\perp, y' - \eta), \tag{B3}$$

where $f^{(0)}$ is the free-streaming solution given in Eq. (24). The primes on the variables indicate the use of free-streaming coordinates,

$$\mathbf{x}'_\perp = \mathbf{x}_\perp - \mathbf{v}_\perp t(\tau,\tau',y-\eta),$$
$$y' = \eta + \operatorname{arcsinh}\left(\frac{\tau}{\tau'}\sinh(y-\eta)\right), \tag{B4}$$

with $t(\tau,\tau',y-\eta)$ being given in Eq. (25).

From this, the first order correction to the energy-momentum tensor is obtained as

$$T^{(1)\mu\nu} = \frac{\nu_{\text{eff}}}{(2\pi)^3}\int_{\mathbf{p}_\perp}\int dy\, p^\mu p^\nu \int_{\tau_0}^{\tau} \mathrm{d}\tau' \times \frac{C[f^{(0)}](\tau',\mathbf{x}'_\perp,\mathbf{p}_\perp,y'-\eta)}{p^\tau(\mathbf{p}_\perp,y'-\eta)}, \tag{B5}$$

where $\int_{\mathbf{p}_\perp} \equiv \int d^2\mathbf{p}_\perp$. As it turns out, the observables that are to be computed to first order in opacity depend only on transverse integrals of the components of T^{ij}. Thus, we need to perform a 6D integral, which can be done in part analytically, reducing the complexity of the numerical integration. For further details of the analytical preparatory groundwork for the numerical implementation, see Appendix B 2.

The observables are now computed from these results in the following way. In the case of the transverse-plane energy, we have

$$\frac{\mathrm{d}E_{\text{tr}}}{\mathrm{d}\eta} = \tau\int_{\mathbf{x}_\perp}(T^{11}+T^{22}), = \tau\int_{\mathbf{x}_\perp}(T^{(0)11}+T^{(0)22}+T^{(1)11}+T^{(1)22}). \tag{B6}$$

As elliptic flow is given as a quotient of two transverse integrals of components of $T^{\mu\nu}$ where the numerator vanishes at zeroth order, the first order result is given as

$$e^{2i\Psi_p}\varepsilon_p = \frac{\int_{\mathbf{x}_\perp}(T^{11}-T^{22}+2iT^{12})}{\int_{\mathbf{x}_\perp}(T^{11}+T^{22})}, = \frac{\int_{\mathbf{x}_\perp}(T^{(1)11}-T^{(1)22}+2iT^{(1)12})}{\int_{\mathbf{x}_\perp}(T^{(0)11}+T^{(0)22})}. \tag{B7}$$

Both of these observables depend on the transverse integral of $T^{(0)11}+T^{(0)22}$, which using (B2) can be straightforwardly evaluated to

$$\int_{\mathbf{x}_\perp} T^{(0)11}+T^{(0)22} = \frac{1}{\tau}\frac{\mathrm{d}E^0_\perp}{\mathrm{d}\eta}. \tag{B8}$$

In particular, the quantity $\mathrm{d}E_{\text{tr}}/\mathrm{d}\eta$, which we introduced as the analog of $\mathrm{d}E_\perp/\mathrm{d}\eta = \int_{\mathbf{x}_\perp}\langle p^\tau p_\perp\rangle$, is in fact identical to $\mathrm{d}E_\perp/\mathrm{d}\eta$ to zeroth order. Furthermore it is constant in time, so only the first order correction has to be computed. We furthermore compute zeroth order results for the average transverse flow velocity and the average inverse Reynolds number as

$$\langle u_\perp\rangle = \frac{\int_{\mathbf{x}_\perp}\epsilon^{(0)}\sqrt{(u_1^{(0)})^2+(u_2^{(0)})^2}}{\int_{\mathbf{x}_\perp}\epsilon^{(0)}}, \tag{B9}$$

$$\langle \mathrm{Re}^{-1}\rangle = \frac{\int_{\mathbf{x}_\perp}\sqrt{6\pi^{(0)\mu\nu}\pi^{(0)}_{\mu\nu}}}{\int_{\mathbf{x}_\perp}\epsilon^{(0)}} = \frac{\int_{\mathbf{x}_\perp}\sqrt{6T^{(0)\mu\nu}T^{(0)}_{\mu\nu}-\frac{24}{3}(\epsilon^{(0)})^2}}{\int_{\mathbf{x}_\perp}\epsilon^{(0)}}. \tag{B10}$$

2. Analytical and numerical integration in the computation of linear order results

As discussed in the previous appendix, obtaining numerical results for the linear order term in the energy momentum tensor requires the computation of a 6D integral. In this appendix, we explain what part of this integral is performed analytically and give the specific form of the remaining integral which the code computes numerically.

We start from the expression in Eq. (B5) for the purely spatial components of the energy momentum tensor,

$$\int_{\mathbf{x}_\perp} T^{(1)ij} = \frac{\nu_{\text{eff}}}{(2\pi)^3}\int_{\mathbf{x}_\perp}\int_{\mathbf{p}_\perp}\int \mathrm{d}y\, \mathbf{p}^i_\perp\mathbf{p}^j_\perp \times \int_{\tau_0}^{\tau}\mathrm{d}\tau'\frac{C[f^{(0)}]}{p^\tau}(\tau',\mathbf{x}'_\perp,\mathbf{p}_\perp,y'-\eta), \tag{B11}$$

where the free-streaming coordinates $\mathbf{x}'_\perp$ and y' were introduced in Eq. (B4).

The integration variables can be changed from $(\mathbf{x}_\perp,y)$ to $(\mathbf{x}'_\perp,y')$, where

$$\mathrm{d}y'd^2\mathbf{x}'_\perp = \frac{\tau}{\tau'}\frac{\cosh(y-\eta)}{\cosh(y'-\eta)}\mathrm{d}yd^2\mathbf{x}_\perp, \tag{B12}$$

$$= \frac{\tau}{\tau'}\frac{\sqrt{1+(\frac{\tau'}{\tau})^2\sinh^2(y'-\eta)}}{\cosh(y'-\eta)}\mathrm{d}yd^2\mathbf{x}_\perp. \tag{B13}$$

Right away and from this point on, we will drop the primes on all coordinates except τ' for convenience. The specific form of the RTA kernel is

$$C[f] = -\frac{p^\mu u_\mu}{\tau_R}(f-f_{\text{eq}}), \tag{B14}$$

where $\tau_R = 5(\eta/s)T^{-1}$ is the relaxation time and

$$p^\mu u_\mu = \gamma p_\perp[\cosh(y-\eta)-\mathbf{v}_\perp\cdot\boldsymbol{\beta}], \tag{B15}$$

where $\mathbf{v}_\perp = \mathbf{p}_\perp/p_\perp = (\cos\varphi_p,\sin\varphi_p)$ is a unit vector in the transverse plane. Similarly, $\boldsymbol{\beta}\equiv\boldsymbol{u}_\perp/u^\tau = \beta(\cos\varphi_u,\sin\varphi_u)$ is the transverse-plane fluid velocity

and $\gamma = 1/\sqrt{1-\beta^2}$ is the local Lorentz factor. Plugging Eqs. (B13)–(B15) into Eq. (B11), we arrive at

$$\int_{\mathbf{x}_\perp} T^{(1)ij} = -\frac{\nu_{\rm eff}}{(2\pi)^3}\int_{\mathbf{p}_\perp}\int_{\mathbf{x}_\perp}\int \mathrm{d}y \int_{\tau_0}^{\tau}\frac{\tau'\mathrm{d}\tau'}{\tau} \times \frac{\mathbf{v}_\perp^i\mathbf{v}_\perp^j}{\tau_R}\frac{\gamma[\cosh(y-\eta)-\mathbf{v}_\perp\cdot\boldsymbol{\beta}]}{\sqrt{1+(\frac{\tau'}{\tau})^2\sinh^2(y-\eta)}} \times p_\perp^2(f^{(0)}-f_{\rm eq})(\tau',\mathbf{x}_\perp,\mathbf{p}_\perp,y-\eta). \tag{B16}$$

In the above, all macroscopic quantities τ_R, γ and $\boldsymbol{\beta}$ are computed from the zeroth order solution, $f^{(0)}$.

It is convenient to consider separately the contributions involving $f^{(0)}$ and $f_{\rm eq}$. In the case of the former, we plug in

$$f^{(0)}(\tau,\mathbf{x}_\perp,\mathbf{p}_\perp,y-\eta) = \frac{(2\pi)^3}{\nu_{\rm eff}}\frac{\delta(y-\eta)}{\tau p_\perp} \times \frac{\mathrm{d}N_0}{\mathrm{d}^2\mathbf{x}_\perp\mathrm{d}^2\mathbf{p}_\perp\mathrm{d}y}(\mathbf{x}_\perp-\mathbf{v}_\perp\Delta\tau,\mathbf{p}_\perp). \tag{B17}$$

Using the relation

$$\epsilon(\tau_0,\mathbf{x}_\perp-\mathbf{v}_\perp\Delta\tau) = \frac{2\pi}{\tau_0}\int \mathrm{d}p_\perp\, p_\perp^2 \times \frac{\mathrm{d}N_0}{\mathrm{d}^2\mathbf{x}_\perp\mathrm{d}^2\mathbf{p}_\perp\mathrm{d}y}(\mathbf{x}_\perp-\mathbf{v}_\perp\Delta\tau,\mathbf{p}_\perp), \tag{B18}$$

it is not difficult to obtain

$$\int_{\mathbf{x}_\perp} T^{(1)ij}_{(0)} = -\frac{\tau_0}{\tau}\int_{\tau_0}^{\tau}\mathrm{d}\tau'\int_{\mathbf{x}_\perp}\frac{\gamma}{\tau_R}\int\frac{\mathrm{d}\varphi_p}{2\pi} \times \mathbf{v}_\perp^i\mathbf{v}_\perp^j(1-\mathbf{v}_\perp\cdot\boldsymbol{\beta})\epsilon(\tau_0,\mathbf{x}_\perp-\mathbf{v}_\perp\Delta\tau'), \tag{B19}$$

where γ, τ_R and $\boldsymbol{\beta}$ are evaluated at $(\tau',\mathbf{x}_\perp)$.

For the equilibrium buildup contribution, we can use the property

$$\frac{\nu_{\rm eff}}{(2\pi)^3}\int_0^\infty \mathrm{d}p_\perp p_\perp^3 f_{\rm eq}\left(\frac{p^\mu u_\mu}{T}\right) = \frac{1}{4\pi}\frac{\epsilon}{(p^\mu u_\mu/p_\perp)^4}, \tag{B20}$$

leading to

$$\int_{\mathbf{x}_\perp} T^{(1)ij}_{\rm eq} = \int_{\mathbf{x}_\perp}\int_{\tau_0}^{\tau}\frac{\tau'\mathrm{d}\tau'}{\tau}\frac{\epsilon^{(0)}}{\tau_R}F^{ij}_{\rm eq}, \tag{B21}$$

where

$$F^{ij}_{\rm eq} = \int\frac{\mathrm{d}y}{2}\int\frac{\mathrm{d}\varphi_p}{2\pi}\frac{(p^\mu u_\mu/p_\perp)^{-3}}{\sqrt{1+(\frac{\tau'}{\tau})^2\sinh^2(y-\eta)}}\mathbf{v}_\perp^i\mathbf{v}_\perp^j, = \delta^{ij}I_{3/2}+3\beta^i\beta^j I_{5/2}. \tag{B22}$$

In the above, we introduced

$$I_\alpha = \frac{1}{4}\int_{-\infty}^{\infty}dy\frac{[\cosh^2(y-\eta)-\beta^2]^{-\alpha}}{\gamma^3\sqrt{1+(\frac{\tau'}{\tau})^2\sinh^2(y-\eta)}}. \tag{B23}$$

It is understood that, in Eq. (B21), the quantities $\epsilon^{(0)}$, τ_R, γ and $F^{ij}_{\rm eq}$ are evaluated at $(\tau',\mathbf{x}_\perp)$.

Altogether, $T^{(1)ij}$ can be computed using the following formula:

$$\int_{\mathbf{x}_\perp} T^{(1)ij} = \int_{\tau_0}^{\tau}d\tau'\int_{\mathbf{x}_\perp}\frac{1}{\tau_R}\int\frac{d\varphi_p}{2\pi}\left[\frac{\tau'}{\tau}\epsilon^{(0)}F^{ij}_{\rm eq} - \frac{\tau_0}{\tau}\epsilon(\tau_0,\mathbf{x}_\perp-\mathbf{v}_\perp\Delta\tau')\gamma\mathbf{v}_\perp^i\mathbf{v}_\perp^j(1-\mathbf{v}_\perp\cdot\boldsymbol{\beta})\right], \tag{B24}$$

where γ, τ_R, $\boldsymbol{\beta}$, $\epsilon^{(0)}$ and $F^{ij}_{\rm eq}$ are evaluated at $(\tau',\mathbf{x}_\perp)$. Note that the zeroth order results for the flow velocity $u^{(0)}_\mu$ and the rest frame energy density $\epsilon^{(0)}$ entering τ_R via the temperature have been computed in the first step of diagonalizing $T^{(0)\mu\nu}$. Thus, all quantities appearing in the above integrand are known and the remaining 4D integral can be performed numerically.

APPENDIX C: OVERVIEW OF TIME EVOLUTION AT DIFFERENT OPACITIES

In Sec. V B we compared the time evolution of the tracked observables in kinetic theory and scaled viscous hydro and pointed out some qualitative differences for results at three different opacities. To get a better overview of the opacity dependence in the time evolution, we can also compare results coming exclusively from kinetic theory on a wide range in opacity. This comparison for the time evolution of transverse energy $\mathrm{d}E_{\rm tr}/\mathrm{d}\eta$, elliptic flow ε_p, transverse flow velocity $\langle u_\perp\rangle_\epsilon$ and inverse Reynolds number $\langle \mathrm{Re}^{-1}\rangle_\epsilon$ is presented in Fig. 14 for opacities ranging from $4\pi\eta/s = 0.01$ to 1000.

For very small opacities $4\pi\eta/s \sim 1000$, the system is close to free streaming and transverse energy $\mathrm{d}E_{\rm tr}/\mathrm{d}\eta$ is almost constant. At larger opacities, due to more work being performed against the longitudinal expansion, $\mathrm{d}E_{\rm tr}/\mathrm{d}\eta$ decreases by a larger total amount. The opacity also sets the timescale for this cooling, as it sets in earlier for larger opacities.

Elliptic flow ε_p stays close to zero at small opacities $4\pi\eta/s \sim 1000$ and rises monotonically with opacity at each point in time. Qualitatively, the curves look the same at all opacities, with a buildup period at times $0.1R \lesssim \tau \lesssim 2R$ and almost constant behavior afterwards. The onset of this buildup is slightly earlier at larger opacities, but this difference is negligible.

As expected, the transverse flow velocity $\langle u_\perp\rangle_\epsilon$ starts with the same early time linear behavior for all opacities.

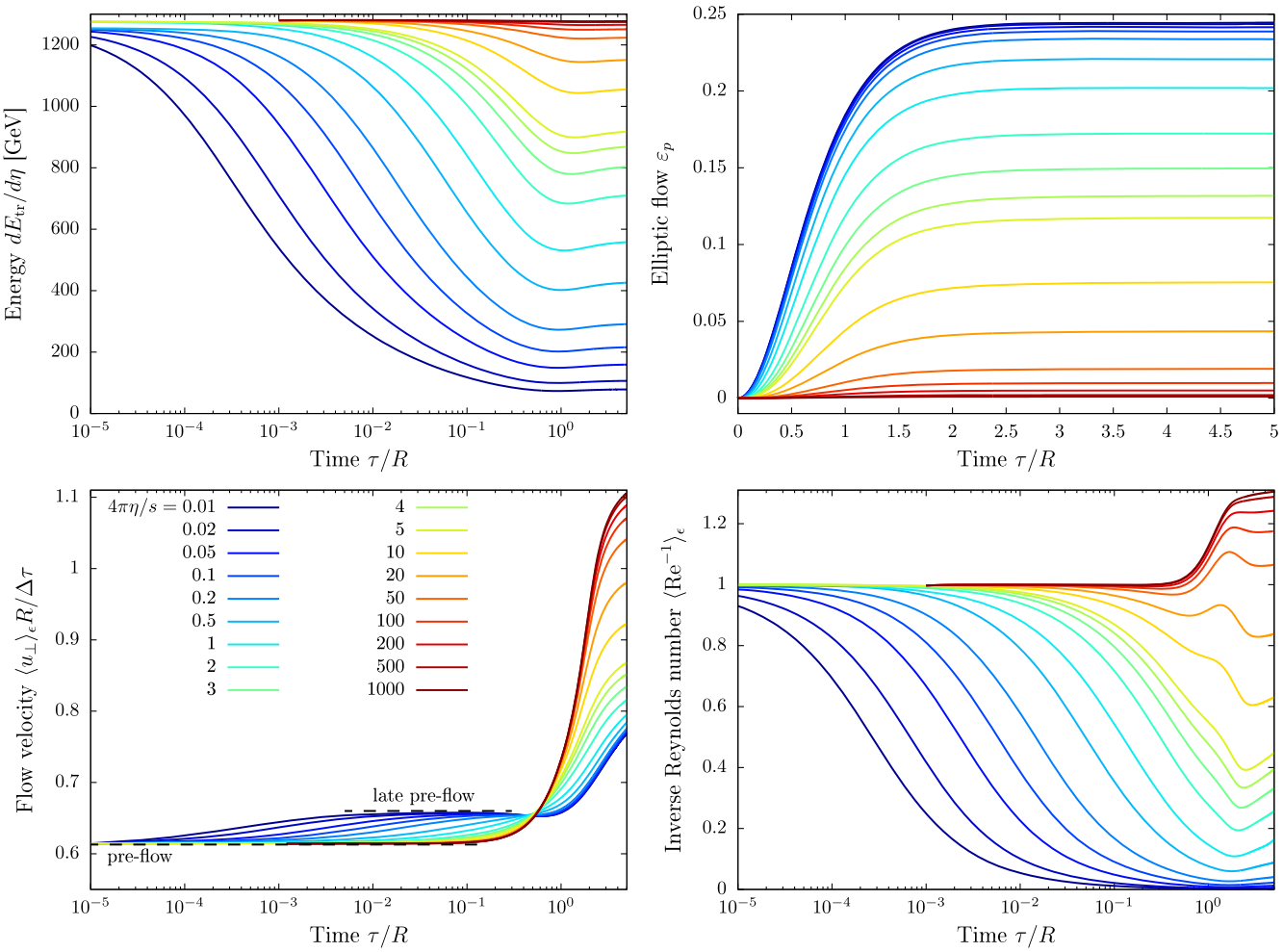

FIG. 14. Time evolution of transverse energy $dE_{\rm tr}/d\eta$ [top left, cf. Eq. (13)], elliptic flow ε_p [top right, cf. Eq. (14)], transverse flow velocity $\langle u_\perp\rangle_\epsilon$ [bottom left, cf. Eq. (15)] and inverse Reynolds number $\langle \mathrm{Re}^{-1}\rangle_\epsilon$ [bottom right, cf. Eq. (16)] in kinetic theory for a wide range of opacities (η/s) plotted in different colors. The plot of transverse flow velocity $\langle u_\perp\rangle_\epsilon$ also shows the preflow result $\langle u_\perp\rangle_{\epsilon,\rm early} = 0.614\Delta\tau/R$ according to Eq. (77) and the late preflow result $\langle u_\perp\rangle_{\epsilon,\rm late} = 0.658\Delta\tau/R$ according to Eq. (79) (see also Table II).

The proportionality constant with elapsed time $\Delta\tau = \tau - \tau_0$ can be computed according to Eq. (77) and evaluates to $\langle u_\perp\rangle_\epsilon = 0.614\Delta\tau/R$. The larger the opacity, the earlier the system starts to deviate from this behavior. For the largest opacities $4\pi\eta/s \lesssim 0.1$, the system is in its local Bjorken flow equilibrium state long enough for early time contributions to become negligible, such that it transitions to the late time preflow proportionality law. According to Eq. (79), in this regime, the flow velocity is given by $\langle u_\perp\rangle_\epsilon = 0.658\Delta\tau/R$. All curves exhibit their strongest rise on the timescale of transverse expansion, $\tau \sim R$. The rise is stronger at smaller opacities and in all cases contributes the most to the buildup, such that the final ($\tau = 4R$) values of transverse flow velocity are also larger at smaller opacities.

The inverse Reynolds number $\langle \mathrm{Re}^{-1}\rangle_\epsilon$ stays almost constant at early times for small opacities $4\pi\eta/s \sim 1000$, but then slightly increases due to transverse expansion. At large enough opacities $4\pi\eta/s \lesssim 10$, interactions equilibrate the system and decrease its value. This process sets in earlier at larger opacities and brings the value of the inverse Reynolds number down to almost zero for the largest opacities $4\pi\eta/s \lesssim 0.05$. In these cases, the value stays close to zero even during transverse expansion. At slightly smaller opacities $0.05 \lesssim 4\pi\eta/s \lesssim 1$, there is a small rise in inverse Reynolds number due to transverse expansion. However, this sets in later than in the case of the smallest opacities. The curves for intermediate to small opacities $1 \lesssim 4\pi\eta/s \lesssim 100$ exhibit a bumpy behavior during transverse expansion.

APPENDIX D: TIME EVOLUTION IN KøMPøST + VISCOUS HYDRO SIMULATIONS

In Sec. V C we considered hybrid simulation frameworks as a solution for alleviating problems with preequilibrium in hydrodynamic simulations and discussed the time evolution mainly in hybrid kinetic theory + viscous hydro simulations. The alternative hybrid framework using

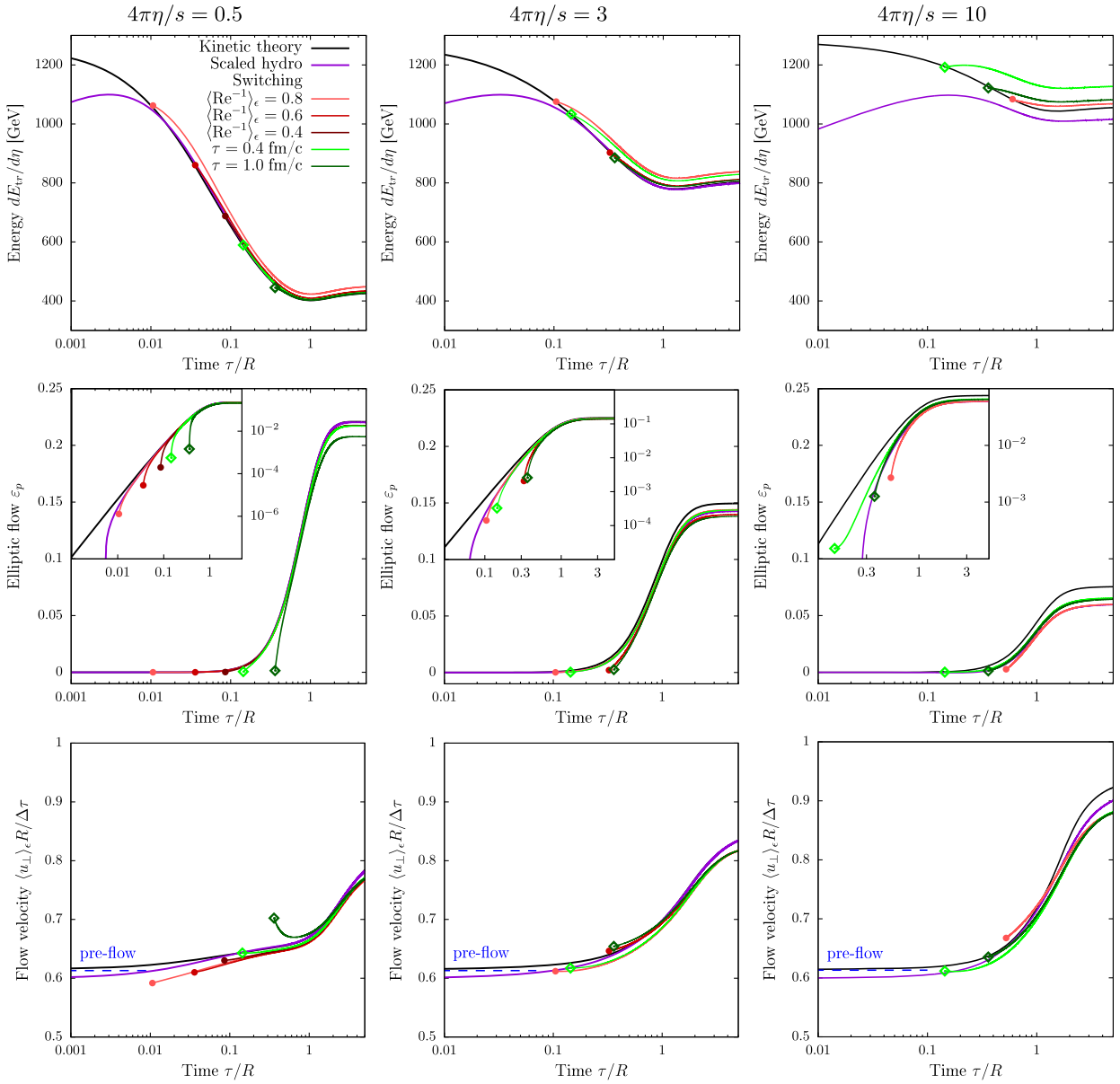

FIG. 15. Time evolution of transverse energy $\mathrm{d}E_{\mathrm{tr}}/\mathrm{d}\eta$ [top, cf. Eq. (13)], elliptic flow ε_p [middle, cf. Eq. (14)] and transverse flow velocity $\langle u_\perp\rangle_\epsilon$ [bottom, cf. Eq. (15)] in hybrid KøMPøST + viscous hydro simulations at opacities $4\pi\eta/s = 0.5$ (left), 3 (middle) and 10 (right) when switching at different values of the inverse Reynolds number [cf. Eq. (16)] $\langle \mathrm{Re}^{-1}\rangle_\epsilon = 0.8$ (light red), 0.6 (red) and 0.4 (dark red) or fixed time $\tau = 0.4$ fm (light green) and $\tau = 1$ fm (dark green). The switching points are marked with filled symbols. The time axis is scaled logarithmically. The plots showing elliptic flow ε_p feature an inset plot of the same quantity plotted in log-log scale. Again, the flow velocity plots also show the preflow result $\langle u_\perp\rangle_\epsilon = 0.614\Delta\tau/R$ according to Eq. (77).

KøMPøST instead of full kinetic theory for the preequilibrium evolution has some limitations but, when applicable, yields results of similar accuracy. The time evolution of transverse energy $\mathrm{d}E_{\mathrm{tr}}/\mathrm{d}\eta$, elliptic flow ε_p and transverse flow velocity $\langle u_\perp\rangle_\epsilon$ in KøMPøST + viscous hydro simulations switching at fixed time τ_s or fixed value of the inverse Reynolds number $\langle \mathrm{Re}^{-1}\rangle_\epsilon$ is shown in Fig. 15 for three different opacities $4\pi\eta/s = 0.5$, 3 and 10.

The values of $\mathrm{d}E_{\mathrm{tr}}/\mathrm{d}\eta$ at the time of switching are reproduced by KøMPøST almost perfectly. As one would expect, the time evolution afterwards follows a very similar behavior to kinetic theory + viscous hydrodynamics, including the inaccuracies of hydrodynamic preequilibrium when switching too early.

As KøMPøST produces almost no elliptic flow, its value at switching time is close to zero. But the buildup during the hydro part of the simulation proceeds similarly to other simulation schemes, such that the discrepancy to kinetic theory in the final state ($\tau = 4R$) is of similar size to the one at switching time. It is therefore larger at larger switching times.

The values of transverse flow velocity $\langle u_\perp \rangle_\epsilon$ are in KøMPøST slightly underestimated for small switching times and slightly overestimated for large switching times. After switching, the curves seem to bend towards the hydrodynamic curve. This bending is mainly due to the division by $\Delta\tau$. $\langle u_\perp \rangle_\epsilon$ in the hydro phase of hybrid simulations builds up similarly as in pure hydrodynamic simulations. The contributions from later times are much larger than those at early times, such that the discrepancy from early times becomes negligible. At late times, results from all switching times underestimate $\langle u_\perp \rangle_\epsilon$ by almost the same amount, similarly to hybrid kinetic theory + viscous hydro simulations.

[1] G. Nijs, W. van der Schee, U. Gürsoy, and R. Snellings, Phys. Rev. C **103**, 054909 (2021).
[2] F. G. Gardim, G. Giacalone, M. Luzum, and J.-Y. Ollitrault, Nat. Phys. **16**, 615 (2020).
[3] D. Everett *et al.* (JETSCAPE Collaboration), Phys. Rev. C **103**, 054904 (2021).
[4] D. A. Teaney, Viscous hydrodynamics and the quark gluon plasma, in *Quark-Gluon Plasma 4*, edited by R. C. Hwa and X.-N. Wang (World Scientific, Singapore, 2010), pp. 207–266, 10.1142/9789814293297_0004.
[5] H. Song, S. A. Bass, U. Heinz, T. Hirano, and C. Shen, Phys. Rev. Lett. **106**, 192301 (2011).
[6] C. Gale, S. Jeon, and B. Schenke, Int. J. Mod. Phys. A **28**, 1340011 (2013).
[7] U. Heinz and R. Snellings, Annu. Rev. Nucl. Part. Sci. **63**, 123 (2013).
[8] M. Luzum and H. Petersen, J. Phys. G **41**, 063102 (2014).
[9] S. Jeon and U. Heinz, Int. J. Mod. Phys. E **24**, 1530010 (2015).
[10] J. H. Putschke *et al.*, arXiv:1903.07706.
[11] B. B. Abelev *et al.* (ALICE Collaboration), Phys. Rev. C **90**, 054901 (2014).
[12] M. Aaboud *et al.* (ATLAS Collaboration), Eur. Phys. J. C **77**, 428 (2017).
[13] A. M. Sirunyan *et al.* (CMS Collaboration), Phys. Rev. Lett. **120**, 092301 (2018).
[14] K. Dusling, W. Li, and B. Schenke, Int. J. Mod. Phys. E **25**, 1630002 (2016).
[15] C. Loizides, Nucl. Phys. **A956**, 200 (2016).
[16] J. L. Nagle and W. A. Zajc, Annu. Rev. Nucl. Part. Sci. **68**, 211 (2018).
[17] P. Bozek, Phys. Rev. C **85**, 014911 (2012).
[18] P. Bozek and W. Broniowski, Phys. Lett. B **718**, 1557 (2013).
[19] P. Bozek and W. Broniowski, Phys. Lett. B **720**, 250 (2013).
[20] P. Bozek and W. Broniowski, Phys. Rev. C **88**, 014903 (2013).
[21] P. Bozek, W. Broniowski, and G. Torrieri, Phys. Rev. Lett. **111**, 172303 (2013).
[22] A. Bzdak, B. Schenke, P. Tribedy, and R. Venugopalan, Phys. Rev. C **87**, 064906 (2013).
[23] G.-Y. Qin and B. Müller, Phys. Rev. C **89**, 044902 (2014).
[24] K. Werner, M. Bleicher, B. Guiot, I. Karpenko, and T. Pierog, Phys. Rev. Lett. **112**, 232301 (2014).
[25] I. Kozlov, M. Luzum, G. Denicol, S. Jeon, and C. Gale, arXiv:1405.3976.
[26] B. Schenke and R. Venugopalan, Phys. Rev. Lett. **113**, 102301 (2014).
[27] P. Romatschke, Eur. Phys. J. C **75**, 305 (2015).
[28] C. Shen, J.-F. Paquet, G. S. Denicol, S. Jeon, and C. Gale, Phys. Rev. C **95**, 014906 (2017).
[29] R. D. Weller and P. Romatschke, Phys. Lett. B **774**, 351 (2017).
[30] H. Mäntysaari, B. Schenke, C. Shen, and P. Tribedy, Phys. Lett. B **772**, 681 (2017).
[31] B. Schenke, C. Shen, and P. Tribedy, Phys. Lett. B **803**, 135322 (2020).
[32] B. Schenke, Rep. Prog. Phys. **84**, 082301 (2021).
[33] S. Demirci, T. Lappi, and S. Schlichting, Phys. Rev. D **103**, 094025 (2021).
[34] B. Schenke, S. Schlichting, and R. Venugopalan, Phys. Lett. B **747**, 76 (2015).
[35] L. McLerran and V. Skokov, Nucl. Phys. **A947**, 142 (2016).
[36] B. Schenke, S. Schlichting, P. Tribedy, and R. Venugopalan, Phys. Rev. Lett. **117**, 162301 (2016).
[37] K. Dusling, M. Mace, and R. Venugopalan, Phys. Rev. Lett. **120**, 042002 (2018).
[38] K. Dusling, M. Mace, and R. Venugopalan, Phys. Rev. D **97**, 016014 (2018).
[39] M. Greif, C. Greiner, B. Schenke, S. Schlichting, and Z. Xu, Phys. Rev. D **96**, 091504 (2017).
[40] M. Mace, V. V. Skokov, P. Tribedy, and R. Venugopalan, Phys. Rev. Lett. **121**, 052301 (2018); **123**, 039901(E) (2019).
[41] M. Mace, V. V. Skokov, P. Tribedy, and R. Venugopalan, Phys. Lett. B **788**, 161 (2019); **799**, 135006(E) (2019).
[42] A. Kovner and V. V. Skokov, Phys. Lett. B **785**, 372 (2018).
[43] M. Greif, C. Greiner, S. Plätzer, B. Schenke, and S. Schlichting, Phys. Rev. D **103**, 054011 (2021).
[44] P. Agostini, T. Altinoluk, and N. Armesto, Eur. Phys. J. C **81**, 760 (2021).
[45] M. E. Carrington, A. Czajka, and S. Mrowczynski, Phys. Rev. C **106**, 034904 (2022).
[46] B. Schenke, S. Schlichting, and P. Singh, Phys. Rev. D **105**, 094023 (2022).
[47] A. Kurkela and Y. Zhu, Phys. Rev. Lett. **115**, 182301 (2015).
[48] M. P. Heller and V. Svensson, Phys. Rev. D **98**, 054016 (2018).
[49] A. Kurkela, S. F. Taghavi, U. A. Wiedemann, and B. Wu, Phys. Lett. B **811**, 135901 (2020).

[50] S. Schlichting and D. Teaney, Annu. Rev. Nucl. Part. Sci. **69**, 447 (2019).
[51] J. Berges, M. P. Heller, A. Mazeliauskas, and R. Venugopalan, Rev. Mod. Phys. **93**, 035003 (2021).
[52] J. Berges, K. Boguslavski, S. Schlichting, and R. Venugopalan, Phys. Rev. D **89**, 114007 (2014).
[53] J. Berges, K. Boguslavski, S. Schlichting, and R. Venugopalan, J. High Energy Phys. 05 (2014) 054.
[54] M. P. Heller and M. Spalinski, Phys. Rev. Lett. **115**, 072501 (2015).
[55] M. Spaliński, Phys. Lett. B **776**, 468 (2018).
[56] M. Strickland, J. Noronha, and G. Denicol, Phys. Rev. D **97**, 036020 (2018).
[57] M. Strickland, J. High Energy Phys. 12 (2018) 128.
[58] M. Spaliński, Phys. Lett. B **784**, 21 (2018).
[59] G. Giacalone, A. Mazeliauskas, and S. Schlichting, Phys. Rev. Lett. **123**, 262301 (2019).
[60] A. Kurkela, W. van der Schee, U. A. Wiedemann, and B. Wu, Phys. Rev. Lett. **124**, 102301 (2020).
[61] G. S. Denicol and J. Noronha, Phys. Rev. Lett. **124**, 152301 (2020).
[62] D. Almaalol, A. Kurkela, and M. Strickland, Phys. Rev. Lett. **125**, 122302 (2020).
[63] M. P. Heller, R. Jefferson, M. Spaliński, and V. Svensson, Phys. Rev. Lett. **125**, 132301 (2020).
[64] X. Du and S. Schlichting, Phys. Rev. Lett. **127**, 122301 (2021).
[65] J.-P. Blaizot and L. Yan, Phys. Rev. C **104**, 055201 (2021).
[66] C. Chattopadhyay, S. Jaiswal, L. Du, U. Heinz, and S. Pal, Phys. Lett. B **824**, 136820 (2022).
[67] X. Du, M. P. Heller, S. Schlichting, and V. Svensson, Phys. Rev. D **106**, 014016 (2022).
[68] A. Behtash, S. Kamata, M. Martinez, and H. Shi, J. High Energy Phys. 07 (2020) 226.
[69] A. Dash and V. Roy, Phys. Lett. B **806**, 135481 (2020).
[70] V. E. Ambruş, S. Busuioc, J. A. Fotakis, K. Gallmeister, and C. Greiner, Phys. Rev. D **104**, 094022 (2021).
[71] V. E. Ambruş, S. Schlichting, and C. Werthmann, Phys. Rev. D **105**, 014031 (2022).
[72] T. Nunes da Silva, D. Chinellato, M. Hippert, W. Serenone, J. Takahashi, G. S. Denicol, M. Luzum, and J. Noronha, Phys. Rev. C **103**, 054906 (2021).
[73] C. Gale, J.-F. Paquet, B. Schenke, and C. Shen, Phys. Rev. C **105**, 014909 (2022).
[74] D. Liyanage, D. Everett, C. Chattopadhyay, and U. Heinz, Phys. Rev. C **105**, 064908 (2022).
[75] T. N. da Silva, D. D. Chinellato, A. V. Giannini, M. N. Ferreira, G. S. Denicol, M. Hippert, M. Luzum, J. Noronha, and J. Takahashi, arXiv:2211.10561.
[76] C. M. Ko, Q. Li, and R.-C. Wang, Phys. Rev. Lett. **59**, 1084 (1987).
[77] B. Blattel, V. Koch, W. Cassing, and U. Mosel, Phys. Rev. C **38**, 1767 (1988).
[78] Q. Li, J. Q. Wu, and C. M. Ko, Phys. Rev. C **39**, 849 (1989).
[79] W. Botermans and R. Malfliet, Phys. Rep. **198**, 115 (1990).
[80] Z. Xu and C. Greiner, Phys. Rev. C **71**, 064901 (2005).
[81] Z. Xu, C. Greiner, and H. Stocker, Phys. Rev. Lett. **101**, 082302 (2008).
[82] H. Heiselberg and A.-M. Levy, Phys. Rev. C **59**, 2716 (1999).
[83] N. Borghini and C. Gombeaud, Eur. Phys. J. C **71**, 1612 (2011).
[84] P. Romatschke, Eur. Phys. J. C **78**, 636 (2018).
[85] N. Kersting, N. Borghini, and S. Feld, MDPI Proc. **10**, 16 (2019).
[86] A. Kurkela, U. A. Wiedemann, and B. Wu, Phys. Lett. B **783**, 274 (2018).
[87] N. Borghini, S. Feld, and N. Kersting, Eur. Phys. J. C **78**, 832 (2018).
[88] A. Kurkela, U. A. Wiedemann, and B. Wu, Eur. Phys. J. C **79**, 965 (2019).
[89] A. Kurkela, A. Mazeliauskas, and R. Törnkvist, J. High Energy Phys. 11 (2021) 216.
[90] N. Borghini, M. Borrell, and H. Roch, Eur. Phys. J. C **82**, 961 (2022).
[91] M. Borrell and N. Borghini, Eur. Phys. J. C **82**, 525 (2022).
[92] B. Bachmann, N. Borghini, N. Feld, and H. Roch, Eur. Phys. J. C **83**, 114 (2023).
[93] L. He, T. Edmonds, Z.-W. Lin, F. Liu, D. Molnar, and F. Wang, Phys. Lett. B **753**, 506 (2016).
[94] H. Roch and N. Borghini, Eur. Phys. J. C **81**, 380 (2021).
[95] B. V. Jacak and B. Muller, Science **337**, 310 (2012).
[96] B. Schenke, P. Tribedy, and R. Venugopalan, Phys. Rev. Lett. **108**, 252301 (2012).
[97] M. L. Miller, K. Reygers, S. J. Sanders, and P. Steinberg, Annu. Rev. Nucl. Part. Sci. **57**, 205 (2007).
[98] J. Auvinen, K. J. Eskola, P. Huovinen, H. Niemi, R. Paatelainen, and P. Petreczky, Phys. Rev. C **102**, 044911 (2020).
[99] F. Cooper and G. Frye, Phys. Rev. D **10**, 186 (1974).
[100] H. Petersen, J. Steinheimer, G. Burau, M. Bleicher, and H. Stöcker, Phys. Rev. C **78**, 044901 (2008).
[101] J. E. Bernhard, J. S. Moreland, and S. A. Bass, Nat. Phys. **15**, 1113 (2019).
[102] V. E. Ambrus, S. Schlichting, and C. Werthmann, arXiv:2211.14356.
[103] K. Yagi, T. Hatsuda, and Y. Miake, *Quark-Gluon Plasma (From Big Bang to Little Bang)*, Vol. 23 (Cambridge University Press, 2005).
[104] S. Ryu, J. F. Paquet, C. Shen, G. S. Denicol, B. Schenke, S. Jeon, and C. Gale, Phys. Rev. Lett. **115**, 132301 (2015).
[105] J. E. Bernhard, J. S. Moreland, S. A. Bass, J. Liu, and U. Heinz, Phys. Rev. C **94**, 024907 (2016).
[106] P. B. Arnold, G. D. Moore, and L. G. Yaffe, J. High Energy Phys. 01 (2003) 030.
[107] V. E. Ambruş and R. Blaga, Phys. Rev. C **98**, 035201 (2018).
[108] V. Ambruş, L. Bazzanini, A. Gabbana, D. Simeoni, R. Tripiccione, and S. Succi, Nature Computational Science **2**, 641 (2022).
[109] A. Kurkela, A. Mazeliauskas, J.-F. Paquet, S. Schlichting, and D. Teaney, Phys. Rev. Lett. **122**, 122302 (2019).
[110] A. Kurkela, A. Mazeliauskas, J.-F. Paquet, S. Schlichting, and D. Teaney, KøMPøST, https://github.com/KMPST/KoMPoST (2018).
[111] A. H. Mueller, Phys. Lett. B **475**, 220 (2000).
[112] N. Borghini, M. Borrell, N. Feld, H. Roch, S. Schlichting, and C. Werthmann, Phys. Rev. C **107**, 034905 (2023).

[113] A. Bazavov *et al.* (HotQCD Collaboration), Phys. Rev. D **90**, 094503 (2014).
[114] S. Borsanyi *et al.*, Nature (London) **539**, 69 (2016).
[115] I. Karpenko, P. Huovinen, and M. Bleicher, Comput. Phys. Commun. **185**, 3016 (2014).
[116] S. Kamata, M. Martinez, P. Plaschke, S. Ochsenfeld, and S. Schlichting, Phys. Rev. D **102**, 056003 (2020).
[117] J. Anderson and H. Witting, Physica **74**, 466 (1974).
[118] J. Anderson and H. Witting, Physica **74**, 489 (1974).
[119] C. Cercignani and G. M. Kremer, *The Relativistic Boltzmann Equation: Theory and Applications* (Birkhäuser Verlag, Basel, Switzerland, 2002), 10.1007/978-3-0348-8165-4.
[120] G. S. Denicol and D. H. Rischke, *Microscopic Foundations of Relativistic Fluid Dynamics*, Vol. 990 (Springer, Cham, 2021), 10.1007/978-3-030-82077-0.
[121] W. Florkowski, R. Ryblewski, and M. Strickland, Phys. Rev. C **88**, 024903 (2013).
[122] P. Romatschke, M. Mendoza, and S. Succi, Phys. Rev. C **84**, 034903 (2011).
[123] S. Succi, *The Lattice Boltzmann Equation: For Complex States of Flowing Matter* (Oxford University Press, Oxford, UK, 2018), 10.1093/oso/9780199592357.001.0001.
[124] A. Gabbana, D. Simeoni, S. Succi, and R. Tripiccione, Phys. Rep. **863**, 1 (2020).
[125] L. Rezzolla and O. Zanotti, *Relativistic Hydrodynamics* (Oxford University Press, Oxford, UK, 2013), 10.1093/acprof:oso/9780198528906.001.0001.
[126] W. A. Hiscock and L. Lindblom, Ann. Phys. (N.Y.) **151**, 466 (1983).
[127] W. A. Hiscock and L. Lindblom, Phys. Rev. D **31**, 725 (1985).
[128] I. Müller, Z. Phys. **198**, 329 (1967).
[129] W. Israel and J. M. Stewart, Ann. Phys. (N.Y.) **118**, 341 (1979).
[130] G. S. Denicol, H. Niemi, E. Molnar, and D. H. Rischke, Phys. Rev. D **85**, 114047 (2012); **91**, 039902(E) (2015).
[131] A. Jaiswal, Phys. Rev. C **87**, 051901 (2013).
[132] E. Molnár, H. Niemi, G. S. Denicol, and D. H. Rischke, Phys. Rev. D **89**, 074010 (2014).
[133] V. E. Ambrus, E. Molnár, and D. H. Rischke, Phys. Rev. D **106**, 076005 (2022).
[134] J. Vredevoogd and S. Pratt, Phys. Rev. C **79**, 044915 (2009).
[135] P. Romatschke, Phys. Rev. Lett. **120**, 012301 (2018).
[136] A. Kurkela, A. Mazeliauskas, J.-F. Paquet, S. Schlichting, and D. Teaney, Phys. Rev. C **99**, 034910 (2019).
[137] M. Martinez and M. Strickland, Nucl. Phys. **A848**, 183 (2010).
[138] W. Florkowski and R. Ryblewski, Phys. Rev. C **83**, 034907 (2011).
[139] A. Kurkela, U. A. Wiedemann, and B. Wu, Eur. Phys. J. C **79**, 759 (2019).
[140] G. S. Jiang and C. W. Shu, J. Comput. Phys. **126**, 202 (1996).
[141] C.-W. Shu and S. Osher, J. Comput. Phys. **77**, 439 (1988).
[142] S. Gottlieb and C.-W. Shu, Math. Comput. **67**, 73 (1998).